공학박사 학위논문

Experiment on Critical Heat Flux under Rolling Condition for TAPINS-M Code Development

TAPINS-M 코드 개발을 위한 롤링 조건에서의 임계열속 현상에 관한 실험적 고찰

2013 년 **8** 월

서울대학교 대학원

에너지시스템공학부

황 진 석

Experiment on Critical Heat Flux under Rolling Condition for TAPINS-M Code Development

TAPINS-M 코드 개발을 위한 롤링 조건에서의
임계열속 현상에 관한 실험적 고찰

지도교수 조 형 규

이 논문을 공학박사 학위논문으로 제출함
2013 년 **4** 월

서울대학교 대학원
에너지시스템공학부
황 진 석

황진석의 박사 학위논문을 인준함
2013 년 **6** 월

위 원 장	서 균 렬 (인)
부위원장	조 형 규 (인)
위 원	심 형 진 (인)
위 원	박 군 철 (인)
위 원	이 광 원 (인)

Abstract

Experiment on Critical Heat Flux under Rolling Condition for TAPINS-M Code Development

Jin-Seok Hwang
Department of Energy System Engineering
The Graduate School
Seoul National University

One of the biggest differences between a marine reactor and a land-based reactor is that the former is exposed to ship motions, such as heaving and rolling. Thus, in designing marine reactors, it is crucial to quantitatively evaluate the effects of ship motions on the thermal-hydraulics of the reactor coolant system. Furthermore, it is vital to predict CHF of a marine reactor under rolling motion in order to consider the safety design and operation of the reactor.

The objectives of this study are to develop a system analysis code for thermal-hydraulic simulation of a marine reactor, development of a CHF correlation under rolling motion and the validation of the developed code. This system analysis code TAPINS-M (Thermal-hydraulic Analysis Program for Integral reactor System-Marine reactor), implements the moving model and the developed CHF

correlation under rolling motion.

Extensive CHF analyses have been carried out in the past and numbers of CHF correlation have been developed. But, most of the existing CHF correlation cannot be applied to marine reactor directly. In spite of the efforts by many researchers, experimental study on CHF under rolling motion was barely reported so far.

In order to understand the characteristics of CHF under rolling motion, the experiment with MARMS (Marine Reactor Moving Simulator) is conducted. Predominant finding obtained through MARMS result is that the CHF ratio under rolling motion is either enhanced or deteriorated depending on mass flux. In order to classify the CHF mechanism, the flow regime must be determined in advance. The flow regime is determined by using a void fraction at the onset of the annular flow (OAF) suggested by phenomenological liquid film dryout (LFD) analysis. The flow regimes consist of bubbly (BF), annular (AF) flow and transition region (TR). Non-dimensional parameters and functional forms of correlations in BF and AF regions are determined based on the literature surveys on enhanced and deteriorated CHF phenomena. The CHF ratio can be predicted by logistic function using void fraction profile as the CHF mechanism in TR cannot be explain clearly. The mechanism of TR is taken into account by mean of logistic function, which is expressed by a function of void fraction at OAF.

Various normal and transient analyses are carried out for validation of the TAPINS-M. The validation works for normal condition are performed with experiments on the CHF, single- and two-phase natural circulation, and two-phase forced convection under rolling motion. To generate the transient data such as pump trip and pressure transient for code validation, additional tests are conducted

using MARMS. The TAPINS-M calculation results are compared with the test data gained under transient conditions in MARMS. From the validation results, it was revealed that the TAPINS-M code can provide a reliable prediction on the thermal-hydraulic phenomena in a marine reactor.

Keywords

Marine reactor, MARMS, Critical Heat Flux (CHF), Fluid-to-fluid scaling, R-134a, TAPINS-M code, CHF correlation, Moving model, Code validation

Student Number: 2009-30264

List of Contents

List of Tables

List of Figures

Chapter 1

Introduction

1.1 Background and Motivation

Nuclear-powered ships have outstanding advantages such as capability to navigate for a long period at high power and ability to navigate submerged for a long period. It is difficult for conventional ships to achieve these features. Thus, nuclear-powered ships are expected to make significant contribution to the advancement and diversification of marine transportation and scientific activities in the ocean in the future. (Fujino, 2000)

- The nuclear-powered ships can function as::
  - Icebreaker
  - Polar observation ship
  - 6500m deep-sea scientific research submersible
  - 600m undersea scientific research submersible
  - Floating power station
- Merchant nuclear ships:
  - SES (Surface Effects ship)-type super high-speed container ship
  - Displacement-type large high-speed container ship
  - Icebreaking crude-oil tanker

- Icebreaking container ship
- Undersea crude-oil tanker
- Ocean tug
- Super large container barge carrier

The characteristics of atomic energy and its utilization are shown in Fig. 1.1, where various types of nuclear ships mentioned above are categorized into three groups. One of the biggest differences between a marine reactor and a land-based reactor is that the former is greatly influenced by ship motions. Therefore, in designing a marine reactor, it is very important to quantitatively evaluate the effects of ship motions on the thermal-hydraulics of the reactor coolant system. The ship motions include linear motions such as surging, swaying and heaving, and rotational motions such as pitching, rolling and yawing, as shown in Fig 1.2. Especially, rolling and heaving are major motions to affect the thermal-hydraulic behavior of a marine reactor. Rolling motion is a kind of rotation which gives the system a time-dependent inclination together with a centrifugal and a tangential force. And heaving is the motion which gives a system a uniform time-dependent linear vertical gravity acceleration variation. Variation of flow patterns, instability, heat transfer and critical heat flux (CHF) in coolant channel are affected by rolling and heaving motions. Among them, prediction of the CHF characteristic is an important factor to marine reactor safety and its design.

Several researchers (Chang, 1997; Isshiki, 1965; Otsuji, 1982; Hwang, 2011) have performed studies on CHF under heaving motion. Their correlations are mostly based on the Zuber's et al. (1959) finding that CHF in pool boiling is proportional to the gravitational acceleration to the power of one fourth. Otherwise, they just identified the tendency of the effects in test conditions. Also, a few experimental and numerical researches have been carried out for single-phase natural circulation characteristics (Tan, 2009a), two-phase flow instability (Tan, 2009b), heat transfer and flow variation (Murata, 1990, 2000, 2002), and CHF (Hwang, 2012) under rolling motions.

In spite of the efforts by many researchers, predictions of CHF under rolling motion and comparisons between rolling and heaving motions have been barely reported so far.

1.2 Objectives of This Study

Three objectives are proposed in this study. One is to develop a system analysis code for thermal-hydraulic simulation of marine reactors with implementation of moving model. Another is the development of CHF correlation under rolling motion. The other is the validation of the code. As a unique contribution of this study, prediction model of CHF is newly proposed. And that model is incorporated into the developed code for better prediction of CHF in steady and transient conditions under rolling motion. Additional experiments under various flow conditions were conducted in an apparatus for rolling motion. The produced unique data from experiments are used for code validation. The outline of this study is described in Fig. 1.3. The scopes of this research are summarized as follows;

Development of rolling CHF correlation: A series of experiments were performed in the apparatus for CHF under rolling motion named MArine Reactor Moving Simulator (MARMS). CHF loop in MARMS is mounted on the rolling equipment. The data generated from the experiment are used to develop the CHF prediction model through understanding the CHF mechanisms and identifying the flow regimes under rolling motion.

Development of TAPINS-M: A system analysis code named TAPINS (Thermal-hydraulic Analysis Program for INtegral reactor System) is modified for the analysis of the marine reactor during natural circulation and forced convection. The modified code is named as TAPINS-M, where M stands for a marine reactor. The CHF correlation developed by MARMS data was complemented and moving models for heaving and rolling motion were added.

TAPINS-M validation: In order to confirm the applicability of TAPINS-M for marine reactor, the code validation is performed against several additional experiments with MARMS. The assessment matrix for code validation is prepared, ranging from steady-state to transient test problems investigated in this study. The results of TAPINS-M are compared with the experimental data. From the comparison, it was noted that the TAPINS-M code can provide reliable prediction for various flow condition under transient conditions as well as normal operation conditions.

1.3 Outline of the Thesis

Chapter 2 reports literature reviews on thermal-hydraulic characteristics and issues in a marine reactor. Previous studies on a marine reactor under rolling and heaving motions are presented. Chapter 3 provides detailed information related to the experimental test facility named Marine Reactor Moving Simulator (MARMS). A brief description of CHF mechanisms at various flow conditions, CHF scaling theories and a survey of various CHF scaling techniques are explained. The parametric trend study (inlet subcooling, mass flux, system pressure, rolling angle and rolling period) for CHF under rolling condition is discussed. Fluid-to-fluid scaling technique (R-134a to water) is utilized to compare the equivalent water CHF data with CHF look-up table at stationary. Also, a CHF prediction model under rolling condition is developed by determination of flow regime. The development of TAPINS-M is presented in Chapter 4. Modification of TAPINS code and the validation with the analysis of MAMRS data are explained. The code validation results at various flow conditions are covered in this chapter. Finally, the conclusion of this study is given in Chapter 5.

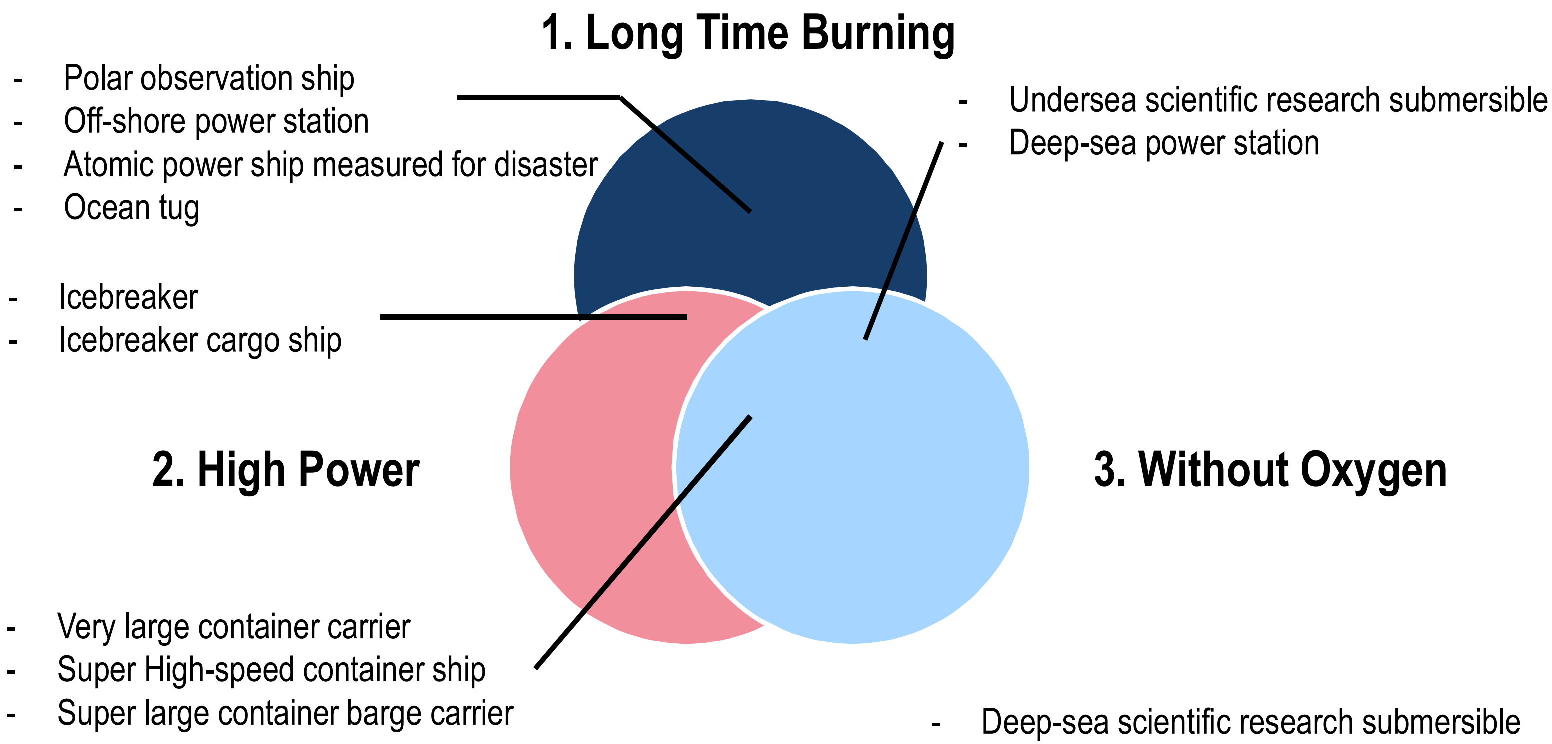

Figure 1.1 Characteristic features of nuclear energy and its utilization (Fujino, 2000)

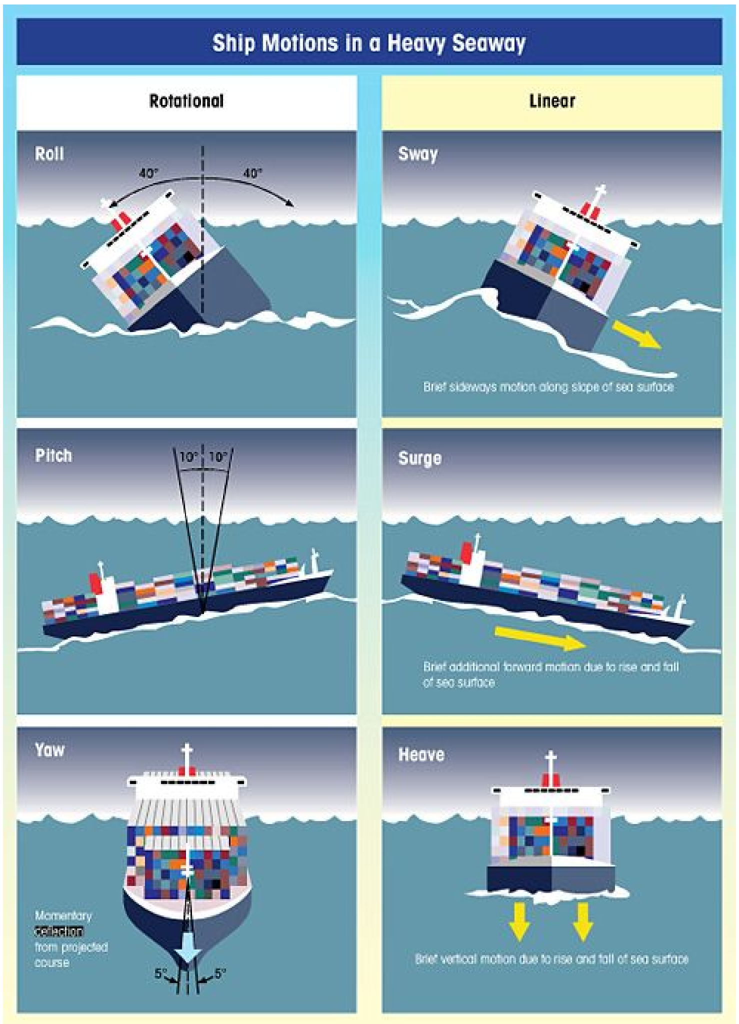

Figure 1.2 Six types of ship motions (taken from “JK Moving & Storage, Inc”)

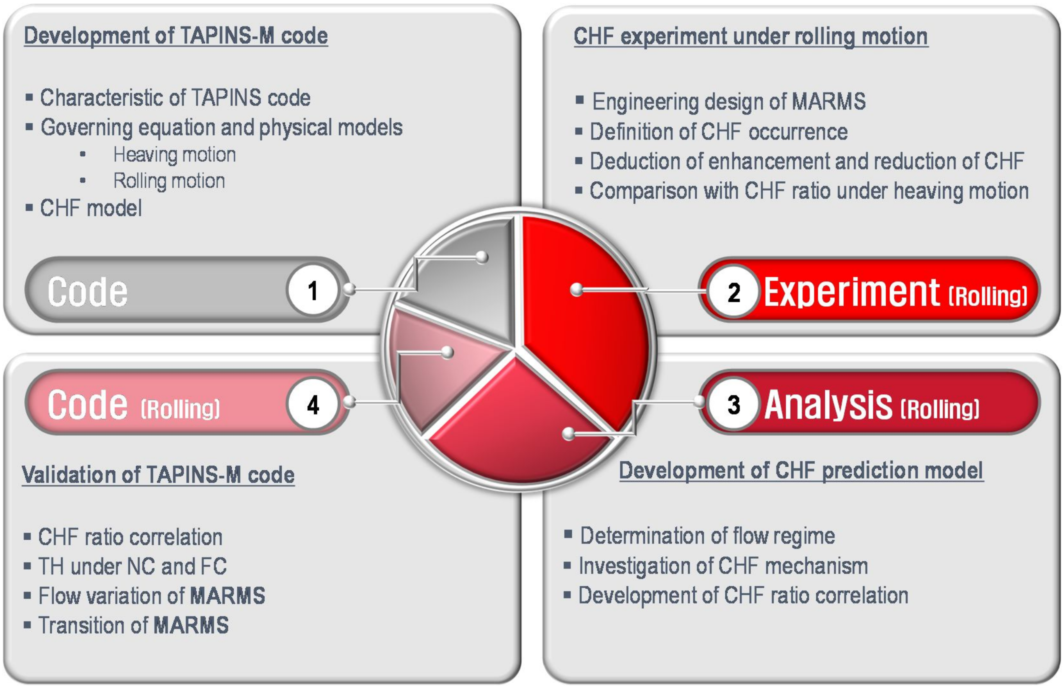

Figure 1.3 Outline of the study

Chapter 2

Literature Survey

2.1 Introduction

The most prominent characteristic of a marine reactor is that it is operated during the long voyage over the ocean. On the ocean, a marine reactor suffers from the dynamic motions such as rolling and heaving. Accordingly, the thermal-hydraulic behavior of marine reactor can be influenced by rolling and heaving motions. Ship motions affects flow patterns, instability, heat transfer and CHF in coolant channel. Among them, a prediction of the CHF characteristic is a crucial factor to a marine reactor safety and its design.

In this chapter, previous studies on the thermal-hydraulics and CHF related to a marine reactor will be reviewed.

2.2 Previous Studies on Marine Reactor

2.2.1 Thermal-Hydraulic Study on Heaving Motion

Various reports (Woodward, 1965; Chang et al., 1997, Isshiki, 1965; Otsuji et al., 1982) have been published on the aspect of marine reactors; some of these reports considered the relation of gravitational acceleration and CHF. Although a few CHF correlations contain a gravity term, each correlation has some limitation on the range of application. To resolve these deficiencies in existing CHF correlations, CHF experiments with gravity changes have been performed by researchers such as Chang, Isshiki, and Otsuji.

Woodward (1965) measured CHF in an oscillating force field using a natural circulation loop of R-113. Under the oscillating condition, CHF was always reduced from a corresponding value at steady state and that the maximum reduction rate reached 20%. In this experiment, however, the flow perturbation due to acceleration was very large, exceeding sometimes 100% of average flow rate, since the experiments were performed under the natural circulation condition. Hence the decrease in CHF was attributed to this large flow oscillation rather than direct effect of variation of acceleration. Although the result of this study includes some interesting events such as resonance between natural and forced oscillation of flow rate, the conditions of several points are far from actual situations which a marine reactor encounters.

Chang et al. (1997) proposed a CHF correlation that includes the acceleration effect. When the marine reactor is heaving, the net coolant flow rate decreases and the CHF is reduced. When it is in an upward motion, the fluid acceleration in the direction of gravity would increase, and the lift pressure drop would also increase. It is reported that the ratio of CHF under oscillation to CHF at stationary is proportional to the ratio of oscillating acceleration to gravitational acceleration to the power of one fourth. It can be expressed as:

$$q_c^{"} / q_{c,o}^{"} = \left(\Delta g / g_o\right)^{1/4} \tag{2.1}$$

Isshiki (1965) studied CHF under periodically changing gravity fields using a small water loop operated at atmospheric pressure. The experiments were conducted under both natural and forced circulation with a void fraction of more than 1.5% at the exit. The result is shown as follows:

$$q_c^{"} / q_{c,o}^{"} = 1 - \left(1 - y_{\min 0.8}\right) \Delta g / g_o \tag{2.2}$$

where $y_{\min 0.8}$ is the ratio of the minimum inlet velocity at $\Delta g = 0.8 g_o$ to the inlet velocity at $\Delta g = g_o$.

Otsuji et al. (1982) performed a series of single channel experiments with R-113 using a thermo-hydraulic loop that is capable of vertical movement. It was found that the CHF decreases quantitatively with oscillating gravity acceleration in a vertical direction. As a result, the CHF values obtained by Eq. 2.1 were smaller than almost all of the experimental data, regardless to quality and subcooling. A low limit of the CHF ratio was suggested as:

$$q_c^{"} / q_{c,0}^{"} = \left(1 - \Delta g / g_o\right)^n \tag{2.3}$$

where n is a constant that is dependent on both subcooling and the mass flow rate at the inlet. As these values increase, the value of n increases, and approaches 0.25. Figure 2.1 shows the variation of the CHF ratio depending on various gravity accelerations, and the comparison of the correlations can be shown as well. Also, Otsuji suggested that the CHF ratio is affected by inlet mass flow rate. Thus, he tried to found that the CHF ratio was reduced only by inlet mass flow rate. The low limit of the CHF ratio suggested by Otsuji cannot be satisfied because of the insufficient range of the experimental parameters.

Also, Hwang et al. (2011) performed an assessment on a code that predicts the CHF ratio with varying acceleration and it was further compared with Otsuji's data. The suggestions made in these researches are based on the Zuber's theory (1959) that CHF is proportional to the gravity acceleration to the power of one fourth in pool boiling.

2.2.2 Thermal-Hydraulic Study on Rolling Motion

Compared with the effects of inclining and heaving motions, those of a rolling motion are more complicated. An inclining motion only means a change in the effective height of the natural circulation flow loop, and a heaving motion only introduces an additional acceleration to the gravity acceleration. However, a rolling motion not only changes the effective height, but also introduces three additional accelerations; centripetal, tangential and Coriolis accelerations.

Murata et al. (1990, 2000, 2002), Tan et al. (2005, 2007, 2008) and Gao et al. (1999) experimentally studied natural circulation flow under rolling motion. Their results shows that the coolant mass flow rate changes periodically with the rolling angle owing to the inertial force caused by the rolling motion. Similar results were obtained in theoretical studies conducted by Fuji (1969), Gao et al. (1995, 1997), Su et al. (1996), Yang et al. (2002) and Guo et al. (2008). Because the additional inertia on a test loop varies depending on its distance from the rolling axis with different test apparatuses, the effects of rolling motion also differs. Using a test apparatus with two loops, Yang (2002) insisted that the fluctuation period of the natural circulation flow is half of the rolling period because of the effect of two circulation loops. However, the experimental results of Murata et al. (2002) showed that the fluctuation periods of natural circulation flow fluctuation in both the hot and cold legs are the same as the periods of the rolling motion, and the mass flow rate in the core does not oscillate. Using the test apparatus with a single loop, Tan et al. (2005, 2007, 2008) found that the period of flow fluctuation is the same as the rolling period. In Murata's et al. apparatus (2002), the axis of the rolling device lays above the top of the loop. In Tan's et al. experiment (2005, 2007, 2008), however, the axis is in the middle of the device in Gao's et al. experiment (1999) , it lays under the loop for Gao et al. Since the axes of each apparatus differ in location, the effects might be different. Though the previous research results confirm that the rolling motion induces a periodic fluid flow fluctuation, the effects of the system parameters on the characteristics of natural circulation flow have not yet been studied in detail. The heat transfer under rolling motion has been studied only by Murata et al. (2002). Their results show the heat transfer in the core is enhanced, which is thought to be caused by internal flow due to the rolling motion. Tan et al. (2009) experimentally studied two-phase flow instability of natural circulation under a rolling motion condition. Their results showed that rolling motion can cause an early onset of flow instability of natural circulation and it can change the types of flow instability such as trough-type flow oscillation or complex flow oscillation.

2.3 Previous Study on CHF

2.3.1 Theoretical Backgrounds

Flow patterns in a vertical heated tube

The CHF mechanism is governed by the flow pattern in vertical heated tube (Tong, 1982). The vapor generation forms a two-phase mixture in the tube and the heat flux through the tube wall alters the flow patterns which would have occurred in a long unheated tube at the same local flow conditions. It is due to two main reasons; firstly, the departure from the thermodynamic equilibrium which is relevant to the presence of radial temperature profiles in the channel and secondly, departure from local hydrodynamic equilibrium throughout the channel. The radial temperature profile in the liquid allows the vapor to be formed at the wall before the thermodynamic quality reaches zero. Also, a lack of thermodynamic equilibrium allows liquid drops to exit in the presence of superheated vapor close to the point of theoretically complete evaporation. The heat flux changes the local flow condition (expressed as the vapor quality) and then it results in the changes of flow pattern. The departure from hydrodynamic equilibrium conditions is caused by the difference between the change rates of the local flow condition and that of flow pattern. It affects the flow patterns in a vertical heated channel.

For the long evaporator tube with uniformly low heat flux and low inlet subcooling, vapor bubbles are initially formed. And then, the bubbles grow, and are detached to form a bubbly flow. With an increase of the bubble population along length, coalescence takes place to form slug which in turn gives way to annular flow further along the channel. Close to this point the formation of vapor at nucleation sites on the wall may cease and further vapor formation will be as a result of evaporation at the liquid film-vapor core interface. Increasing velocities in the vapor core will cause entrainment of liquid in the form of droplets. Depletion of the liquid from the liquid film by this entrainment and by evaporation finally causes the film to dry out completely.

The internal structures of the two-phase flow are classified by the flow regimes or flow patterns. Since various transfer mechanisms between two-phase mixture depend on the flow regimes, regime dependent correlations have been used together with two-phase flow regime criteria. The flow regimes have been based on the liquid and gas superficial velocities or the total mass flux and quality.

Basic mechanisms of CHF

When the flow is in the highly subcooled condition at the entrance, only fluid convection can be observed. After the coolant is heated in the channel through the tube wall, one can observe the regime of the nucleate boiling. Its features include separate vapor bubbles that nucleate and grow at the heater. In this regime, the heat transfer rate is very large due to both the phase change (latent heat of evaporation) and the fact that the superheated liquid is carried away from the heating surface by the departing vapor bubbles. Therefore, the boiling curve slop is larger than for the convection regime. The temperature of the heating surface increases with the heat flux. When the latter exceeds a critical value, CHF, the vapor bubbles on the heating surface abruptly from a film that thermally insulates the heater from the liquid; the surface of heater dries out. This is the film boiling regime. During the transition from nucleate to film boiling, the heat transfer is blocked and the temperature of the heater rapidly grows and can lead to its burnout. This phenomenon is known as "boiling crisis", "CHF phenomenon", or "Departure from Nucleate Boiling, DNB". The CHF value depends on various parameters of the system.

Correct CHF estimation requires a clear understanding of the physical phenomenon that triggers the boiling crisis. Numerous models were proposed where completely different mechanisms are assumed to be responsible for the different regimes of boiling. For concepts that appear to have been reasonably well-established experimentally include (Semeria, 1972):

- Formation of a hot spot under the growing bubble; when a bubble grows at the heated wall, a dry patch forms underneath the bubble as the micro-layer of liquid under the bubble evaporates. In this dry zone, the wall temperature rises due to the deterioration of the heat transfer. When the bubble departs, the dry patch may be rewetted and the process repeats itself. However, if the temperature of the dry patch becomes too high, then rewetting does not take place and gross local overheating occurs.
- Near-wall bubble crowding and inhibition of vapor release; a "bubble boundary layer" builds up on the surface and the vapor generated by boiling at the surface must escape through this boundary layer. When the boundary layer becomes too crowded with bubbles, the vapor escape is impossible and the surface becomes dry and overheated, giving rise to burnout.
- Dryout under a slug or vapor clot; in the plug or slug flow, the thin film surrounding the large bubble may dry out giving rise to localized

overheating and, hence, burnout. Alternatively, a stationary vapor slug may be formed on the wall with a thin film of liquid separating it from the wall; in this case, localized dryingout of this film gives rise to overheating and burnot.

- Film dryout in annular flow; in annular flow, the liquid film dries out due to evaporation and due to the partial entrainment of the liquid in the form of droplets into the vapor core. This mechanism is detail below. One should note that each of these mechanisms has a direct relation to the two-phase flow regime in which CHF occurs; e.g., bubble crowding in subcooled nucleate boiling, vapor clotting in slug flow, or film dryout in annular flow. Thus, CHF is fundamentally a condition where liquid cannot rewet the heater wall because the rate of vapor production impedes the liquid flow back to the hot surface. The flow regime changes due to variations in mass velocity, pressure, or the geometry of the particular mechanism that prevents the liquid from rewetting the heater surface, the basic principle remains the same.

Relationship between CHF mechanism and flow regime

The cause of dryout is different in each two-phase flow patterns. At low qualities, the flow regime is either bubbly flow or annular flow with a thick liquid film on the wall. In the bubbly flow, CHF occurs due to an inadequate removal of bubbles from the wall (DNB-type dryout). Cooling by liquid flow is effective only at the outside of the bubble boundary layer, so that the influence of flow rate on the CHF is not significant in the subcooled region. But, the effect of liquid subcooling on it is strong because the subcooled liquid flow condenses steam bubbles and suppresses their coalescence.

In the slug flow region, the CHF is affected by the thickness and the length of liquid film beneath the slug bubble and its passing velocity. It was ascertained that the liquid film dried out even at lower heat flux than the CHF due to fluctuating features of slug bubbles. But, most of partial dryouts will be rewetted by passing of consecutive liquid slugs. Therefore, the CHF due to partial dryout of liquid film beneath the slug bubble is determined by whether the partial dry patch can be rewetted or not.

As quality increases in slug region, the flow pattern changes to the annular flow which is comparatively stable. In this region, CHF occurs due to a depletion of the liquid film on the wall except for an extremely high heat flux, where dry patch by bubbles is generated in the thick liquid film layer due to the high heat flux, and the occurrence of CHF is determined by whether the dry patch is rewetted again or not. An amount of entrainment at the onset of annular flow will determine the CHF mechanism in this region because a large amount of entrainment at the onset of annular flow reduces the initial film thickness. The CHF occurs when liquid film is dried out due to droplet entrainment and evaporation from the liquid film. Therefore, the entrainment is ascertained to major CHF mechanism in this region and it is called as entrainment-controlled film dryout. The CHF vs. critical quality curve in this region is smooth; hence, there is a gradual change in the CHF mechanism between DNB- and entrainment-controlled dryout.

At higher flow qualities, the flow regime is annular-mist flow. The interface shear stress between a vapor and a liquid film flow increases due to increase of vapor velocity. Accordingly the droplet entrainment increases, and then thickness of the liquid film decreases. Generally, it seemed that nucleate boiling was suppressed due to the efficient cooling by evaporation. The primary supply of liquid to the film is through deposition from the entrained droplets in the core region (deposition-controlled dryout). Most of the liquid fed to the tube is wasted away by evaporation from the thin liquid film, and thereby the CHF condition is introduced, so that sometimes this type of CHF can be said evaporation-controlled dryout. In case of the high heat flux, the droplet deposition is suppressed by a strong vapor effusion from the liquid film due to high heat flux. It might interrupt the smooth change in the CHF vs. critical quality curve; hence, the changeover to deposition-controlled dryout takes place in the limiting quality region, where the CHF drops sharply, compared to the smooth decline in CHF with critical quality elsewhere and due to high heat flux.

CHF scaling theories and techniques

(A) General theory

Strictly speaking, in fluid-to-fluid scaling, geometric and dynamic similarities should be matched. Usually, by using the same *L/D* ratio in model and prototype, geometric similarity is achieved as follow;

$$\left(\frac{L}{D}\right)_M = \left(\frac{L}{D}\right)_W \tag{2.4}$$

Where subscript "*M*" denotes the modeling (or scaling) fluid and subscript "*W*" indicates the equivalent value for the water or prototype system. The dynamic similarities include thermodynamic qualities in both systems are the same at any axial location *z/D* along the lengthwise,

$$x(z)_M = x(z)_W \tag{2.5}$$

from the heat balance equation,

$$x(z) = 4\left(\frac{\phi_c}{\lambda G}\right)\left(\frac{z}{D}\right) - \left(\frac{\Delta h_i}{\lambda}\right) \tag{2.6}$$

where the Δh_i is the inlet subcooling enthalpy. It follows that the dimensionless groups also should be equal

$$Bo = \left(\frac{q_c''}{\lambda G}\right)_M = \left(\frac{q_c''}{\lambda G}\right)_W \tag{2.7}$$

and

$$X_i = \left(\frac{\Delta h_i}{\lambda}\right)_M = \left(\frac{\Delta h_i}{\lambda}\right)_W \tag{2.8}$$

where *Bo* is the so-called boiling number and X_i is the inlet subcooling quality. For hydrodynamic similarity, a similar density ratio in both systems is required,

$$\left(\frac{\rho_l}{\rho_v}\right)_M = \left(\frac{\rho_l}{\rho_v}\right)_W \tag{2.9}$$

as well as the dimensionless mass flux in both systems

$$G_M^* = G_W^* \tag{2.10}$$

where G^* is derived based on the classical dimensional analysis associated with experimental evidence and can be expressed in various ways depending on the investigators (Steven and Kirby (1964), Dix (1970) and Ahmad (1973)).

To convert the scaling fluid parameters into water-equivalent system parameters requires the introduction of the scaling factors as follows;

$$F_D = \frac{D_W}{D_M} \tag{2.11}$$

$$F_G = \frac{G_W}{G_M} \tag{2.12}$$

$$F_{\Delta H_i} = \frac{\left(\Delta h_i\right)_W}{\left(\Delta h_i\right)_M} = \frac{\lambda_W}{\lambda_M} \tag{2.13}$$

$$F_{CHF} = \frac{\left(q_c^{"}\right)_W}{\left(q_c^{"}\right)_M} = F_G \cdot F_{\Delta H_i} \tag{2.14}$$

(B) Scaling laws and factors

Barnett's CHF scaling laws

Barnett (1963) employed classical dimensional analysis to find the most likely scaling laws which describe the boiling heat transfer for forced convection of a vertical upflow in a uniformly heated tube. He found that there are six quantities of system parameters representing the occurrence of a burnout situation at particular combinations. These parameters are tube diameter, tube length, inlet pressure, outlet pressure, inlet temperature, and heat flux. The relation of these parameters can be written as

$$q_c^{"} = f\left(L, D, P_i, P_o, T_i\right) \tag{2.15}$$

where $q_c^{''}$ represents the critical heat flux and is treated as a dependent variable. Then, the mass flux is used instead of P_o, ρ_l / ρ_v is used to replace P_i to ensure that the voidage is scaled under steady conditions and the inlet subcooling of enthalpy is used to substitute T_i. Thus, Eq. 2.15 becomes

$$q_c'' = f\left(L, D, \rho_l / \rho_v, G, \Delta h_i\right) \tag{2.16}$$

He considered P_i and the corresponding saturation temperature to be the significant conditions from which to select the properties required in non-dimensionalized Eq. 2.16. Therefore, the liquid density, vapor density, thermal conductivity of liquid phase, k_f, specific heat of liquid phase, C_{pf}, and heat of vaporization are evaluated at the conditions of P_i and its corresponding saturation temperature. In addition to these properties, two other properties may be used if the analysis shows that they are required. They are the surface tension, σ, and the sloped of the saturation temperature vs. pressure, which is expressed as

$$\beta = \frac{dT_{sat}}{dP} \tag{2.17}$$

Barnett suggested that the properties of ρ_l, ρ_v and λ are obviously important in the case of forced-convection boiling heat transfer because their presence ensures that the mean condition of voidage and quality are correctly scaled. Also, ρ_l and ρ_v could be combined as the density ratio of liquid to vapor which is a significant parameter for evaluating void fraction and slip ratio and is a unique function of pressure: it is always possible to find pressures for which any two fluid have the same value of ρ_l / ρ_v. Therefore, he conducted 14 possible sets of scaling laws with the help of examining the experimental data for water and R-12, and based on the consideration that those possible sets of scaling laws contain only one dimensionless group, ρ_l / ρ_v, which involves only properties. These 14 possible sets of scaling laws are illustrated in Table 2.1. The scaling laws contain various fluid properties, including γ, which has not been introduced before and is defined as

$$\gamma = \frac{-d\left(\rho_l / \rho_v\right)_{sat}}{dP} \tag{2.18}$$

After testing the 14 sets of scaling laws by comparing the water-equivalent CHF of R-12 with actual water data, he included that the scaling law 4 shown in Table 2.1 gives the best comparison between the actual and equivalent water CHF data (within ±6%). Scaling law 4 is written as

$$\frac{q_c^{"}\gamma^{1/2}}{\lambda\rho_l^{1/2}} = f\left(\frac{L}{D}, \frac{DC_{P_f}\rho_l^{1/2}}{k_l\gamma^{1/2}}, \frac{G\gamma^{1/2}}{\rho_l^{1/2}}, \frac{\rho_l}{\rho_v}, \frac{\Delta h_i}{\lambda}\right) \tag{2.19}$$

To use Eq. 2.19, each dimensionless group at the right hand side should be equal in both fluid systems. Then the value of the dimensionless CHF at the left hand side in Eq. 2.19 will be the same in both fluid systems.

Stevens and Kirby's mass flux scaling factor

Stevens and Kirby (1964) presented a graphical correlation to scale the CHF data of R-12 at 10 bar to those of water at 70 bar for vertical upflow in uniformly heated round tubes. For the same values of ρ_l / ρ_v in water at 70 bar and in R-12 at 10 bar, They proposed that if

$$\left(\frac{L}{D}\right)_F = \left(\frac{L}{D}\right)_W \tag{2.20}$$

$$\left(\frac{\Delta h_i}{\lambda}\right)_F = \left(\frac{\Delta h_i}{\lambda}\right)_W \tag{2.21}$$

$$\left(GD^{1/4}\right)_F = \left(KGD^{1/4}\right)_W \quad \textit{where } K\text{=0.658} \tag{2.22}$$

$$\left(\frac{q_c^{"}}{\lambda G}\right)_F = \left(\frac{q_c^{"}}{\lambda G}\right)_W \tag{2.23}$$

where subscript "F" indicates the Freon system and the subscript "W" refers to the water system.

To obtain the water-equivalent CHF from a R-12 system, requires the use of several scaling factors for various system parameters,

$$\left(q_c^{"}\right)_W = F_\phi \left(q_c^{"}\right)_F \tag{2.24}$$

$$\left(\frac{\Delta h_i}{\lambda}\right)_F = \left(\frac{\Delta h_i}{\lambda}\right)_W \tag{2.25}$$

$$\Delta h_{i,W} = F_{\Delta H_i} \Delta h_{i.F} \tag{2.26}$$

$$G_W = F_G G_F \tag{2.27}$$

$$D_W = F_D D_F \tag{2.28}$$

$$L_W = F_L L_F \tag{2.29}$$

Substituting Eqs. 2.24-2.29 into Eqs. 2.20-2.23, yields

$$F_L = F_D \tag{2.30}$$

$$F_{\Delta H_i} = \frac{\lambda_W}{\lambda_F} \tag{2.31}$$

$$F_{CHF} = \frac{\lambda_W}{\lambda_F} F_G \tag{2.32}$$

$$F_G = \frac{1}{K} \times F_D^{-1/4} \tag{2.33}$$

Where ρ_l / ρ_v=20.63, K=0.658.

Coffield et al.'s subcooled DNB investigation of R-113

Coffield et al. (1969) measured the DNB type of dryout for R-113 flowing vertically through a uniformly heated round tube. These subcooled CHF data were used to examine Barnett's and Stevens and Kirby's scaling techniques, which were developed for the low and high quality CHF conditions. Coffield et al. found that both the Barnett's and Stevens and Kirby's methods simulate the subcooled R-113 CHF data to the equivalent subcooled water CHF data within ±15%, that is, the methods of Barnett and Steven and Kirby can be extended to the subcooled region. However, Steven and Kirby's scaling technique was recommended by Coffied et al. because of the convenience of selecting a diameter scaling factor. Coffield et al. concluded that the value of constant *K* in Steven and Kirby's scaling function varies with the density ratio.

They proposed a scaling factor technique that was successful for CHF modeling in the subcooled boiling flow. He also derived a dynamic similitude from dimensional analysis that was based on a CHF relationship originally suggested by Barnett (1963) as,

$$q_c^{''} = f(L, D, G, \rho_l / \rho_g, \Delta h_i, h_{lg}, C_{pl}, k_l, \gamma) \tag{2.34}$$

According to the dimensionless analysis using these parameters, he made dimensionless parameters and expressed the modeling parameter as,

$$\frac{q_c^{''}\gamma^{1/2}}{h_{lg}\rho_l^{1/2}} = f\left(\frac{L}{D}, \frac{DC_{pf}\rho_l^{1/2}}{k_l\gamma^{1/2}}, \psi_{\text{Coffield}}, \frac{\rho_l}{\rho_g}, \frac{\Delta h_i}{h_{lg}}\right) \tag{2.35}$$

$$\psi_{\text{Coffield}} = G\sqrt{\frac{\gamma}{\rho_l}} \tag{2.36}$$

Ahmad's Scaling Technique

Ahmad (1973) proposed a FTF scaling with a compensated distortion model using a nondimensional parameter matrix affecting the CHF for the boiling heat transfer. Ahmad deduced 13 dimensionless numbers from the parameters, as shown in Eq. 2.37, which are based on the dimensional analysis and a lot of experimental data.

$$f(q_{CHF}, G, \Delta h_{in}, L, D, g_o, h_{lg}, \rho_l, \rho_g, \mu_l, \mu_g, C_{Pl}, C_{Pg}) \tag{2.37}$$

He chose seven important dimensionless groups for CHF by applying Buckingham's Pi theorem (Buckingham, 1914) to the dimensionless equation, which is expressed as:

$$\frac{q_c''}{GH_{lg}} = f\left(\psi_{Ahmad}, \frac{\Delta h_{in}}{h_{lg}}, \frac{\rho_l}{\rho_g}, \frac{L}{D}\right) \tag{2.38}$$

where ψ_{Ahmad} can be presumed to be the modeling parameter for a dimensionless mass flux

$$\psi_{\text{Ahmad}} = \Lambda_1 \Gamma_1^{4/3} \Gamma_2^{-1/5} \tag{2.39}$$

where $\Lambda_1 = \dfrac{GD}{\mu_l}$, $\Gamma_1 = \dfrac{\mu_l}{(\sigma D \rho_l)^{1/2}}$, $\Gamma_2 = \dfrac{\mu_l}{\mu_g}$

If Eqs. 2.4, 2.8 and 2.9 and $(\psi_{\text{Ahmad}})_W = (\psi_{\text{Ahmad}})_M$ are satisfied, then dimensionless CHF (i.e., boiling number) of the left hand side of Eq. 2.38 should be the same for both fluids.

$$\left(\frac{q_c''}{GH_{lg}}\right)_W = \left(\frac{q_c''}{GH_{lg}}\right)_M \tag{2.40}$$

Katto's generalized correlation of CHF

Katto (1978) presented the generalized correlation of CHF of flow boiling in uniformly heated vertical tubes. In the Katto correlation, the following rather simple relationship is presented using five parameters instead of seven parameters used by Ahmad (1973).

$$\frac{q_c^{"}}{Gh_{lg}} = f\left(\frac{L}{D}, \frac{\rho_l}{\rho_g}, \frac{\Delta h_i}{h_{lg}}, \frac{\sigma\rho_l}{G^2 L}\right) \tag{2.41}$$

Katto assumed that five dimensionless groups in Eq. 2.41 govern the CHF in vertical uniformly heated tube. Under this assumption, Katto proposed the following a non-dimensional mass flux parameter

$$\psi_{\text{Katto}} = \frac{GD^{1/2}}{\left(\sigma\rho_l\right)^{1/2}} \tag{2.42}$$

Based on this parameter, mass velocity scaling factor was introduced and it was reported that the prediction of the scaling factor Eq. 2.42 agreed with the experimental data of CHF obtained for R-114, -12, -22 and -21 by Dix (1970) and compared the prediction values with Ahmad's prediction.

2.3.2 Previous Analytical and Experimental Works

CHF enhancement

Since the heaving and rolling are periodic motions, vibration is an important factor that should be considered for taking into account of effects of such motions on the CHF in the marine reactors. Lee et al. (2004) experimentally investigated relationship between CHF and flow-induced vibration (FIV) with vertical round tube at the atmosphere. They presented that CHF increased with vibration intensity, represented by vibrational Reynolds number (Re_v) in the both condition of DNB and LFD as shown in Table 2.2. Kim et al. (2007) performed an experimental study on CHF at atmospheric pressure in vertical annulus tube under FIV. They found that the most effective on CHF was vibration amplitude, but vibration frequency and mass flux had no significant effect on CHF enhancement. They supposed that reinforced turbulent mixing effect of vibration makes CHF enhanced.

Twisted-tape swirl generator (Kim et al., 2005; Jensen, 1984) have been studied for various two-phase flow conditions, with the main emphasis being placed on determining the effect of twisted-tape inserts on the suppression of the CHF data, which have been obtained with several fluids, fluid conditions and tape geometries. Kim et al. (2005) conducted the CHF experiments in the smooth tube, four-head and six-head rifled tubes. Their investigation showed that the CHF enhancement depends on the mass flux and pressure. They explained characteristics of the CHF performance using the relative vapor velocity on the pressure, helical angle and velocity. They supposed the CHF enhancement in the rifled tube is achieved by extending the nucleate boiling region to the higher quality.

CHF reduction

There are also some important mechanisms that must be considered since they negatively impact on CHF under oscillatory motions. Umekawa et al. (1996)

carried out an experimental investigation on CHF in upward/downward flows under oscillatory flow conditions with predetermined amplitude and period using an oscillator. The experimental results show that under both upflow and downflow oscillation conditions, the CHF decreased significantly with an increase in the amplitude and period of flow oscillation, especially at intermediate mass flow rate, and that there is no upward and downward flows. Kim et al. (1999) experimentally investigated the effect of flow oscillation on CHF for water in vertical round tubes at low pressure and low flow conditions. They found that flow oscillations at higher mass flow rates significantly decrease the CHF for both forced and natural circulation, and the reduction of the CHF in natural circulation is larger than that in forced circulation even with the similar conditions: average mass flow rate, oscillation amplitude and period are same. They also found that flow circulation mode does not affect the CHF as long as the flow is maintained sufficiently stable, and there is no difference in the CHF between natural and forced circulation at low flow regions below the threshold mass flow rate of ~100 kg/m^2s due to the experimental condition in natural circulation with the flow maintained at a stable rate with high throttling. Kim et al. defined a CHF correction factor F as shown in Table 2.3. Okawa et al. (2009) supposed the transient CHF was associated with the instantaneous dryout of liquid film wave at outlet. A one-dimensional three-fluid model taking into consideration the effect of axial mixing in the liquid film was developed. They suggested that disturbance waves forming on the surface of the liquid film might have contributed to enhancing the axial mixing of the liquid film. Zhao et al. (2011) conducted transient CHF experiments with forced sinusoidal inlet flow oscillation in a vertical tube under low pressure condition. The results of their study indicated that

CHF remarkably decreased as flow oscillation increased due to the liquid film oscillation. The changing trends of the periodic dryout heat flux showed a reasonable agreement with Okawa's theoretical model, in which the liquid film oscillation was supposed to be weakened by the axial mixing of liquid film.

Table 2.1 Possible sets of scaling laws (Barnett, 1964)

Set No.	Physical properties assumed important in addition to λ, ρ_l and ρ_g	Resulting dimensionless equation assuming $q_c^{"}=f(L,D,G,P,\Delta h_i)$	Implied ratio of variable in water at 1000 psi and R-12 at 155 psi, i.e. the scaling factor *F*			
			F_L	F_G	$F_{\Delta h_i}$	$F_{q_{ci}^{"}}$
1	Cp_l, k_l, β	$\frac{q_c^{"}\beta^{1/2}Cp_l^{1/2}}{\lambda^{3/2}\rho_l^{1/2}} = f\left(\frac{L}{D}, \frac{DCp_l^{1/2}\lambda^{1/2}\rho_f^{1/2}}{k_f\beta^{1/2}}, \frac{G\beta^{1/2}Cp_f^{1/2}}{\lambda^{1/2}\rho_f^{1/2}}, \frac{\rho_l}{\rho_g}, \frac{\Delta h_i}{\lambda}\right)$	0.588	2.33	11.72	27.32
2	Cp_l, k_l	$\frac{q_c^{"}}{\rho_l\lambda^{3/2}} = f\left(\frac{L}{D}, \frac{DCp_l\lambda^{1/2}\rho_f}{k_f}, \frac{G}{\lambda^{1/2}\rho_l}, \frac{\rho_l}{\rho_g}, \frac{\Delta h_i}{\lambda}\right)$	0.669	2.053	11.72	24.08
3	Cp_l, k_l, σ	$\frac{q_c^{"}k_f}{\lambda\sigma\rho_l Cp_l} = f\left(\frac{L}{D}, \frac{D\sigma Cp_l\rho_f}{k_f^{2}}, \frac{Gk_f}{\sigma Cp_l\rho_l}, \frac{\rho_l}{\rho_g}, \frac{\Delta h_i}{\lambda}\right)$	1.155	1.189	11.72	18.92
4	Cp_l, k_l, γ	$\frac{q_c^{"}\gamma^{1/2}}{\lambda\rho_f^{1/2}} = f\left(\frac{L}{D}, \frac{DCp_l\rho_f^{1/2}}{k_f\gamma^{1/2}}, \frac{G\gamma^{1/2}}{\rho_l^{1/2}}, \frac{\rho_l}{\rho_g}, \frac{\Delta h_i}{\lambda}\right)$	0.717	1.914	11.72	18.92
5	β, k_l, γ	$\frac{q_c^{"}\gamma^{1/2}}{\lambda\rho_f^{1/2}} = f\left(\frac{L}{D}, \frac{D\lambda\gamma^{1/2}\rho_f^{1/2}}{\beta k_f}, \frac{G\gamma^{1/2}}{\rho_l^{1/2}}, \frac{\rho_l}{\rho_g}, \frac{\Delta h_i}{\lambda}\right)$	0.482	1.914	11.72	22.43
6	σ, μ_l	$\frac{q_c^{"}\mu_l}{\lambda\sigma\rho_f} = f\left(\frac{L}{D}, \frac{D\sigma\rho_f}{\mu_l^2}, \frac{G\mu_l}{\sigma\rho_l}, \frac{\rho_l}{\rho_g}, \frac{\Delta h_i}{\lambda}\right)$	0.101	4.007	11.72	46.95
7	σ, μ_g	$\frac{q_c^{"}\mu_g}{\lambda\sigma\rho_f} = f\left(\frac{L}{D}, \frac{D\sigma\rho_f}{\mu_g^2}, \frac{G\mu_g}{\sigma\rho_l}, \frac{\rho_l}{\rho_g}, \frac{\Delta h_i}{\lambda}\right)$	1.488	1.407	11.72	46.95
8	μ_l, γ	$\frac{q_c^{"}\gamma^{1/2}}{\lambda\rho_f^{1/2}} = f\left(\frac{L}{D}, \frac{D\rho_f^{1/2}}{\mu_l\gamma^{1/2}}, \frac{G\gamma^{1/2}}{\rho_l^{1/2}}, \frac{\rho_l}{\rho_g}, \frac{\Delta h_i}{\lambda}\right)$	0.212	1.914	11.72	12.27
9	μ_l, k_l, β	$\frac{q_c^{"}\beta^{1/2}k_f^{1/2}}{\lambda\rho_f^{1/2}} = f\left(\frac{L}{D}, \frac{D\rho_f^{1/2}}{\mu_l\gamma^{1/2}}, \frac{G\gamma^{1/2}}{\rho_l^{1/2}}, \frac{\rho_l}{\rho_g}, \frac{\Delta h_i}{\lambda}\right)$	0.320	1.270	11.72	14.87
10	μ_l, γ	$\frac{q_c^{"}\gamma^{1/2}}{\lambda\rho_f^{1/2}} = f\left(\frac{L}{D}, \frac{D\rho_f^{1/2}}{\mu_g\gamma^{1/2}}, \frac{G\gamma^{1/2}}{\rho_l^{1/2}}, \frac{\rho_l}{\rho_g}, \frac{\Delta h_i}{\lambda}\right)$	0.814	1.914	11.72	22.43
11	σ, γ	$\frac{q_c^{"}\gamma^{1/2}}{\lambda\rho_f^{1/2}} = f\left(\frac{L}{D}, \frac{D}{\sigma\gamma}, \frac{G\gamma^{1/2}}{\rho_l^{1/2}}, \frac{\rho_l}{\rho_g}, \frac{\Delta h_i}{\lambda}\right)$	0.445	1.914	11.72	22.43
12	Cp_g, k_g, β	$\frac{q_c^{"}\beta^{1/2}Cp_g^{1/2}}{\lambda^{3/2}\rho_f^{1/2}} = f\left(\frac{L}{D}, \frac{DCp_g^{1/2}\lambda^{1/2}\rho_l^{1/2}}{k_g\beta^{1/2}}, \frac{G\beta^{1/2}Cp_g^{1/2}}{\lambda^{1/2}\rho_l^{1/2}}, \frac{\rho_l}{\rho_g}, \frac{\Delta h_i}{\lambda}\right)$	0.371	1.968	11.72	23.06
13	Cp_g, k_g, γ	$\frac{q_c^{"}\gamma^{1/2}}{\lambda\rho_f^{1/2}} = f\left(\frac{L}{D}, \frac{DCp_g\rho_l^{1/2}}{k_g\gamma^{1/2}}, \frac{G\gamma^{1/2}}{\rho_l^{1/2}}, \frac{\rho_l}{\rho_g}, \frac{\Delta h_i}{\lambda}\right)$	0.381	1.914	11.72	22.43
14	Cp_g, k_g, σ	$\frac{q_c^{"}k_g}{\lambda\sigma\rho_l Cp_g^2} = f\left(\frac{L}{D}, \frac{D\sigma Cp_g^2\rho_l}{k^2_g}, \frac{Gk_g}{\sigma\rho_l Cp_g}, \frac{\rho_l}{\rho_g}, \frac{\Delta h_i}{\lambda}\right)$	0.626	2.487	11.72	29.13

Table 2.2 CHF enhancement correlations

Source	**Correlation**	**Condition(s)**
Lee et al.	$En = 1 + 0.00112\,\mathrm{Re}^{-0.11}\,\mathrm{Re}_V^{0.72(1+0.27x)^{0.1}},\ 0 < a \le 0.5\ mm$ $En = 1 + 0.00112\,\mathrm{Re}^{-0.11}\,\mathrm{Re}_V^{0.72(1+0.27x)^{0.5}},\ 0.5 < a \le 1.0\ mm$	- Vibration - Atmospheric - Vertical tube
Kim et al.	$En = 0.06825(a)^{0.61683}$	- Vibration - Atmospheric - Vertical annulus
Jensen	$En = \left(4.597 + 0.09254y + 0.004154y^2\right)\left(\rho_l / \rho_g\right)^{-0.7012} + 0.09012\ln\left(a / g\right)$	- Twist-tape

*En=CHF enhancement

**x=thermal equilibrium exit, $x = 1 / h_{fg}\left[\left(4q_c L / DG\right) - \left(\Delta h_i\right)\right]$

***y=tape-twist ratio, y=(distance for 180^{o} turn)/(tube diameter)

Table 2.3 CHF Reduction correlations

Source	**Correlation**	**Condition (s)**
Kim et al.	$F_p = 1 - \left(\frac{\Delta G_{\max}}{G_{avg}}\right)^{0.4606}\left(\frac{\tau}{T_{tr}}\right)^{0.215}\left(\frac{\sigma\rho_l}{G_{avg}^2 D_i}\right)^{-0.1366}\left(\frac{\Delta h_i}{h_{lg}}\right)^{0.591}$	- Inlet flow oscillation - Forced circulation
Okawa et al.	$F_p = 1 - \left(1 - \tanh\left(0.4\frac{2L_h}{\tau u_{fo}}\right)\right)\left(1 - q_{\min,CHF} / q_{avg,CHF}\right),$ $u_{fo} = \frac{G_{vg}}{\sqrt{\rho_f \rho_v}}\left(\frac{\Delta G_{\max}}{G_{avg}}\right)^{-0.2}$	- Inlet flow oscillation - Forced and natural circulation
Zhao et al.	$F_p = F_{p,\lim} + \left(1 - F_{p,\lim}\right)e^{-2*\left(\frac{\Delta G_{\max}}{G_{vg}}\right)\left(\frac{t_{tr}}{\tau}\right)},$ $F_{p,\lim} = e^{-1.22*\left(\frac{t_{tr}}{\tau}\right)^{0.5}}$	- Inlet flow oscillation - Forced circulation

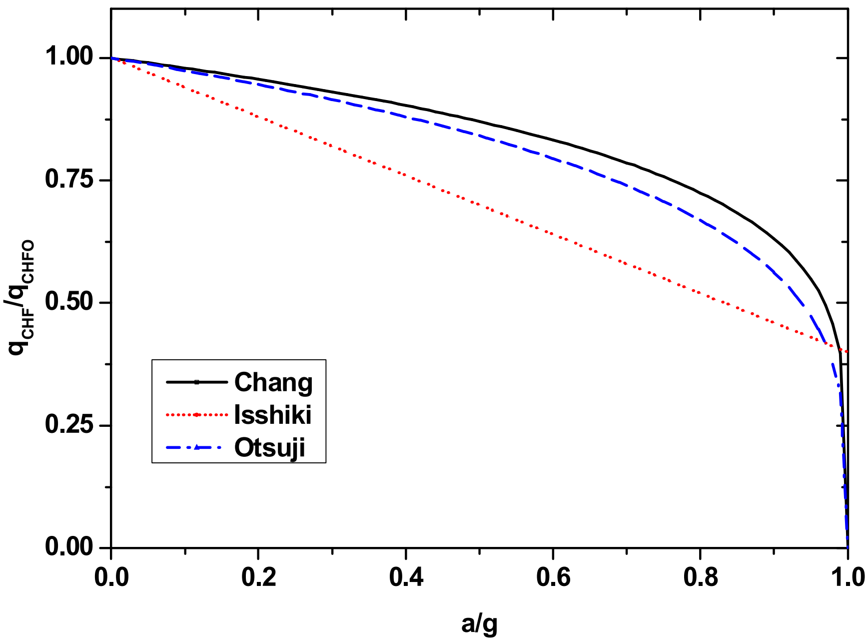

Figure 2.1 Reduction of CHF ratios as gravity acceleration

Chapter 3

Experimental Study on Thermal-Hydraulics for Rolling Motion in Marine Reactor

3.1 Experimental Set-up

3.1.1 Experimental Apparatus

The test facility, named MArine Reactor Moving Simulator (MARMS) is shown in Fig. 3.1. It is composed of a Freon circulation loop and rolling system as shown in Fig. 3.2. The Freon (R-134a) circulation loop consists of the following components: a test section, a non-sealed canned motor pump, manufacture by HALLA IND Co., LTD, for stable mass flow supply, a mass flowmeter, manufacture by RHEONK, a preheater for inlet temperature (inlet subcooling) control, a pressurizer (accumulator type) for pressure control of the loop system, a cooler (brazed type heat exchanger) for condensing the evaporated Freon, and a chilling system with water. A control valve, manufacture by KOPECS, located upstream of the test section is used to precisely control the flow rate in the test section. Also, it is used to avoid flow fluctuations, which are usually observed under low flow rate conditions. The loop is filled with R-134a with vacuum system. The test loop is designed for pressure of 40 bar and temperature of 200 ^{o}C. The loop flow is measured by Coriolis mass flowmeter calibrated to have 2% of RMS error by the manufacturer. Temperatures and pressures are measured at various locations as indicated by T and P, respectively, in Fig. 3.2(a). The design specification of MARMS is listed in Table 3.1.

Generally, it is difficult to determine the response characteristic of the ship motion on an actual sea by means of artificial wave with rolling device. It is because rolling motion of actual marine reactor is dependent on many parameters such as weight of the ship, transverse metacentric height, moment of inertia for the transverse axis of the ship, etc. The angle and period of rolling system were determined to follow the ship safety design criteria when designing the system. The rolling device consists of the loop stand, support, gear and motor to control the rolling motion as shown in Fig. 3.2(b). The loop stand is a 1m×1m square plane. Rolling axis located at the top of the device and the height is 1.5m between axis and stand. The rolling device is driven by the motor and gear from the Programmable Logic Controller, manufacture by LS IS. The rolling amplitude and period can be controlled by adjusting the revolution, speed of electromotor and the number of gear tooth. The rolling angle was measured in a clockwise direction perpendicular. The angular acceleration at each rolling amplitude and period were detected by two acceleration transducers, manufacture by SENSOREX; one in x-direction and the other in z-direction.

The test section is schematically shown in Fig. 3.3. It is stainless steel (SUS316) tube with upward flow. The tube is directly heated with a direct current (DC) power supply, manufacture by KAPJIN, which controls the power by a silicon controlled rectifiers (SCRs) with a maximum power capacity of 48 kW

(40V and 1200A). The heated length of test section is 1000 mm, the inside diameter and thickness are 9.5 mm and 1.65 mm, respectively. These geometric dimensions are selected to reflect the hydraulic diameter of a marine reactor core. The temperatures of the liquid at the inlet and outlet of the test section are measured with the T-type sheathed thermocouples. The temperatures of the outside wall are measured at 14 locations along the channel wall with K-type thermocouples. The first 4 thermocouples are installed at an interval of 5 mm from upper power electrode. Outlet pressure and inlet pressure are measured with a pressure transducer, manufacture by EMERSON, which is calibrated to have 0.5% of RMS error for a full range. The pressure difference of the test section is measured by a differential pressure and two pressure transducers. A pair of clamp-type copper electrodes is connected with both ends of the test tube. The test section is connected to the flange, which is insulated from other part of the test loop with Teflon. The supplied current and the voltage difference between both ends of the test section are measured and collected by a data acquisition system.

3.1.2 Test Procedure and Conditions

Experiments have been performed for upward flow of R-134a with changing inlet conditions such as pressure, mass flux, and inlet subcooling in loop and rolling conditions such as amplitude and period in rolling device. Before each experiment, a heat balance test under single-phase flow condition was performed to estimate the heat loss from the test section and to check a proper working of the test section instrumentation. In the heat balance testes, under the specific condition of inlet pressure, inlet temperature, and mass flow rate, total power applied to the test section is compared with the enthalpy rise of the fluid through it. The heat balance is estimated as follows

$$\eta = \frac{Q_T}{GA\left(h_o - h_i\right)} \times 100 \ (\%) \tag{3.1}$$

If the η is within 100±3%, the overall operation of the test loop was considered as to be pertinent and then the main test was started. In most of the tests, the heat loss was with η less than 100±1%.

The experiment was conducted as the following procedure below.

(1) The pump starts and the mass flow rate is controlled by inverter and the control valve.
(2) The system pressure in the Freon loop is increased by turning on the pre-heater and is controlled by venting and injecting the nitrogen gas in the accumulator.
(3) After the pressure in the loop reached a desired level, the inlet temperature is controlled by the pre-heater with SCR and the cooler with chiller.
(4) Power is applied to the test section and increased gradually in small steps while the inlet conditions of the test section are maintained at constant level.
(5) CHF is considered as a sharp and continuous rise of the wall temperatures of below the upper power terminal.
(6) In the case of rolling condition, the rolling device is switched on before power is applied to the test section.

The CHF change due to the rolling motion is smaller than ±20%. Since the difference is small, it has a possibility of overlapping within the range of scattered collected data of stationary CHF, which is caused by an insufficient accuracy of measurement of test conditions, device variation of the heater surface and probabilistic phenomenon of CHF mechanism. The CHF under rolling motion and stationary CHF were measured successively in order to obtain a reliable CHF ratio.

Table 3.2 summarizes the test matrix and the equivalent water-based conditions using fluid-to-fluid scaling. Since Katto's (1978a) scaling parameter has been successfully used for a scaling law, the present study uses the Katto's additional hydrodynamic similarity. Test conditions (i.e. pressure, mass flux and inlet subcooling) were converted by FTF scaling as follows;

A. Calculate the density ratio of liquid to vapor. Find the pressure at which the density ratio of Freon (R-134a) is equal to that of water.

$$\left(\frac{\rho_l}{\rho_g}\right)_{R134a} = \left(\frac{\rho_l}{\rho_g}\right)_{Water} \tag{3.2}$$

B. Calculate the mass flux scaling factor (F_G) with Katto's scaling parameter at the equivalent pressure as follows:

$$F_G = \frac{G_{Water}}{G_{R134a}} = \frac{\left(\sqrt{\sigma\rho_l}\right)_{Water}}{\left(\sqrt{\sigma\rho_l}\right)_{R134a}} \tag{3.3}$$

3.2 Experimental Result

3.2.1 Stationary CHF

In order to verify the CHF experiment under rolling condition, CHF was plotted at every stationary condition. For this work, the validity of the fluid-to-fluid modeling method was confirmed by comparing the CHF data converted from R-134a flow boiling experimental data with existing CHF value in water provided from CHF look-up table (Groeneveld, et al., 2006). The selected condition ranges in R-134a for comparison with CHF data in water are shown in Table 3.2. A sample of fluid-to-fluid converting process and comparison work is listed as follows.

Converting procedure form the R-134a CHF to Water-equivalent CHF

1. Select the one CHF with pressure, mass flux and exit quality (e.g. CHF = 105.19 kW/m^2 at 13 bar, 285kg/m^{2}s, x_{exit} = 0.75)
2. Determine the water equivalent condition using F_P, F_G, and assume geometry similarity is obtained (F_L = 1) (see Table 3.3).
3. Water equivalent pressure and mass flux condition become 80 bar (13 × F_p), and 402 kg/m^{2}s (285 kg/m^{2}s × F_G), respectively.
4. Determine the water equivalent CHF value using F_{CHF} (e.g. $CHF_{water\ equivalent} = F_{CHF} \times CHF_{R134a}$= 13.3 × 105.19 = 1399 kW/m^2)
5. Find the existing water CHF data from the CHF-look-up table under the

water equivalent condition (pressure: 80 bar, mass flux: 285 kg/m^{2}s, x_{exit}: 0.75). CHF value is selected as 1550 kW/m^2 from look-up table.

6. Compare between the water equivalents CHF converted from R-134a experimental test data using fluid-to-fluid method and the CHF look-up table result under identical water equivalent operating condition.

Figure 3.4 depicts the comparison of CHF test data at stationary in R-134a with the CHF data through the above process and work. The present CHF data is agreed to within a deviation of ±10% for water data of CHF Look-up table.

In the experiments, CHF occurred near the exit of the tube as it had the highest temperature along the tube. Stationary CHF was measured with varying mass flux, inlet subcooling and system pressure.

<u>Inlet subcooling and mass flux effects</u>

Figure 3.5 illustrate the effect of inlet subcooling on stationary CHF at various mass flow conditions. For vertical upward flow at stationary, CHF is obviously affected by inlet thermal condition. For the effect of inlet subcooling on CHF, general consistence (Moon, 1996) is that CHF is directly proportional to inlet subcooling enthalpy. The experimental study showed that those understandings could directly apply to the CHF in R-134a as working fluid.

The results are obtained at the pressures of 13 and 24 bar and the mass fluxes of 285, 500, 712, 1000 and 1300 kg/m^{2}s. The CHF increases almost linearly with inlet subcooling enthalpy, but the effect decreases with decreasing mass flux. The linear relationship between the CHF and inlet subcooling seems to be maintanined over all investigated pressure. It was observed from these results that the inlet subcooling effect is strongly dependent on the mass flux.

Pressure effect

Figure 3.6 shows the effect of pressure on CHF, indicating that CHF decreases with increasing pressure and the trends are similar in both of mass fluxes.

In annular flow, generally CHF mechanism as mentioned in previous section is governed by an onset of annular flow, evaporation rate, entrainment rate, and deposition rate. CHF is strongly affected by the pressure, since the change of the pressure results in the changes of surface tension, latent heat, and density ratio. The evaporation rate increases with the pressure increase because of low latent heat at a higher pressure.

The pressure effect on CHF in a forced convection has been shown to be complex and the trend was not clear as indicated by Collier (1982) and confirmed by Moon (1996). Moon presented that the CHF increases with pressure at low pressure, passes through a maximum, then decreases in the range of the medium pressure. Since the experiment pressure for R-134a corresponds to the intermediate pressure (80~140 bar) in the water condition by the fluid-to-fluid scaling, the present result seems to be consistent with trend in water.

Critical quality

Figure 3.7 depicts the CHF vs. the critical quality graph for the mass flux of

285, 500, 712 and 1000 kg/m^{2}s and pressure of 13, 16 and 24 bar. Critical quality is determined via the heat balance. The critical quality was calculated as follows;

$$x_c = \frac{q_c^{''}}{Gh_{lg}} - \frac{\Delta h_i}{h_{lg}} \tag{3.4}$$

This figure shows that a CHF decreases continuously with an increase of the critical quality without sharp change in slope. The CHF values at the higher mass flux is considered to be higher than those at the lower mass flux in consideration of the data trends at each test condition. It indicates that the inverse mass flux effects are present for all tests.

The observed linear variations of CHF with inlet subcooling, mass flux and pressure agree with the general understanding in many existing water data.

3.2.2 Variation of CHF under the Rolling Motion

The cases of present experiment are divided into loop conditions and rolling conditions. The loop conditions are represented by pressure, mass flux and inlet subcooling, The rolling conditions are considered by the amplitude and period of the rolling device. Each test is performed under the combined conditions of them. The combinations are summarized in Table 3.4. The CHF ratio is defined as that of the CHF under rolling condition to the CHF in stationary condition. The CHF ratio can be used to represent the effect of rolling motion.

An occurrence of the CHF in stationary state can be certainly determined with a rapid increase of the heater wall temperature after small increment of power. In contrast, in every case under the rolling motion, the wall temperature begins to oscillate with the rolling motion synchronously. A further increase in heat flux at the near CHF leads the wall temperature to oscillate more strongly. Finally, the wall temperature increases continuously without returning to the balanced value. Thus, it becomes difficult to recognize CHF under oscillating condition. In the present work, we define the CHF as a heat flux at which the wall temperature increases irreversibly as shown in Figs. 3.8 and 3.9. Arrows in Figs. 3.8 and 3.9 mean the time to increase heat flux.

3.2.3 Effect of Rolling Period on CHF

Figure 3.10 shows the effect of the rolling period on the CHF ratio at different inlet subcooling conditions. The slope of the CHF ratio decreases with increasing rolling period. The CHF ratio is dependent on inlet subcooling in condition of rolling period 6 seconds. However, effect of rolling motion on CHF ratio is reduced if it is longer than 6 seconds. For this reason, no more experiments that those in Fig. 3.10 were conducted in the present study.

3.2.4 Effect of Rolling Amplitude on CHF

Figures 3.11 and 3.12 show the effect of the rolling amplitude on CHF ratio at different pressure conditions. There are clear differences trend of CHF ratio between intermediate (13, 16 bar) and high pressure (24 bar) region.

At intermediate pressure, the CHF ratio tends to decreases as the rolling amplitude increases. In the cases of higher than 712 kg/m^2s mass flux, the CHF under rolling condition tends to become higher than that of the stationary condition. In high quality (i.e. low subcooling), the reduction rate of the CHF ratio gradually increases with increasing the rolling amplitude. As the mass flux increases, CHF ratio becomes independent on the effect of rolling amplitude. Furthermore, above a certain mass flux, change of the CHF ratio becomes negligible. However, all the CHF measurement results are enhanced compared to the stationary CHF in the high pressure (24 bar) as shown in Fig. 3.12. CHF ratios in high pressure region increase as rolling amplitude increases.

3.2.5 Effect of Mass Flux on CHF

The experimental ranges of mass flux vary from 285 to 1300 kg/m^{2}s at 13, 16 and 24 bar of pressure. At the intermediate pressure (13 and 16 bar), the trend of the CHF ratio changes according to mass flux was observed as shown in Figs. 3.13-3.15. The CHF under rolling condition above certain mass flux (500-700 kg/m^{2}s) seems similar to that in stationary or slightly higher. However, when the mass flux is smaller than certain value it gradually decreases as mass flux decreases.

The CHF ratio in higher pressure region (24 bar) is not strongly dependent on the mass flux than intermediate pressure region, as shown in Fig. 3.15. The effect of pressure on CHF ratio in higher mass flux region, is not significant than in lower mass flux region. The CHF ratio is decreasing as the inlet subcooling increases in the low mass flux region. In other words, the CHF ratio is affected significantly by the inlet subcooling in low mass flux region.

3.2.6 Variation of the Inlet Flow Rate

The observed amplitude of the flow oscillation is shown in Fig. 3.16 as the rolling amplitude vs. mass flux. Over the range investigated, the amplitude of the flow oscillation is proportional to the rolling amplitude. As expected, the amount of flow oscillation strongly depends on the inlet subcooling, it decreases with increasing inlet subcooling. A little variation of the flow rate was observed in the cases where the inlet subcooling is high. The fluctuations of the inlet flow were inherent in flow and were observed in the stationary case.

3.2.7 Determination of the Flow Regime

Experimental results show variations of CHF ratios with respect to pressure, mass flux, inlet subcooling, and rolling amplitude. General trend of the CHF mechanism as flow pattern is adopted to understand the variation of CHF ratio under the rolling condition.

To do this, the idea by Hong was applied to identify the annular flow region in this experiment. Hong (2000) calculated the quality and void fraction using vapor superficial velocity suggested by Taitel et al. (1980). It could improve the accuracy of dryout prediction and extend the applicable range to low quality. Whalley (1985) assumed the quality to be 1% at the onset of annular flow (OAF) location to calculate the initial film thickness at the beginning of the annular flow. Levy (1981) suggests the void fraction of 80% at the OAF location and Katto (1984) reduced it by 60%. It is obvious that the void fraction or quality at the OAF varies according to the thermal-hydraulic conditions through the flow pattern map. The vapor superficial velocity is obtained by the churn-to-annular flow transition criterion proposed by Taitel et al. (2009).

Eq.3.5 shows that the transition to the annular pattern is independent of liquid flow rate and pipe diameter.

$$j_g = 3.1\left[\frac{\sigma g\left(\rho_f - \rho_g\right)}{\rho_g^2}\right]^{1/4} \tag{3.5}$$

$$x_{an} = \frac{j_g \rho_g}{G} \tag{3.6}$$

$$\alpha_{an} = \frac{x_{an}}{C_0\left[x_{an} + \frac{\rho_g}{\rho_f}\left(1 - x_{an}\right)\right] + \rho_g \frac{V_{gj}}{G}} \tag{3.7}$$

C_0 is the vapor distribution coefficient and was expressed by Dix (1971) as

$$C_0 = \beta\left[1 + \left(\frac{1}{\beta} - 1\right)^m\right] \tag{3.8}$$

where

$$\beta = \frac{1}{1 + \frac{1 - x_{an}}{x_{an}} \cdot \frac{\rho_g}{\rho_f}} \tag{3.9}$$

$$m = \left(\frac{\rho_g}{\rho_f}\right)^{0.1} \tag{3.10}$$

V_{gj} is the drift velocity which is a void fraction weighted average difference between phase velocities.

$$V_{gj} = 2.9\left[\frac{\sigma g\left(\rho_f - \rho_g\right)}{\rho_f^2}\right]^{1/4} \tag{3.11}$$

The values of void fraction at the OAF, which were calculated from Eqs. 3.5-3.11, are plotted against mass flux in Figs. 3.17 and 3.18. The figure indicates that reduction of CHF is dependent on the behavior of liquid film in annular flow under rolling motion in the low mass flux region. However, transition region cannot be defined clearly. Low mass flux region is considered as annular flow and the rest of the region as bubbly flow.

3.2.8 CHF Mechanism under Rolling Condition

As mentioned above, the bubbly flow (BF) region is defined expect for the annular flow (AF) region. The interval between AF and BF region is hard to decide with void fraction because of change the characteristics of CHF at intermediate pressure. At intermediate pressure, say at 13 and 16 bar, the CHF can be occurred in annular flow for lower mass flux (for example, from 100 to 600 kg/m^{2}s) as depicted in Fig. 3.17.

This phenomenon can possibly be explained by two hypothetical CHF mechanisms. If the dryout occurs because of the annular pattern, variation of inlet mass flow due to rolling motion generates relative minimum flow rate compared with average mass flow rate. This would contribute to the disruption of the liquid layer due to surface wave instability by inlet flow fluctuation. After the disruption of the liquid layer, CHF occurs in the minimum film thickness region corresponding to the minimum flow rate. The second possible hypothetical mechanism is that rolling motion could have noticeably enhanced the droplet entrainment rate in the liquid film to the vapor core. Due to the reduced film thickness caused by the enhanced droplet entrainment rate, CHF is likely to occur earlier in the rolling condition than in the stationary condition. In order to support the second mechanism described in above, additional data was collected for lower mass fluxes at pressure of 13 and 16 bar as shown in Fig. 3.19. As you can see in Fig. 3.19 the CHF ratio decreases with the mass flux decreases. However, its reduction rate relatively decreases below a certain mass flux, which indicates that a limiting entrainment rate exists. In high pressure region (24 bar) and intermediate pressure region at high mass fluxes (for example, 13 bar and above 600 kg/m^2s), the DNB occurs in bubbly flow. These phenomena can be explained by one possible mechanism. Possible explanation is that high mass flux and the force caused by rolling motion drag the bubble away from the boiling surface and thickening the liquid film that delays CHF occurrence.

3.3 Development of the CHF Correlations under Rolling Motion

There is no existing correlation that can be applied to the present experimental condition, i.e., using a Freon R-134a working fluid in a uniformly-heated tube under rolling condition. To develop the correlation, CHF characteristics as referred in 2.3.1 are adopted.

Several previous CHF correlations from Tables 2.2 and 2.3 are relevant to the development of the correlation of this study. To improve quantitative understanding of the rolling motion on CHF, correlations are derived in this section based on the flow conditions measured in the test section inlet (i.e. single-phase region). Correlations are developed to cover the whole regime from LFD to DNB separately, because the phenomenon and mechanisms between them are quite different as explained in section 2.3.1.

3.3.1 Determination of Annular Flow Regime

Flow regimes in the stationary state play an important role in developing the CHF ratio correlation under rolling condition. Therefore, flow regime has to be classified for each experimental condition since they become the reference. The prediction of the flow regime has been the subject of a great deal of work, but no method is available for rolling condition yet. To do this, several void-quality relationships is introduced and compared to decide the determination method. General methods ((Zuber, 1965), (Ahmad, 1970) and (Cioncolini, 2012) and Hong's approach (2000) are used here to predict the void fraction and flow regime.

The general void fractions for subcooled boiling, α proposed by Zuber and Findlay (1965), Ahmad (1970) and Cioncolini (2012) can be obtained by assuming the relationship between α and x_{tr}.

$$\alpha = \frac{x_{tr}}{\rho_g}\left\{1.13\left[\frac{x_{tr}}{\rho_g}+\frac{1-x_{tr}}{\rho_l}\right]+\frac{1.18}{G_{avg}}\left[\frac{\sigma g\left(\rho_l-\rho_g\right)}{\rho_l^2}\right]^{0.25}\right\}^{-1.0} \quad : \text{Zuber} \qquad (3.12)$$

$$\alpha = \frac{x_{tr}}{x_{tr}+S\left(\frac{\rho_g}{\rho_l}\right)\left(1-x_{tr}\right)} \quad : \text{Ahmad} \qquad (3.13)$$

$$\alpha = \frac{hx^n}{1+\left(h-1\right)x^n} \quad : \text{Cioncolini} \qquad (3.14)$$

where

$$S=\left(\frac{\rho_l}{\rho_g}\right)^{0.205}\left(\frac{G_{avg}D_h}{\mu_l}\right)^{0.016} \quad \text{and}$$

$$h=-2.129+3.129\left(\rho_g\rho_l^{-1}\right)^{-0.2186}\ ;\ \ n=0.3487+0.6513\left(\rho_g\rho_l^{-1}\right)^{0.5150} \tag{3.15}$$

To calculate the local void fraction, one must know the true quality, x_{tr} (Levy, 1981). If x is the local quality calculated from a heat balance and thermal equilibrium, x_{eq} will have a finite value at positions where x is zero and negative.

$$x_{eq}=\frac{1}{h_{lg}}\left(\frac{4qL_h}{D_hG_{avg}}-\Delta h_i\right) \tag{3.16}$$

It seems x_{eq} is a function of pressure P, mass flux G, inlet liquid thermal condition and the ratio of the heated length to the inner diameter, L_h/D_h. The L_h/D_h is maintained as a constant value in this study.

In fact, x_{tr} at the point of bubble departure is approximately zero since at that location the bubbles are small and still attached to the heated surface. The corresponding value of x at the same point is negative and equal to x_d:

$$x_d=\frac{h-h_l}{h_g-h_l} \tag{3.17}$$

A simple relation between x_{tr} and x_d is

$$x_{tr}=x-x_d\exp\left(\frac{x}{x_d}-1\right) \tag{3.18}$$

All the models were tested and found no big difference exists in the prediction results. From the above results, prediction of quality is important to calculate the void fraction. Also, in order to predict the local quality, point of bubble departure in the test section should be known. In this study, it cannot check on accurate point of bubble departure in the test section. Hence, other methods for calculating void fraction have been found.

Hong's method (2000) for predicting the void fraction at onset of annular flow (OAF) is adopted because it was difficult to obtain the appropriate quality along the z-direction of heated tube with existing method. In order to define the flow regime with applying the MARMS results, phenomenological prediction of dryout is chosen for deciding the annular flow in each condition. This is due to the fact that it is one of the successful prediction methods of the CHF in flow boiling. Quality and void fraction at OAF should be given to determine the flow pattern.

The values of void fraction and quality at OAF calculated from Eqs. 3.12-3.15 are plotted against mass flux in Figs. 3.17 and 3.18.

3.3.2 Determination of Non-dimensional Numbers

The flow regime at the test section must first be classified, which is representative for the flow conditions. In order to correlate the present CHF data, it is important to identify an appropriate flow regime. If the flow regime can be known at stationary condition, CHF mechanism under rolling condition can be predicted by suggested mechanism based on literature reviews. Void fraction at OAF can be a criterion to divide the flow regime. According to the void fraction at OAF, flow regime can be divided into two regions. LFD region is the regime in which the void fraction greater than 0.8, others region can be defined as DNB region as shown in Fig.3.17.

In order to develop a correlation, non-dimensional form of existing CHF Ratio (C.R) correlation have been adopted. Seven variables can be considered as the CHF experimental parameters under rolling condition. They include channel diameter, D_h, heated length, L_h, mass flux, G, pressure, p, inlet subcooling, h_i, rolling amplitude, θ_R and rolling period, τ. Generally, a CHF Ratio can be correlated based on either inlet dependent variables such as inlet enthalpy and heated length, or local conditions correlation such as outlet quality. Although the correlation based on the local condition is more useful since they represent separate effect, such as axial flux distribution, consideration of heated length effect and spacer grids in a coolant channel in a nuclear reactor, this study has developed a correlation based on inlet condition because of the reasons that the CHF ratios are from experiment in which the uniform heat flux and similar with respect to heated length of marine reactor (Ishida, 1992, 2000) and complexity and lack of experimental support of CHF mechanism.

$$C.R. = f\left(D_h, L_h, G, p, h_i, \theta_R, \tau\right) \tag{3.19}$$

where $C.R. = q_R'' / q_S''$ are CHFs with and without rolling motion, respectively.

Through combining physical properties with CHF experimental parameters, CHF ratio correlation can be expressed in non-dimensional forms as follow:

$$C.R. = f\left(\frac{\rho_l}{\rho_g}, Fr_R, We, \frac{\mathrm{Re}}{\mathrm{Re}_R}, \frac{\tau}{T_{tr}}, \frac{\Delta h_i}{h_{lg}}\right) \tag{3.20}$$

As shown in the above equation, the CHF Ratio is expressed as a function of (1) the ratio of liquid to gas densities, (2) Froud number (Fr_R) for rolling motion, (3) Weber number (We), (4) the ratio of Reynolds (Re) to Reynolds numbers for rolling motion (Re_R), (5) the ratio of rolling period to transient time, and (6) the ratio of enthalpy to the latent heat. These can consider effects of pressure, rolling amplitude, mass flux, bubbles agitation in liquid sublayer, inlet flow oscillation on rolling period and inlet subcooling, respectively. Here T_{tr} is the transit time of the inlet flow through the test section under rolling motion, defined as $T_{tr} = L_h / \left(G_{avg} / \rho_{fi} \right)$.

Angular velocity requires additional calculation before insertion into Re_R. In order to quantitatively estimate the influence of the rolling motion on a forced flow, the Reynolds number for rolling motion was introduced by Murata et al. (1990, 2000 and 2002). It denotes a ratio between the inertial forces, caused by the rolling motion, and the viscosity of the fluid, as follows.

$$\mathrm{Re}_R = u_\theta R / \nu \tag{3.21}$$

where u_θ is the velocity scale of the rolling motion and is describe as

$$u_\theta = R\omega = 2\pi R / \tau \tag{3.22}$$

The length scale R, denotes the distance between the central axis of rolling motion and the inlet of test section. Froude number is an important parameter with respect to the ship's drag or resistance. For this reason, Froud number is adopted to utilize the effect of rolling angle and period using the velocity scale, u_θ, in this study. Weber number is useful in determination of thin liquid film and formation of bubbles. Low values of We may be presumed that dryout of an annular liquid film flowing along the tube wall is mainly responsible for the occurrence of CHF in annular regime and therefore the condition corresponding to the complete exhaustion of liquid at the exit of the tube with the uniform heat flux. A τ / T_{tr} is non-dimensional number representing the wave effect of liquid film on CHF by rolling motion.

The non-dimensional numbers in Eq. 3.20 are selected by characteristics of CHF mechanism in each flow regime. To do this, CHF mechanism is postulated that two flow regimes take part in the hypothetical CHF mechanism. Considering the CHF mechanism in LFD region, the CHF is governed by the wave crest of liquid film flow adjacent to the heater wall by the rolling motion. Droplet generated by wave crest has become large enough to influence the reduction of thickness of liquid film. Rolling motion could have noticeably enhanced the droplet entrainment rate in liquid film to vapor core. Due to the reduced film thickness caused by the increased droplet entrainment rate, CHF is likely to occur earlier than in the stationary CHF. This phenomenon can be checked on trend of CHF ratio in the region of the lower mass flux, as shown in Fig. 3.19. The CHF ratio does not decrease no longer at certain mass flux. It can be supported by existence of limiting entrainment rate corresponding to critical liquid film thickness as mentioned in other literature (Katto, 1984). Also, surface temperature is rapidly increased when dryout occurs in minimum liquid film thickness by wave of liquid film and evaporation. In DNB region, however, CHF is governed by generated bubbles on the heater wall. High mass flux and the force caused by rolling motion drag the bubble away from the boiling surface, thickening the liquid sublayer that delays CHF occurrence.

Correlations for CHF ratio in the current experimental conditions were developed as follows. In order to apply the above CHF mechanisms under rolling motion, the following non-dimensional numbers among those in Eq. 3.20 are chosen for each flow regime.

$$C.R_{LFD} = f\left(\frac{\rho_l}{\rho_g}, Fr_R, We, \frac{\tau}{T_{tr}}, \frac{\Delta h_i}{h_{lg}}\right) \tag{3.23}$$

$$C.R_{DNB} = f\left(\frac{\rho_l}{\rho_g}, \frac{\mathrm{Re}}{\mathrm{Re}_R}, \frac{\Delta h_i}{h_{lg}}\right) \tag{3.24}$$

3.3.3 Determination of Functional Form

The experimental trends indicated that CHF ratio is influenced by pressure, mass flux, inlet subcooling and rolling motion (combination of centrifugal and tangential forces). The CHF correlation will be constructed in this section which attempts to quantify these effects.

The nature of relationship of CHF ratio with respect to each of the eight variables specified in Eqs. 3.25 and 3.26 was determined by varying one of the variables while keeping the others approximately constant and this process was repeated for all the five and three variables at each CHF ratio.

$$C.R_{LFD} = 1 - \left[\left(\frac{\rho_l}{\rho_g}\right)^a (Fr_R)^b (We)^c \left(\frac{\tau}{T_{tr}}\right)^d \left(\frac{\Delta h_i}{h_{lg}}\right)^e\right] \tag{3.25}$$

$$C.R_{DNB} = 1 + a\left[\left(\frac{\mathrm{Re}}{\mathrm{Re}_R}\right)^b \left(c + d\left(\frac{\rho_l}{\rho_g}\right)\right)\left(1 - f\left(\frac{\Delta h_i}{h_{lg}}\right)^g\right)\right] \tag{3.26}$$

This approach helped to determine a basic functional form for relationship as described by non-dimensional numbers. The constants in the correlation are provided in Table 3.5. The CHF ratios are compared with experimental data in Fig. 3.20.

In the transition region (TR), CHF mechanisms under rolling motion cannot be explained exactly. The CHF mechanisms in this region can be supposed as follows;

- Bubble generation can be delayed by increasing the mass flow rate.
- Vapor layer can be produced by bubble crowding or heavy concentration on near heater wall by tangential force.
- Transition of churn-to-annular flow regime can be improved by increasing the coalescence the slugs and bubbles.

Since the mechanisms of CHF for TR cannot be clearly describe, the correlation for the region was proposed by interpolating the LFD and DNB correlations. For the interpolation, the power interpolation was adopted. The functional form of power is logistic function form as void fraction at OAF. The CHF ratios of DNB and LFD regions can be predicted by keeping constant values (0 or 1) using logic function. In transition region, void fractions at OAF corresponding to 0.57 through 0.64 and slope of function have to determine to reduce the error of prediction as shown in Fig. 3.21. The final forms of the CHF ratio correlation is

$$C.R = \left(C.R_{LFD}\right)^{\alpha^*} \left(C.R_{DNB}\right)^{\left(1-\alpha^*\right)} \tag{3.27}$$

$$\alpha^* = \frac{1}{1+e^{-200(\alpha-0.52)}} \tag{3.28}$$

The summary of the final correlation and its respective parameters are given in Table 3.6.

The experimental data (240 points) of MARMS for wide range of system conditions have been chosen for obtaining the correlation. The ranges of the data employed are: $13 < P < 24.5$ [bar], $100 < G < 1300$ [kg/m^{2}s], D= 9.5 [mm], L= 1000 [mm], rolling amplitude=15, 30, 40 [deg.] and rolling period=6 [sec.]. The proposed correlation in the form of Eq. 3.27 with Eqs. 3.25 and 3.26 is assessed using MARMS data and the results are summarized in Table 3.7 and Fig. 3.22. Within ranges of the given data, the mean error, mean absolute error and the root-mean square (RMS) error are shown in Table 3.7.

3.4 Comparison with Heaving Correlations

Various researches have proposed CHF correlations under heaving condition. Chang et al. (1997), Isshiki (1965) and Otsuji et al (1982) suggested the CHF correlations that include the gravity acceleration effect as mentioned Chapter 2. In order to compare the CHF correlation under rolling motion, accelerations under rolling motion should be transform into a comparable form with acceleration under heaving motion. The tangential acceleration is proportional to the amplitude, while the centrifugal acceleration to the square of the rolling amplitude. The tangential acceleration is larger than the centrifugal acceleration at any location of the test section and is considered to have predominant influences on the thermal-hydraulic behavior of the test section. The tangential acceleration due to the rolling motion and its magnitude are described as follows:

$$a_\theta = -r\ddot{\theta} = -r\left(\frac{2\pi}{\tau}\right)^2 \omega^2 \Theta \sin\left(\frac{2\pi}{\tau}\cdot t\right) \text{ and } |a_\theta| = -r\left(\frac{2\pi}{\tau}\right)^2 \Theta \qquad (3.29)$$

where r, τ and Θ represent the distance from the rolling axis, rolling period and rolling amplitude, respectively.

As for the present experiment, the magnitude of tangential acceleration reaches its maximum, when r =1.5 m, τ =6 s and Θ= 15, 30 and 45 [deg.] = 0.26, 0.52 and 0.70 [rad.]. The maximum magnitude is estimated to be 5, 9 and 12 percents of gravitational acceleration (0.05g, 0.09g and 0.12g), respectively. Figure 3.23 shows the CHF ratio under rolling motion compared with the CHF ratio under heaving motion as relative gravity acceleration. This figure indicates that rolling motion can affect bubble motion and liquid film behavior more complexly by combination of tangential and centrifugal forces and mass flow than heaving motion.

Table 3.1 Design specification of MARMS

A. Rolling System	
• Load	>500 kg
• Max. Rolling Amplitude	45 deg.
• Max. Rolling period	36 sec.
B. Circulation Loop	
• Working Fluid	Freon R-134a
• Max. Operating Pressure	4.0 MPa
• Max. Operating Temperature	150 ^{o}C
• Max. Flow Rate	2 kg/sec
C. Equipment	
• Power Supply	DC 48kW
• Cooler	21 kW Brazed Type
• Pressurizer	70 bar Accumulator type
• Pump	Head: 30 m Non-seal canned motor

Table 3.2 Test matrix conditions in R-134a and water-equivalent conditions

$P_{R\text{-}134a}$ [bar]	**P_{Water} [bar]**	**$G_{R\text{-}134a}$ [kg/m^{2}s]**				
		285	**500**	**712**	**1000**	**1300**
		G_{Water} [kg/m^{2}s]				
13	80	402	705	1005	1411	1834
16	100	400	702	1000	1405	1826
24	140	396	696	990	1391	1808

Table 3.3 A summary of R-134a-water fluid-to-fluid modeling scaling factor

Summary of scaling factor (F_L, F_P, F_H, F_G, F_q) along with pressure					
R-134a, Pressure [bar]	F_L	F_P	F_H	F_G	F_q
13	1	5.8	9.46	1.39	13.2
16	1	5.6	9.42	1.38	13.0
24	1	5.0	9.33	1.34	12.4

Table 3.4 Test matrix under rolling condition

Loop condition				**Rolling amplitude [deg.]**		**Rolling period [s]**
Pressure [bar]	**Mass flux [kg/m^{2}s]**	**Subcooling [kJ/kg]**	+		+	
				15		6
13-24	285-1300	3-63		30		8
				40		12

Table 3.5 Values of the constant in proposed correlations

	LFD	DNB
a	0.437	134.26
b	1.059	0.0180
c	0.107	0.0430
d	0.166	-0.042
e	-0.139	0.009
f	-	-0.448
g	-	2.010
h	-	-0.475

Table 3.6 Model for prediction of void fraction

CHF ratio correlation	
$C.R = \left(C.R_{LFD}\right)^{\alpha^*}\left(C.R_{DNB}\right)^{\left(1-\alpha^*\right)}$	Eq.(20)
Supporting equations	
$C.R = \frac{q_R^{"}}{q_S^{"}}$,	Eq.(18)
$C.R_{LFD} = 1-\left(\frac{\rho_f}{\rho_g}\right)^{0.43}\left(\mathrm{Fr_R}\right)^{1.05}\left(\mathrm{We}\right)^{0.10}\left(\frac{\tau}{T_{tr}}\right)^{0.16}\left(\frac{\Delta h_i}{h_g}\right)^{-0.13}$ $C.R_{DNB} = 1+134.26\left(\frac{\mathrm{Re}}{\mathrm{Re}_R}\right)^{0.01}\left[0.04-0.04\left(\frac{\rho_l}{\rho_g}\right)^{0.009}\right]\left[-0.44-2.01\left(\frac{\Delta h_i}{h_{lg}}\right)^{-0.47}\right]$	Eq.(19)
$\mathrm{Re} = \frac{G_{avg} D_h}{\mu_l}$, $\mathrm{Re}_R = \frac{u_\theta R}{\nu}$, $We = \frac{G_{avg}{}^2 D_h}{\rho_l \sigma}$	Eq. (16)
$u_\theta = \frac{2\pi R}{\tau}$, $T_{tr} = \frac{L_h}{\left(G_{avg}/\rho_l\right)}$	Eq. (17)

Table 3.7 Performance of CHF Ration correlation in the present study

Region	**Number of data**	**Prediction**		
		Mean error* [%]	**Mean absolute error** [%]**	**RMS error*** [%]**
LFD	84	0.43	1.584	2.033
DNB	93	0.083	1.703	2.124
Transition region	63	-2.305	2.829	3.374

* mean error $= \frac{1}{N}\sum \frac{C.R_{pred} - C.R_{\exp}}{C.R_{\exp}} \times 100\%$,

** mean absolute error $= \frac{1}{N}\sum \frac{\left|C.R_{pred} - C.R_{\exp}\right|}{C.R_{\exp}} \times 100\%$ and

*** RMS error $= \sqrt{\frac{1}{N}\sum \left(\frac{C.R_{pred} - C.R_{\exp}}{C.R_{\exp}}\right)^2} \times 100\%$

where, N is the number of CHF Ratio data.

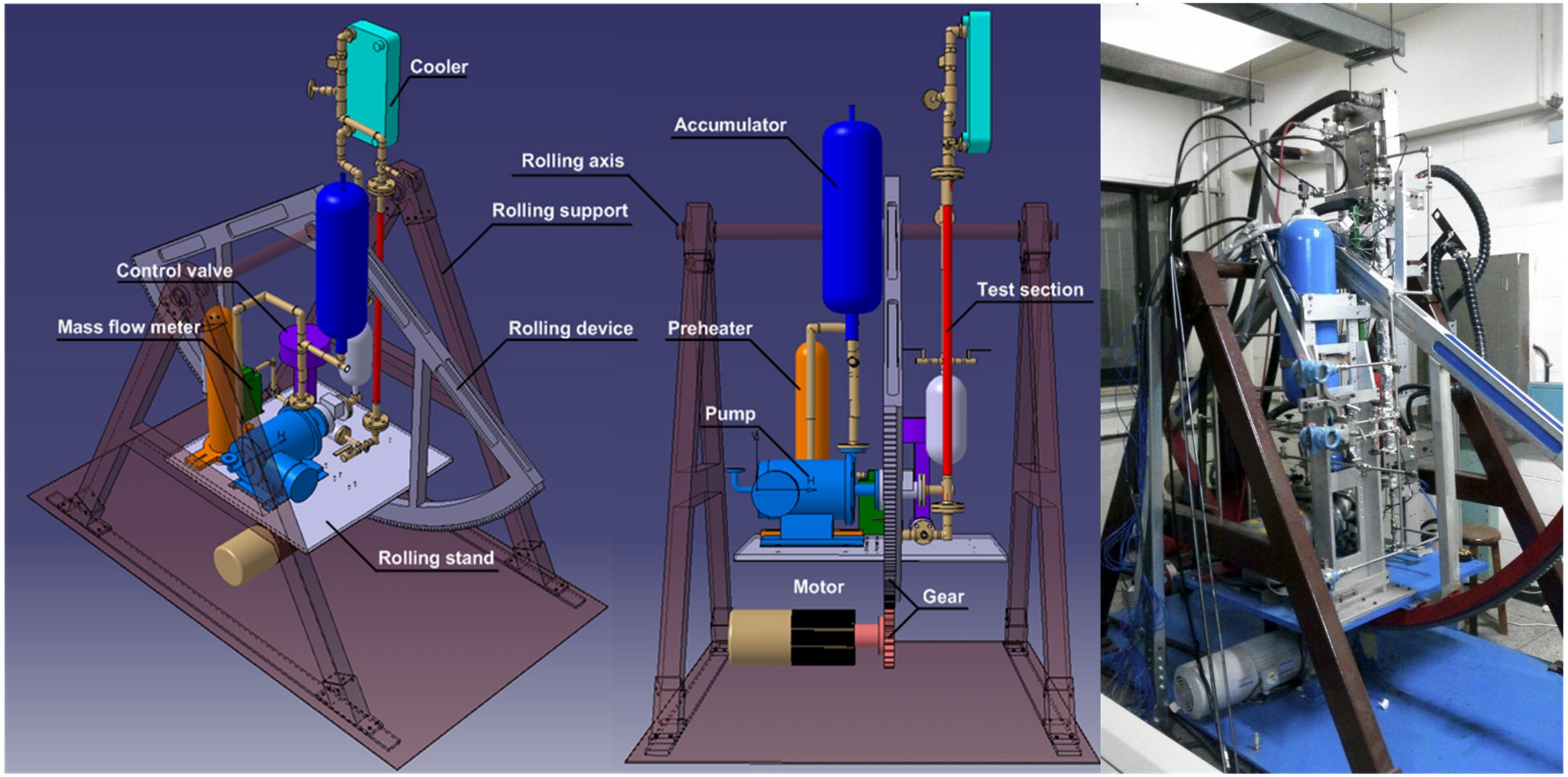

Figure 3.1 Isometric and lateral view of MARMS

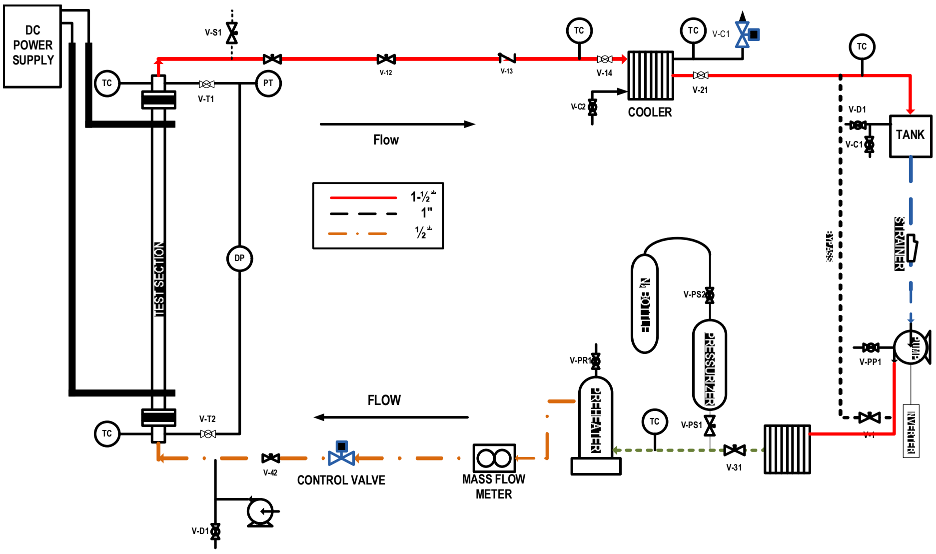

(a) P&ID diagram of CHF loop

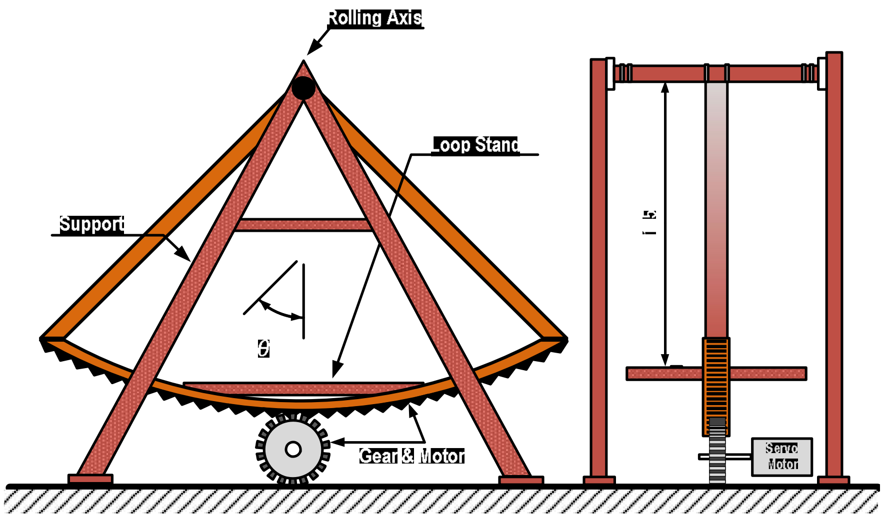

(b) A front and side view of rolling system

Figure 3.2 Schematic diagram of MARMS

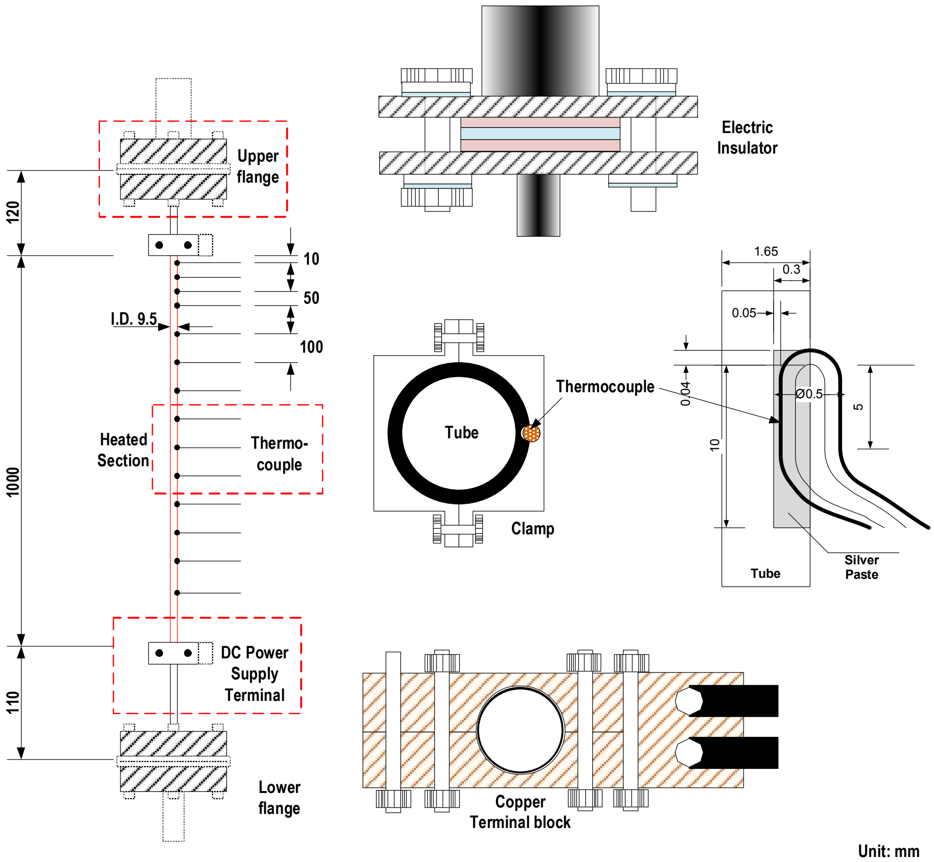

Figure 3.3 Schematic diagram of test section in Freon circulation loop

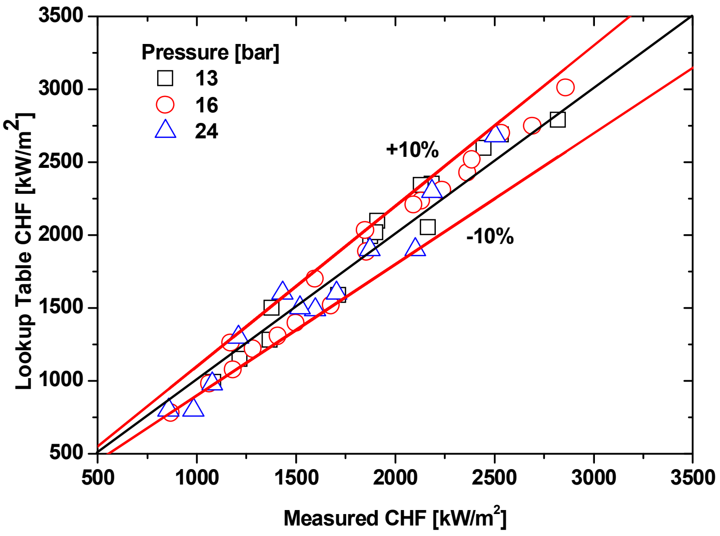

Figure 3.4 Comparison between water-equivalent CHF value and 2006 CHF look-up table

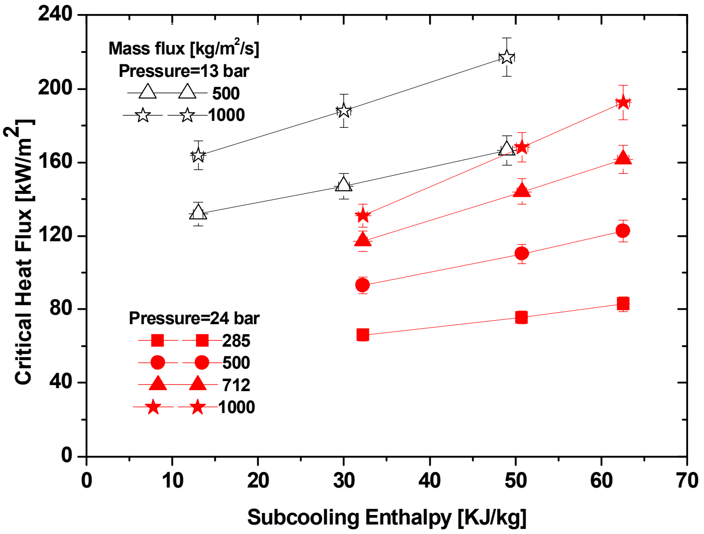

Figure 3.5 Effect of inlet subcooling enthalpy (pressure: 13 and 24 bar)

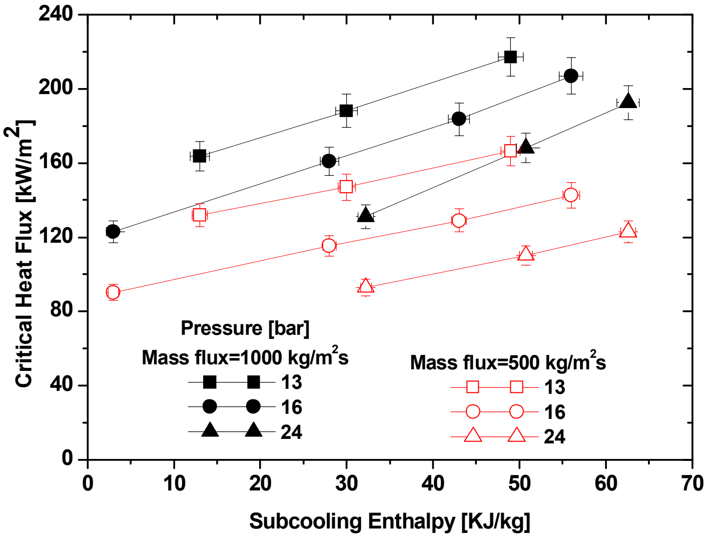

Figure 3.6 Effect of pressure (mass flux: 500 and 1000 kg/m^2s)

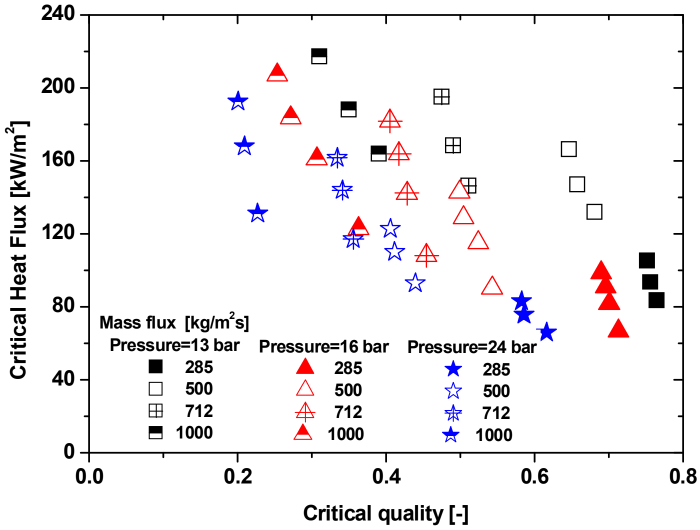

Figure 3.7 Effect of critical quality

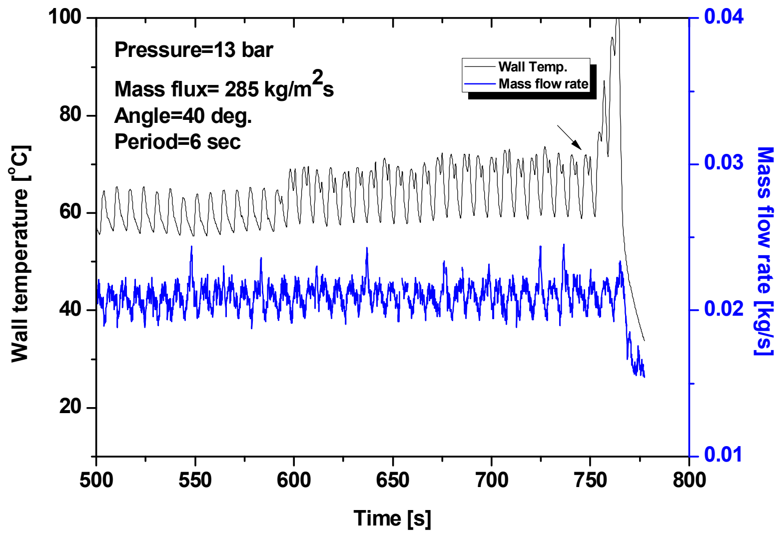

Figure 3.8 Behaviors of wall temperature and mass flow rate under rolling condition (Pressure: 13 bar, mass flux: 285 kg/m^{2}s)

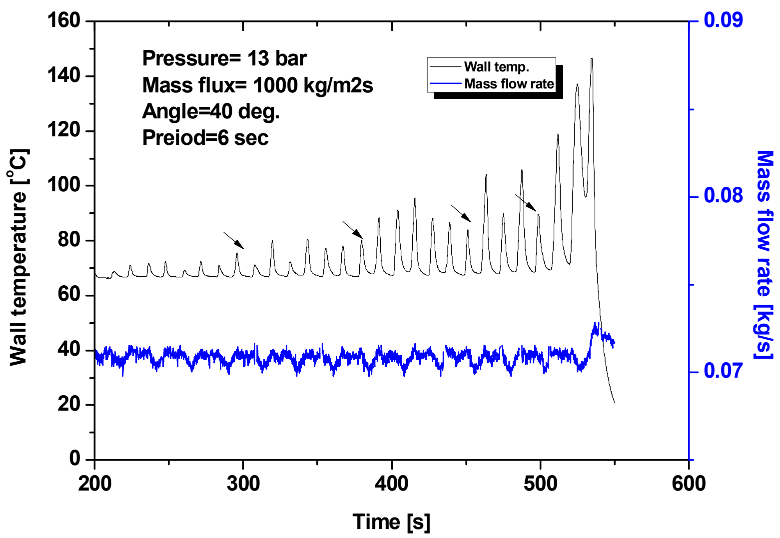

Figure 3.9 Behaviors of wall temperature and mass flow rate under rolling condition (Pressure: 13 bar, mass flux: 1000 kg/m^{2}s)

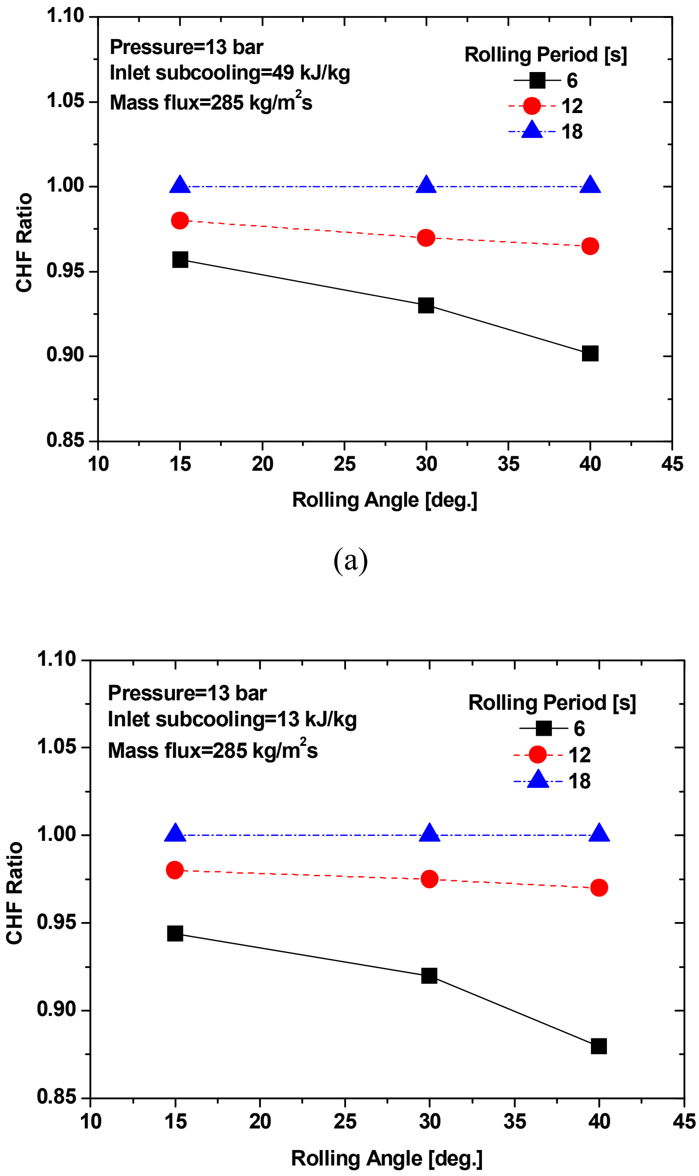

(a)

(b)

Figure 3.10 Effect of rolling period on CHF ratio as inlet subcooling. Outlet pressure: 13 bar

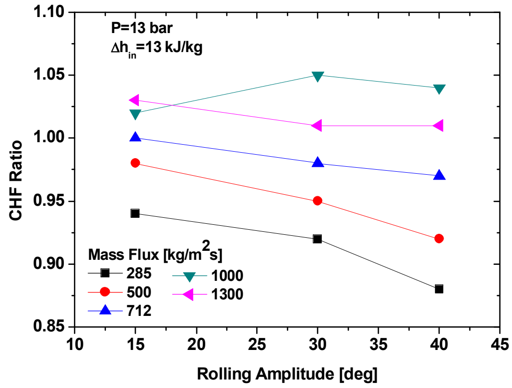

(a)

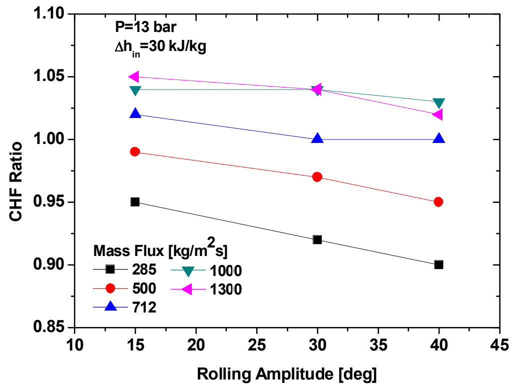

(b)

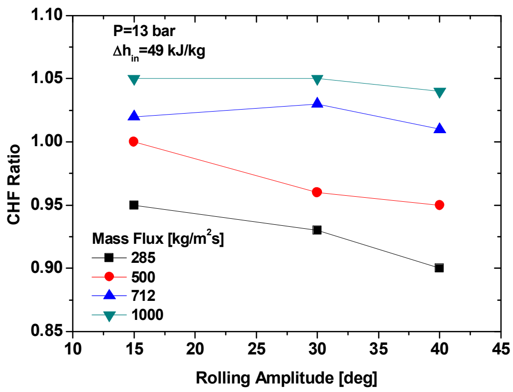

(c)

Figure 3.11 Effect of rolling amplitude on CHF ratio as inlet subcooling and mass flux. (Outlet pressure: 13 bar, rolling period: 6 seconds)

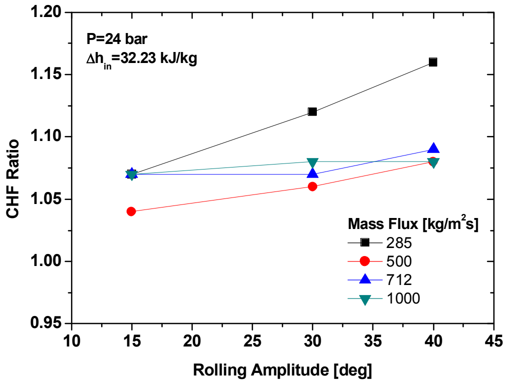

(a)

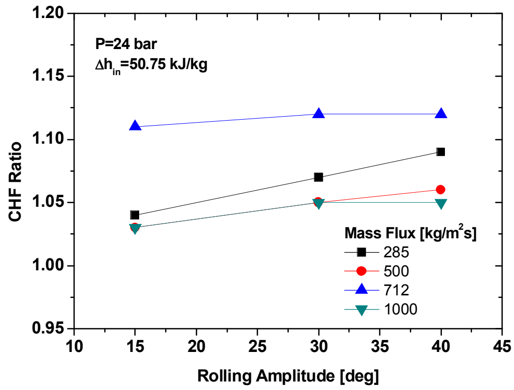

(b)

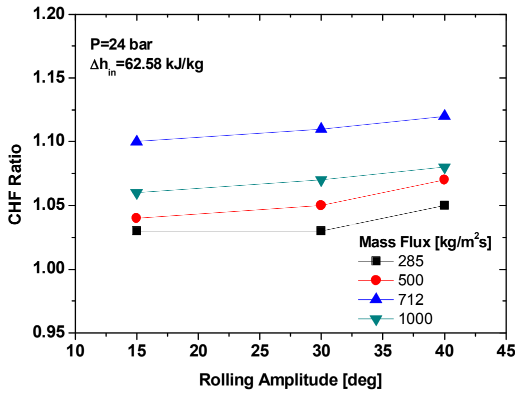

(c)

Figure 3.12 Effect of rolling amplitude on CHF ratio as inlet subcooling and mass flux. (Outlet pressure: 13 bar, rolling period: 6 seconds)

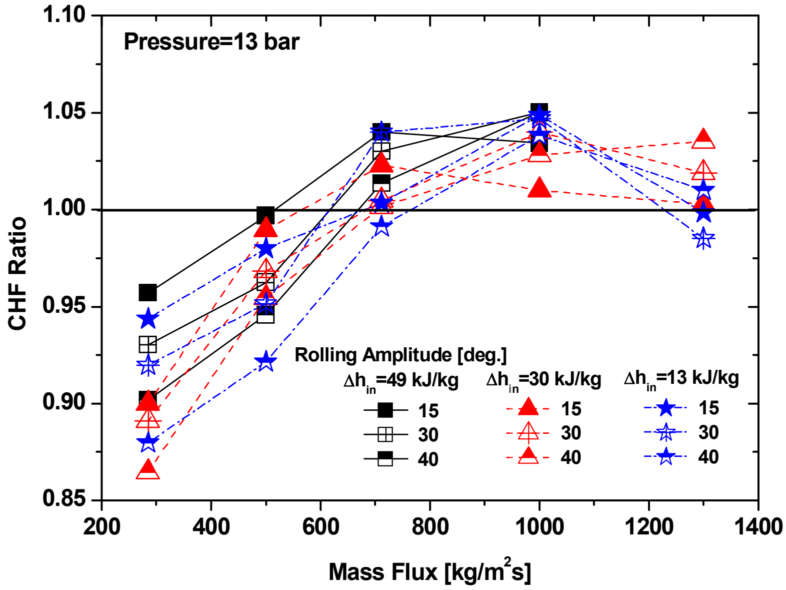

Figure 3.13 Effects of mass flux on CHF ratio as inlet subcooling and rolling amplitude. (Pressure: 13 bar, Rolling period: 6 seconds)

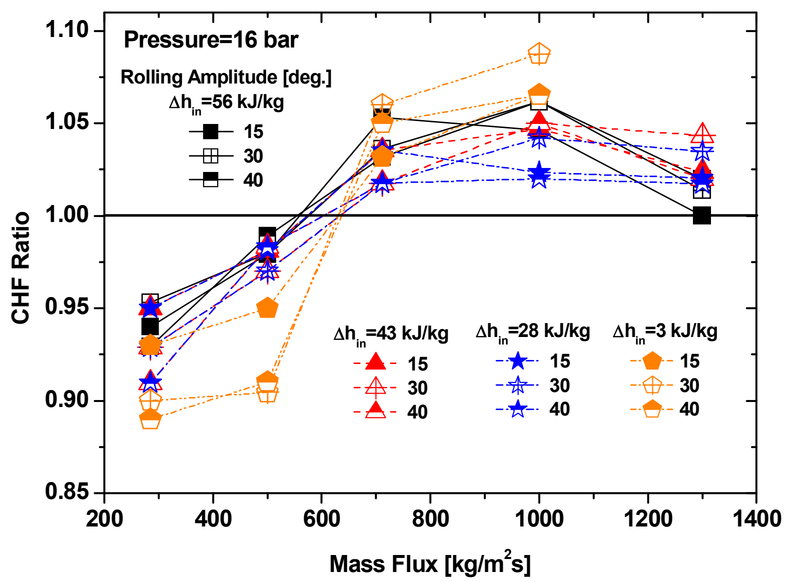

Figure 3.14 Effects of mass flux on CHF ratio as inlet subcooling and rolling amplitude. (Pressure: 16 bar, Rolling period: 6 seconds)

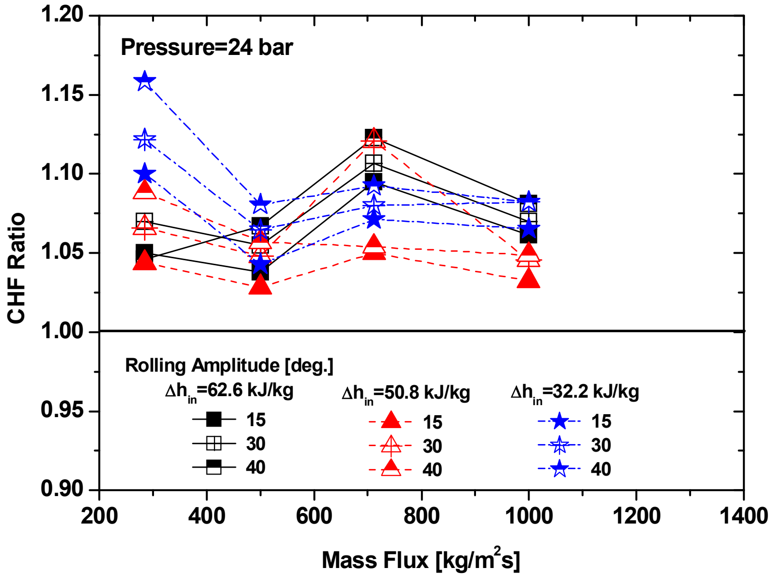

Figure 3.15 Effects of mass flux on CHF ratio as inlet subcooling and rolling amplitude. (Pressure: 24 bar, Rolling period: 6 seconds)

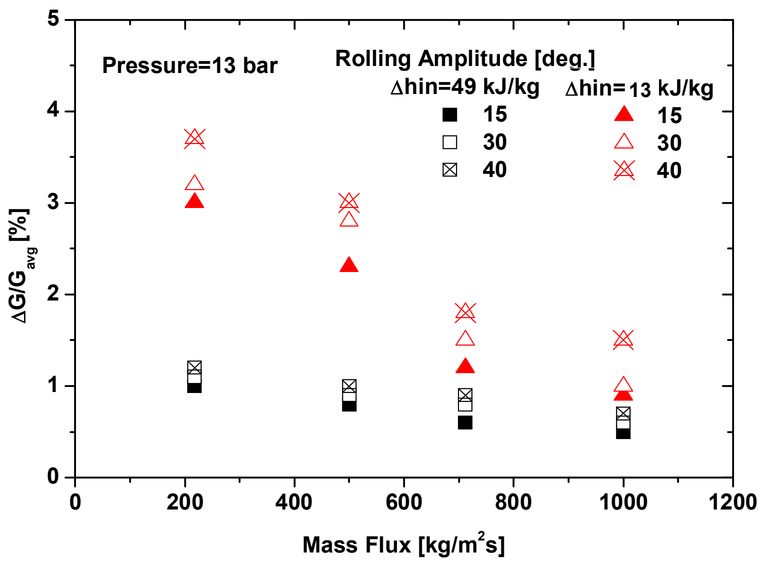

Figure 3.16 Amplitude of flow oscillation under rolling condition at 13 bar.

(Rolling period: 6 seconds)

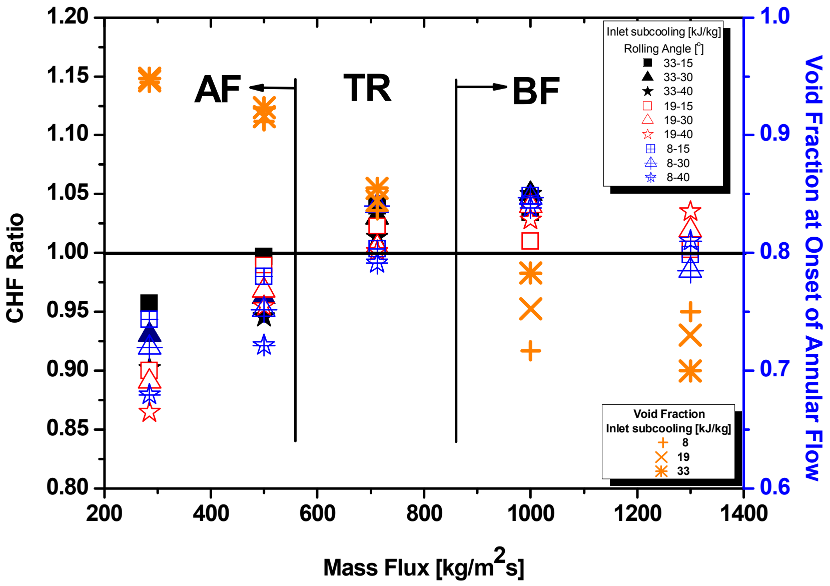

Figure 3.17 Void fraction response to mass flux with inlet subcooling (Pressure: 13 bar)

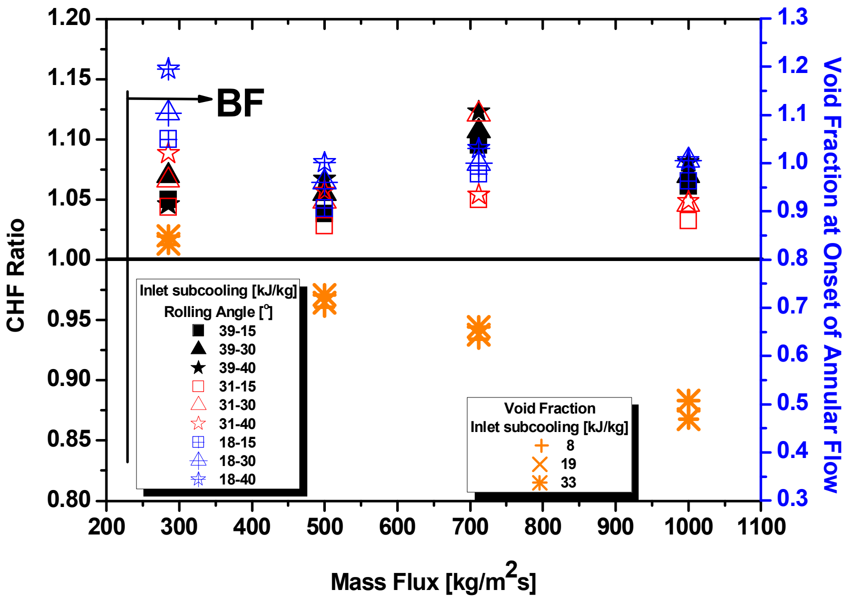

Figure 3.18 Void fraction response to mass flux with inlet subcooling (Pressure: 24 bar)

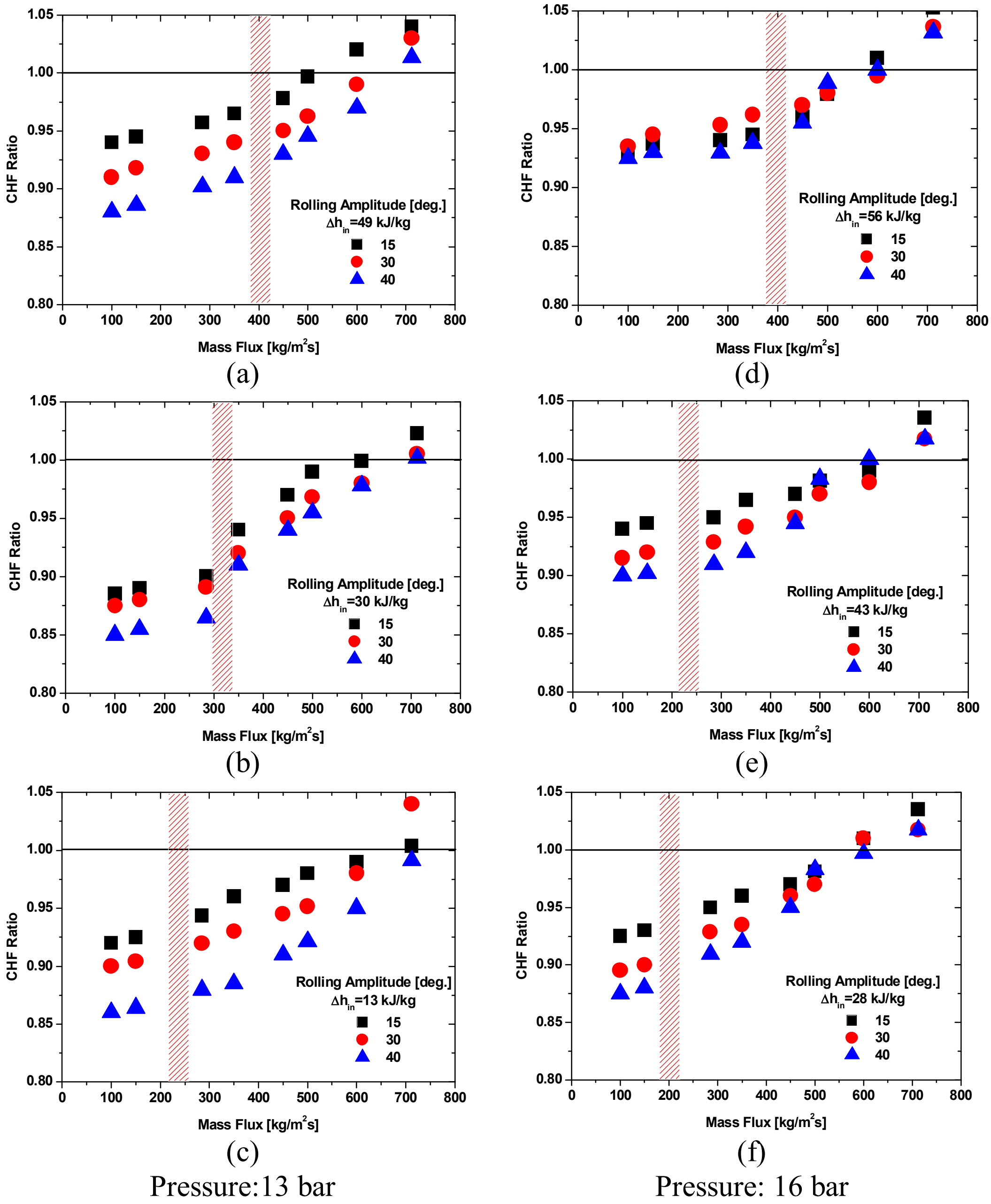

Figure 3.19 Trends of CHF ratio in lower mass flux (Rolling period: 6 seconds)

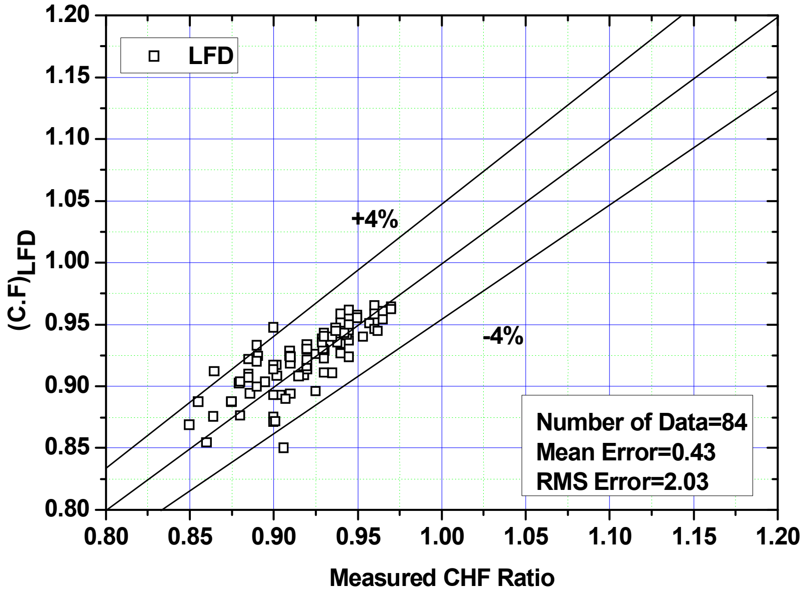

(a) LFD region

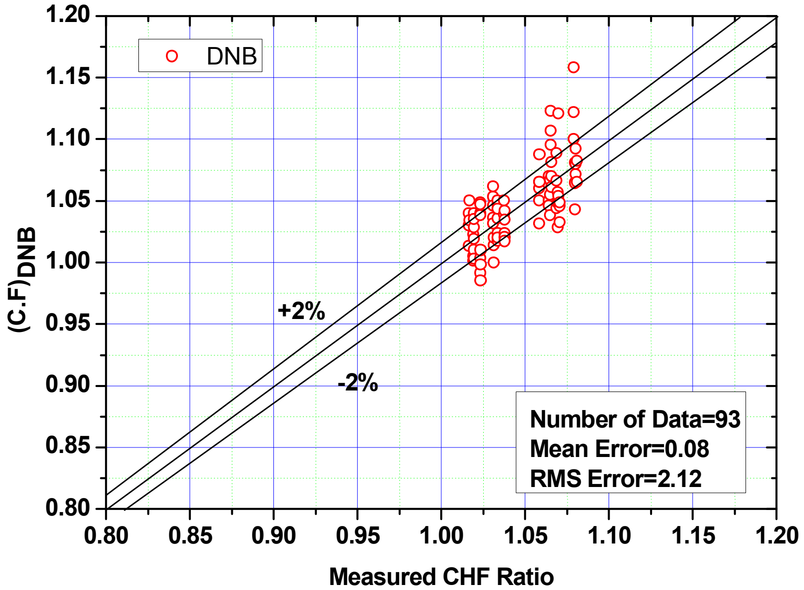

(b) DNB region

Figure 3.20 Comparison of CHF ratio correlations at each region

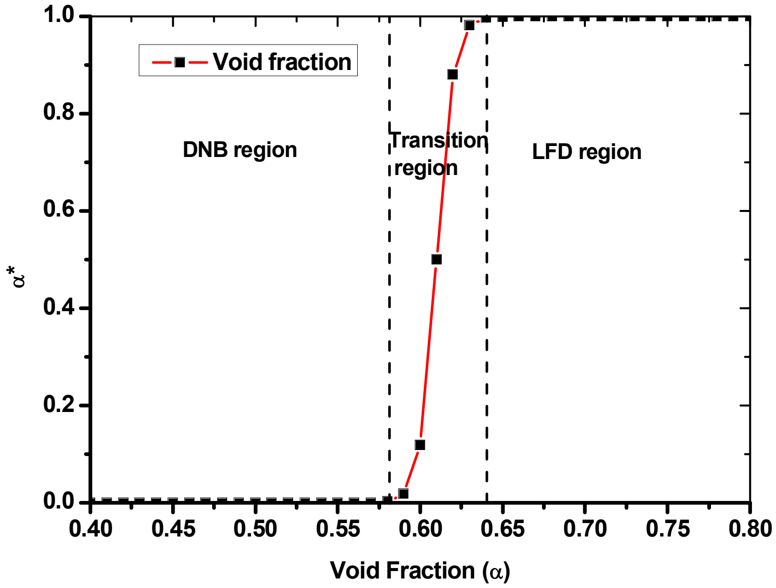

Figure 3.21 Logistic function of void fraction

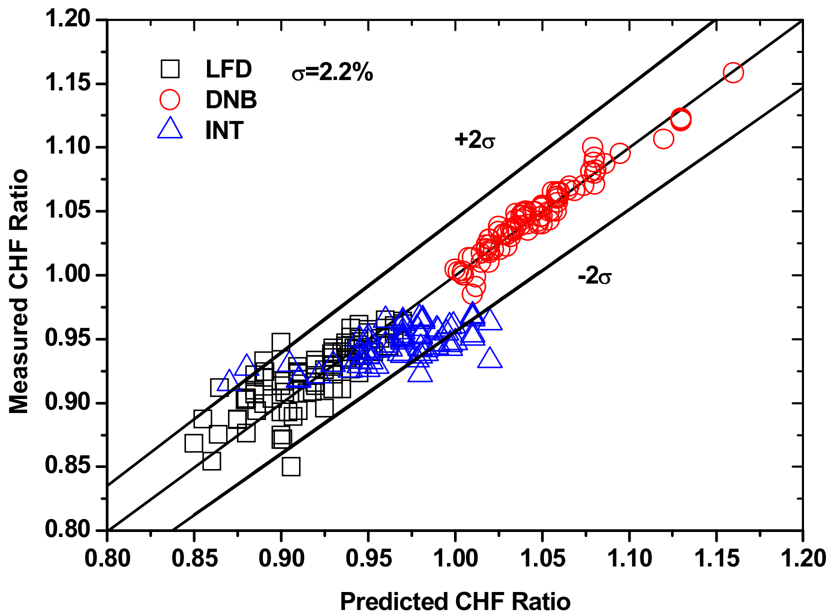

Figure 3.22 Evaluation of CHF ratio correlation with all data

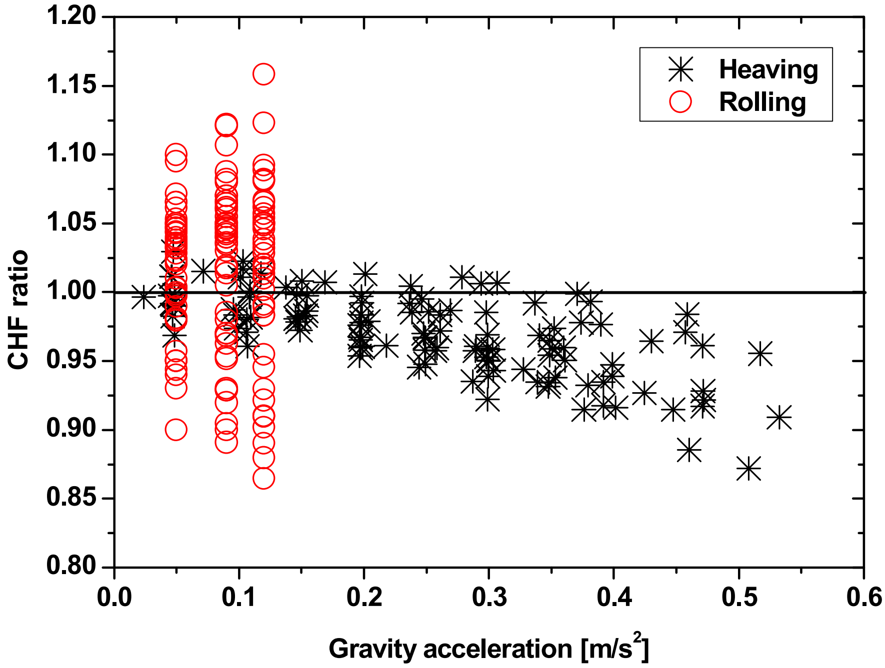

Figure 3.23 Comparison of rolling and heaving CHF ratios

Chapter 4
Computational Study on Thermal-Hydraulics in Marine Reactors

4.1 Introduction

In this study, the heaving and rolling models in TAPINS-M, which is the modified version of TAPINS (Lee, 2012), are added to assess the applicability of the TAPINS-M for thermal-hydraulic simulations of a marine reactor under rolling motions. Thermal-hydraulic characteristics of marine reactor such as N.S. Mutsu (Ishida, 1992) and MRX (Ishida, 2000) can be influenced by various ship motions as shown in Fig. 1.2. Among them, rolling and heaving are dominant in the marine reactors as shown in Fig. 4.1 and very important for the design and operation of marine nuclear reactors.

Since ship motions affect the momentum transfer during natural circulation and forced convection, the modification of the momentum equation was mainly implemented to TAPINS-M. For the modeling of heaving motion, which is a linear motion in the z-direction, the gravity acceleration should be treated as a function of time. For the modeling of rolling motion, which is a rotational motion, the tangential and centrifugal forces projected in x- and z-directions should be added in the body force term. Thus, the distance between the center of rotation and the center of each control volume should be given as an input variable for the calculation of the tangential and centrifugal forces. Also, the distance between the center of the control volume and the connecting junctions should be given since the body force term is generated by the multiplication of the acceleration force and the distance between the center of volume and junction in each direction.

4.2 Development of TAPINS-M Code

4.2.1 Introduction of TAPINS Code

The TAPINS code was selected as an analysis tool for simulating the coolant behavior of MARMS. TAPINS (Thermal-hydraulic Analysis Program for Integral reactor System) code as an integrated-system-specific analysis code (Lee, 2012) was developed to confirm the design basis of an integral reactor, such as natural circulation, pool-type reactor pressure vessel and low pressure operating and to investigate the RCS (Reactor Coolant System) response to the non-LOCA transients, such as changing in the core power and reduction in feedwater flow rate on the natural circulation.

4.2.2 Development of TAPINS-M Code

Governing Equation of TAPINS

The formulation of the hydrodynamic model used in the TAPINS is based on the one-dimensional homogeneous equilibrium model (HEM), which consists of the conservation laws for mass, momentum, and energy (Todreas and Kazimi, 1990):

Continuity equation:

$$\frac{\partial \rho}{\partial t}+\frac{\partial G}{\partial z}=0 \tag{4.1}$$

Momentum conservation equation:

$$\frac{\partial G}{\partial t}+\frac{\partial}{\partial z}\left(\frac{G^2}{\rho}\right)=-\frac{\partial P}{\partial z}-\frac{f}{2D_h}\frac{G|G|}{\rho}-\rho g \tag{4.2}$$

Energy conservation equation:

$$\rho\frac{\partial h}{\partial t}+G\frac{\partial h}{\partial z}=\frac{q^{''}P_h}{A} \tag{4.3}$$

Frictional dissipation and the work done by the pressure are neglected in the energy equation. Using the non-conservative form of the energy equation is plausible since the loss of accuracy is expected to be insignificant due to the existence of large sources or sinks of heat in the RCS. It is also more convenient for the treatment of the difference schemes.

A fundamental aspect of the momentum integral model (Meyer, 1961) is that the fluid is considered incompressible but thermally expandable, as follows:

$$\rho = \rho\left(P^*, h\right) \tag{4.4}$$

where P^* is a reference pressure which is assumed to be constant during transients. This means that the variation of fluid properties due to the pressure change is ignored. This assumption is physically acceptable for most operational transients in a nuclear reactor, except for events accompanied by a huge loss or bulk boiling of the coolant. In the TAPINS, instead of coming up with a local pressure distribution, a representative value of the system pressure updated by a steam–gas pressurizer model is imposed as P^*. From the fluid incompressibility, a further convenience is obtained as the volumetric flow rate becomes uniform around the loop, depending only on time.

The principal point of the momentum integral model is the analytical integration of the momentum conservation equation over space. This approach eliminates the pressure gradient term because the sum of the pressure drop around any closed circuit is zero. Furthermore, on account of the normal mode of coolant circulation in integral reactor being natural convection, the Boussinesq approximation is applied to the momentum equation; the density is regarded as constant except for the gravitational term, in which the density varies linearly with temperature (Zvirin, 1981). Therefore, the final form of the integral momentum equation solved in TAPINS is:

$$\rho_0\left(\sum_k \frac{L_k}{A_k}\right)\frac{dQ}{dt} = -\frac{\rho_0}{2}\left(\sum_k f_k \frac{L_k}{D_{h_k} A_k^2} + \sum_k \frac{k_j}{A_j^2}\right)Q^2 + \rho_0 g \beta \sum_k T_k L_k \cos\theta_k \tag{4.5}$$

The fluid properties are to be homogeneous in each node. In the closed circuit, the boundary condition is altered to the requirement that the coolant enthalpy is continuous around the loop. Eqs. 4.3 and 4.5 are applied to the one-dimensional network. The constitutive relations, e.g. the equation-of-state, friction coefficient, heat transfer correlation and so on, complete the definition of the system properties. In TAPINS, the friction factor is calculated by the theoretical relation, $f = 64/Re$, for laminar flow and the Zigrang–Sylvester equation (1985) for turbulent flow. The form loss coefficient for an abrupt area change is either given in the input card by the user or calculated automatically by a simple module of TAPINS which compares the flow area of adjacent nodes and computes the loss coefficients by sudden expansion or sudden contraction using the empirical formula. The thermophysical properties of fluids are calculated by PROPATH 12.1 (PROPATH GROUP, 2001).

Solving just a single integral momentum equation, along with placing less stringent requirements on the time-step, results in great savings in the computational cost. This is the reason for incorporating the above simplified hydrodynamic model formulated from the momentum integral model into the TAPINS, even though there might be some loss of local information.

Code Structure of TAPINS

Code structure of TAPINS is depicted in Fig. 4.2. TAPINS consists of a couple of large blocks divided by the function in the calculation. The subroutine “InpReader” reads all data from the input file and checks for some probable errors. From the stored data, the subroutine “SetSys” prepares the pre-processors required to the computation by defining the fundamental variables for the core and S/G and allocating the geometric data to the dynamic arrays. The temperature distribution of the primary circuit is initialized and the steady-state heat conduction solution is found for the fuel rods and the S/G helical tubes in the subroutine "IniCndtn". The subroutine Hydromod is the main module of TAPINS to facilitate solution of transient problems. It contains the subroutines to advance the solutions for the reactor kinetics, the hydrodynamic model, the helical coil S/G model, the steam-gas pressurizer model, the heat conduction equations, and so on. Various constitutive relations support to solve the hydrodynamic model, including the state relationships, the vapor generation model, the wall friction correlation, etc.

Physical Models for Marine Reactor

In the TAPINS code, the integral momentum equation is given as

$$\rho_0\left(\sum_k \frac{L_k}{A_k}\right)\frac{dQ}{dt} = -\frac{\rho_0}{2}\left(\sum_k f_k \frac{L_k}{D_{h_k} A_k^2} + \sum_k \frac{k_j}{A_j^2}\right)Q^2 + F_B \tag{4.6}$$

For the modeling of the moving motion, the gravity head term (body force term) in the above equation must be modified. Gravity should be treated as a time dependent function and acceleration forces induced by ship motions should be included in the gravity head term.

(A) Heaving modeling

To take into account the time dependent vertical acceleration of gravity force, g_z, in the momentum equation is replaced with time dependent gravity $g(t)$.

$$\rho_0\left(\sum_k \frac{L_k}{A_k}\right)\frac{dQ}{dt} = -\frac{\rho_0}{2}\left(\sum_k f_k \frac{L_k}{D_{h_k} A_k^2} + \sum_k \frac{k_j}{A_j^2}\right)Q^2 + \rho_0 g\beta \sum_k T_k L_k \cos\theta_k \cdot \left[g_z + A\sin\left(\frac{2\pi}{T_s}t\right)\right] \tag{4.7}$$

For simple periodical oscillation, g(t) can be expressed as

$$g(t) = g_z + A\sin\left(\frac{2\pi}{T_s}t\right) \tag{4.8}$$

where

A=amplitude

T_s=oscillation period

(B) Rolling modeling

Rolling is a rotational motion which generates the time dependent centrifugal and tangential accelerations, a_c and a_t, on the system,

$$a_c = \omega\times(\omega\times r) = R_k\dot{\theta}_z \sin\theta_z \hat{x} + R_k\dot{\theta}_z \cos\theta_z \hat{z} \tag{4.9}$$

$$a_t = \beta\times r = R_k\ddot{\theta}_z \cos\theta_z \hat{x} - R_k\ddot{\theta}_z \sin\theta_z \hat{z} \tag{4.10}$$

Each force on the fluid volume under rolling is depicted in Fig. 4.3. For the given rotational angle θ_z around the z-axis as a function of time, the centrifugal and tangential acceleration can be divided into x and z components as follows,

$$a_z = R_k\dot{\theta}_z \sin\theta_z + R_k\ddot{\theta}_z \cos\theta_z \tag{4.11}$$

$$a_z = R_k\ddot{\theta}_z \cos\theta_z - R_k\ddot{\theta}_z \sin\theta_z \tag{4.12}$$

Relative location of the center of volume in Fig. 4.4 can be expressed as follows,

$$CMASX_k = CMAS_k \sin\theta_z \tag{4.13}$$

$$CMASZ_k = CMAS_k \cos\theta_z \tag{4.14}$$

The relative location of the flow junction for volume can be given as

$$RELZX = RELZ \sin\theta_z + 0.5BOT \cos\theta_z \tag{4.15}$$

$$RELZZ = RELZ \cos\theta_z - 0.5BOT \sin\theta_z \tag{4.16}$$

For a given rotational angle, the relative locations between the center of volume and the junction in the z-axis can be calculated as follows for “from volume” i and “to volume” i+1, respectively,

$$\left(z_k - z_i\right)_z = CMASZ_k - RELZZ_i \tag{4.17}$$

$$\left(z_{i+1} - z_k\right)_x = RELZZ_o - CMASZ_k \tag{4.18}$$

Also, the relative locations in the x-axis are

$$\left(z_k - z_i\right)_z = CMASZ_k - RELZZ_i \tag{4.19}$$

$$\left(z_{i+1} - z_k\right)_x = RELZZ_o - CMASZ_k \tag{4.20}$$

Considering the above equations, the body force terms are made up of the gravity head term and acceleration terms in the x- and z-directions by the centrifugal and tangential forces. Therefore, the modified integral momentum equation is given as follows,

$$\begin{aligned}\rho_0\left(\sum_k \frac{L_k}{A_k}\right)\frac{dQ}{dt} &= -\frac{\rho_0}{2}\left(\sum_k f_k \frac{L_k}{D_{h_k} A_k^2} + \sum_k \frac{k_j}{A_j^2}\right)Q^2 - \Delta P_{pump} \\ &\quad -\sum_k \left[\rho_k \left(z_{i+1} - z_i\right)_z\right]\cdot\left(g_z + a_z\right) + \left[\rho_k \left(z_{i+1} - z_i\right)_x\right]\cdot a_x\end{aligned} \tag{4.21}$$

The third term of the right hand side represents the vertical acceleration change by the heaving and rolling motions. The fourth term accounts for the acceleration in the horizontal direction.

4.3 Validation of TAPINS-M Code with MARMS Data

The following four experimental analyses are introduced for code validation: the first is the CHF in natural circulation under rolling motion; the second is single-phase natural circulation under rolling motion; the third is the two-phase flow under rolling motion; and the fourth is the transient condition during rolling motion. The validation matrix is presented in Table 4.1 with a brief description on the assessment objectives of each problem. In the simulations of TAPINS-M, a total of 28 nodes constitute the MARMS loop as shown in Figs. 4.5 and 4.6.

4.3.1 Analysis on CHF under Rolling Motion

The first validation activity that was carried out for a comprehensible assessment of the TAPINS-M code was concerned with the CHF model under rolling motion. As described in Chapter 3, the CHF ratio correlation was developed to predict the CHF under rolling motion. The developed correlation of CHF ratio under rolling motion was implemented into the TAPINS-M code for a proper prediction of onset of CHF under rolling condition. The calculation procedure of wall temperature in the TAPINS-M code is summarized as following; heat transfer mode was determined by using CHF ratio correlation. According to the onset of CHF, modes of pre-CHF and post-CHF were defined. Depending on the CHF modes, heat transfer coefficient was varied. Through the updated heater power, the wall temperature was calculated by heat flux. If the wall heat flux was determined to be lower than the CHF, heat transfer rate of pre-CHF was used.

Then, the wall temperature was calculated by heat transfer rate of pre-CHF. However, if the wall heat flux was equal to or greater than the CHF, heat transfer rate of post-CHF was applied to calculate the wall temperature at post-CHF mode as shown in Fig. 4.7.

To assess the capability of CHF prediction, additional experiment with MARMS was conducted. For the simulation of CHF under natural circulation, the pump is tripped at 55 seconds as shown in Fig. 4.8. The valve was fully closed simultaneously with pump trip so that the flow rate in test section was reduced to zero. As the reduction in the flow rate causes a rapid increase of increasing of the pressure, after that the pressure decreased slightly due to the heat removal by natural circulation. Starting from 150 seconds, the heater wall temperature was increased gradually without heat input to test section. In other words, CHF is occurred at this point. Figure 4.9 displays the wall temperature calculation result at the moment of the CHF occurrence. Since TAPINS-M employed the CHF correlation developed from MARMS data, it can predict the CHF under rolling condition.

4.3.2 Flow Variation under Rolling Motion

Single- and Two-phase natural circulation under rolling motion

Experiments of the single- and two-phase natural circulation under rolling condition were conducted to evaluate the capability of TAPINS-M, as shown in Figs. 4.10 and 4.11. For single-phase natural circulation, the input power is 0.14 kW, the operating pressure is 24 bar and inlet subcooling temperature is 18^{o}C. For two-phase natural circulation, the input power is 3.90 kW and other test parameters are same as single-phase natural circulation case. The rolling angle is 40 degrees and the rolling period is set to 6 seconds.

The simulation result predicted by TAPINS-M for fluctuation of mass flow under rolling motion was compared with experimental data, as shown in Figs. 4.12. and 4.13. The fluctuation of mass flow was produced in test section by rolling motion. The fluctuation amplitude and period which were calculated by the TAPINS-M code were close to being an actual phenomenon in MARMS. Also, average mass flow rate under natural circulation predicted by code showed an excellent agreement with the data. The flow instability can be occurred by the flow resistance increases due to the generation of the vapor in the two-phase flow test as shown by the arrow in Fig. 4.13.

Two-phase forced convection under rolling motion

Two-phase forced convection experiments using MARMS basically divided into two flow range (flow control by pump), i.e. low flow rate of 0.02 kg/s and high mass flow region of 0.07 kg/s, were conducted. Among the various test cases, two cases of the flow fluctuation were simulated with TAPINS-M. The flow fluctuation in each case by the rolling motion was compared with experimental data.

Figure 4.14 depicts the results of TAPINS-M calculation in the operating pressure of 16 bar, mass flow rate of 0.02 kg/s and inlet subcooling temperature of 15^{o}C. The maximum rolling angle was 40 degrees and the rolling period was set to 6 seconds. In the low flow rate region, the form of flow fluctuation did not show to ideal sine function. A concave region appeared at the wave crest. It was considered due to the influence of the degree of boiling, pump head and distance between heat sink and source.

Figure 4.15 shows the results of the TAPINS-M calculation in the high mass flow rate (0.07 kg/s) condition with the operating pressure of 13 bar, inlet subcooling temperature of 15^{o}C. The maximum rolling angle and period are same as the previous case. Another interesting observation in this case was that a symmetrical pattern of flow fluctuation appeared twice in a period. The flow fluctuation was smaller than the low flow experiment because of a large head pump and relatively small impact of the acceleration by rolling motion in this case. The developed code succeeds in predicting the aforementioned pattern of flow fluctuation, as shown in Fig. 4.15.

4.3.3 Analysis on Transient Condition under Rolling Motion

The TAPINS-M application to the transient conditions of the MARMS is presented in this section. These tests were simulated hypothetical transients; (1) the pump trip, (2) the depressurization and pressurization.

Pump trip

Using MARMS, pump trip was simulated. Figure 4.16 shows the variation of the coolant flow rate, differential pressure, system pressure and wall temperature of the heater when the pump abruptly stopped. Condition of forced convection was maintained by pump operating for the first 100 seconds and after that, the pump was tripped.

In this transient, the mass flow rate was rapidly dropped followed by the pump trip, since the flow rate was kept nearly constant by natural circulation as shown in more detail in Fig. 4.17. The rate of mass flow variation in natural circulation is larger than in forced convection. As the pump was tripped, the temperature at heater wall was slightly increased, causing a system pressure increasing by reducing the heat transfer rate near heater wall simultaneously. Also, the differential pressure in the inlet and outlet of the test section rose and fluctuation of differential pressure occurred by rolling motion.

The experimental data and the simulation results are plotted in Figs. 4.17. TAPINS-M overpredicted in the average mass flow and the fluctuation rate in the natural circulation and forced convection. Although the TAPINS-M results tend to overpredict the performance, qualitative agreement between the code and test data was satisfactory.

Depressurization and pressurization

The other transient problem in the present study was to describe the depressurization and pressurization of the system as shown in Fig 4.18. To simulate the transient condition, the pressure of the loop decreased and then, increased by rapid charging or venting of the nitrogen gas in the accumulator.

As bladder was contracted or expanded, the system pressure decreased or increased for 150 seconds. The wall temperature of the test section was decreased with the depressurization of system at the same time. The reason of this transient was that the amount of heat transfer was enhanced by an accelerated nucleate boiling on the heater wall. According to the pressurization of system, the temperature at the heater wall increased due to the deceasing of the bubble departure from heater wall. This phenomenon can be derived through the behavior of wall temperature. It can be deduced that fluctuation of temperature in the depressurization was larger than that in the pressurization. It was noted that the heat removal rate was affected by the behavior of bubbles. As the pressure was lowered, the variation of mass flow rate was slightly decreased as shown in detail in Fig. 4.19.

The flow variation predicted by TAPIN-M was compared to the experimental data from MARMS as shown in Fig. 4.19. Since TAPINS-M employs HEM as the governing equations, it cannot predict well the amplitude of mass flow variation. Approximations in HEM have inherent limitations. The equilibrium pressure and velocity assumptions limit problems to those where the phases are finely dispersing and flowing in the same directions. HEM cannot reflect the relative velocity the resistance between phases in low flow rate region.

The calculation result of TAPINS-M for the behavior of fluid in the test section exit also plotted in Fig. 4.20. For the trend of temperature behavior, the prediction of TAPINS-M agreed well with the measured data. According to the rolling motion, the flow rate was fluctuated in the subcooled temperature region. However, the temperature did not fluctuate any longer when it reached the saturation temperature. The prediction of the code exhibits some deviations from the temperature value of the test data and temperature fluctuation. It is because that the temperature variation is affected by the overpredicted flow fluctuation.

Table 4.1 Assessment matrix of TAPINS-M

Problem type	Assessment objectives
Two-phase forced and natural circulation under rolling motion	CHF model
Single-phase natural circulation under rolling motion	Moving model (Fluid flow fluctuation)
Two-phase natural circulation under rolling motion	
Two-phase forced convection under rolling motion	
Transient condition	Depressurization & pressurization
	Pump trip

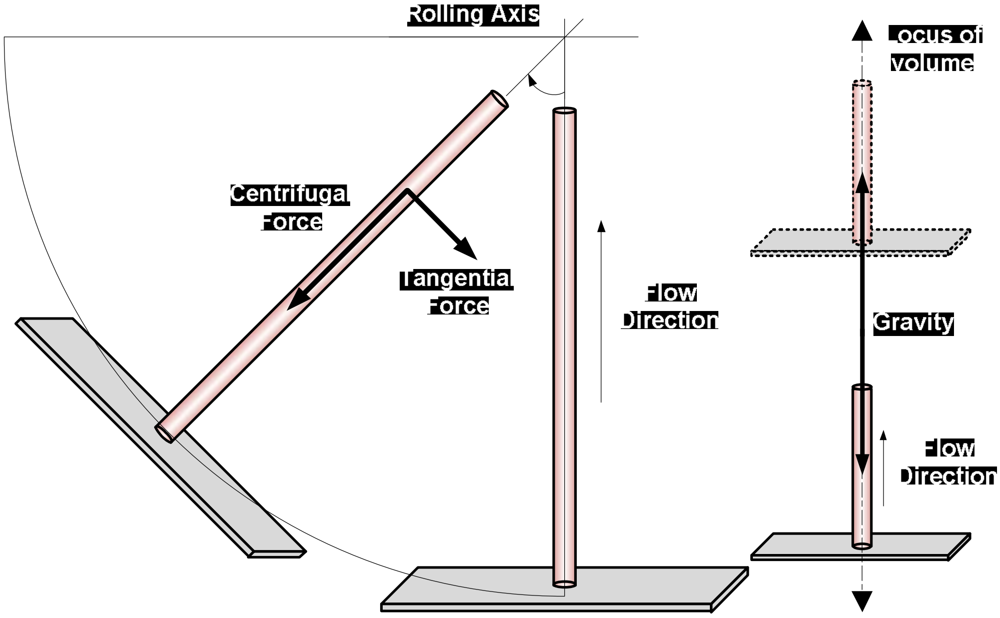

Figure 4.1 Description of rolling and heaving motion

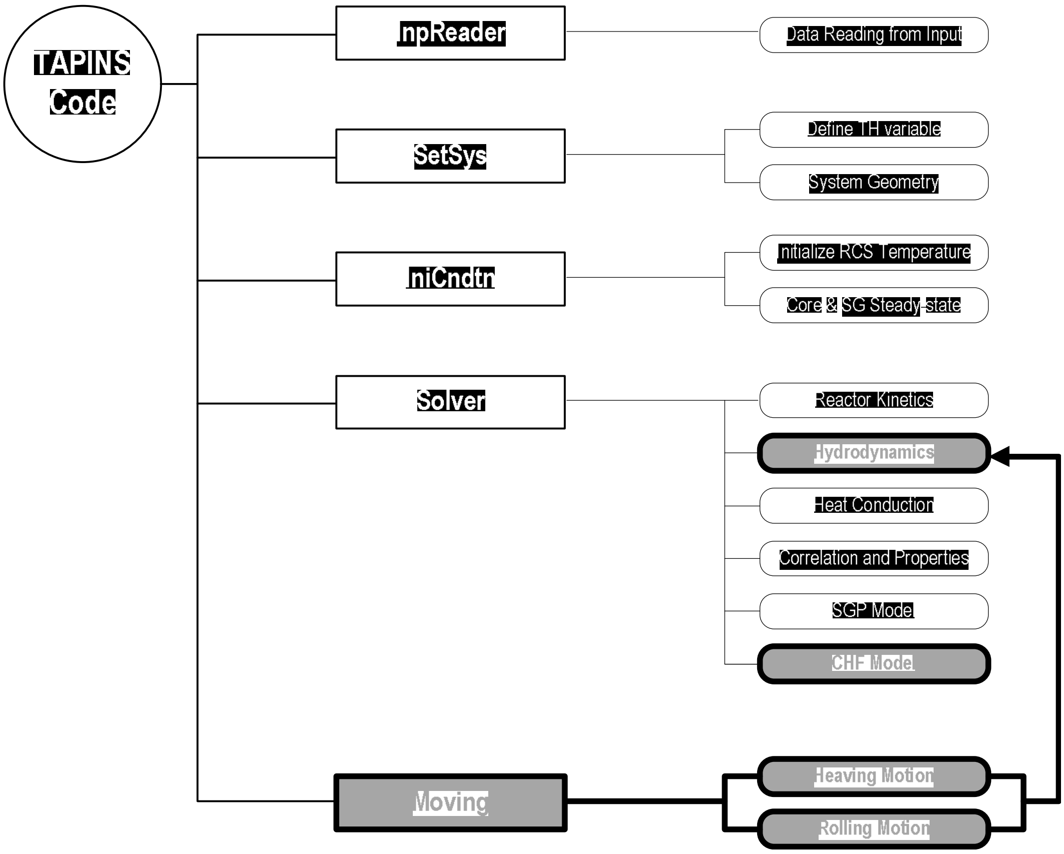

Figure 4.2 Code structure of TAPINS

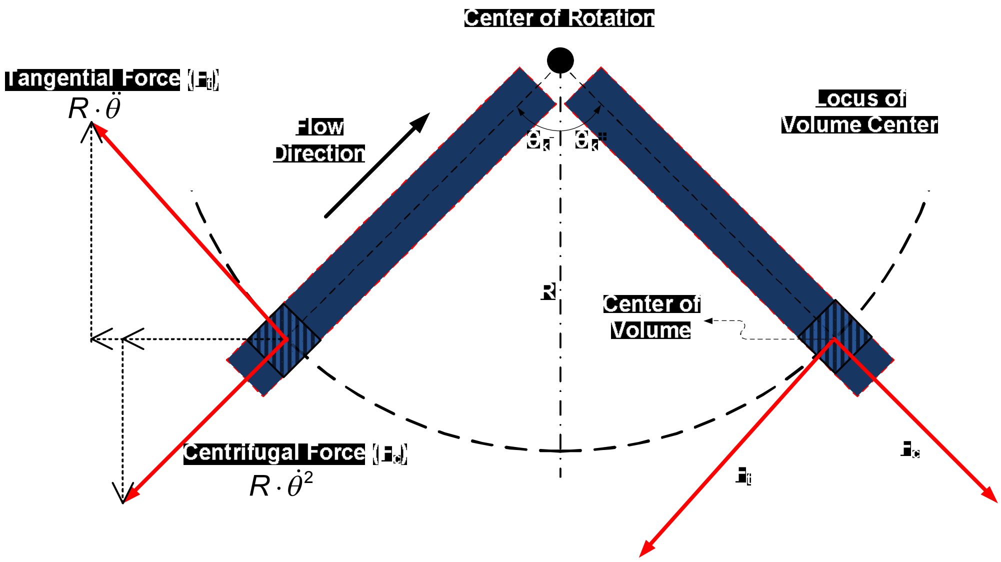

Figure 4.3 Centrifugal and tangential forces for rolling motion

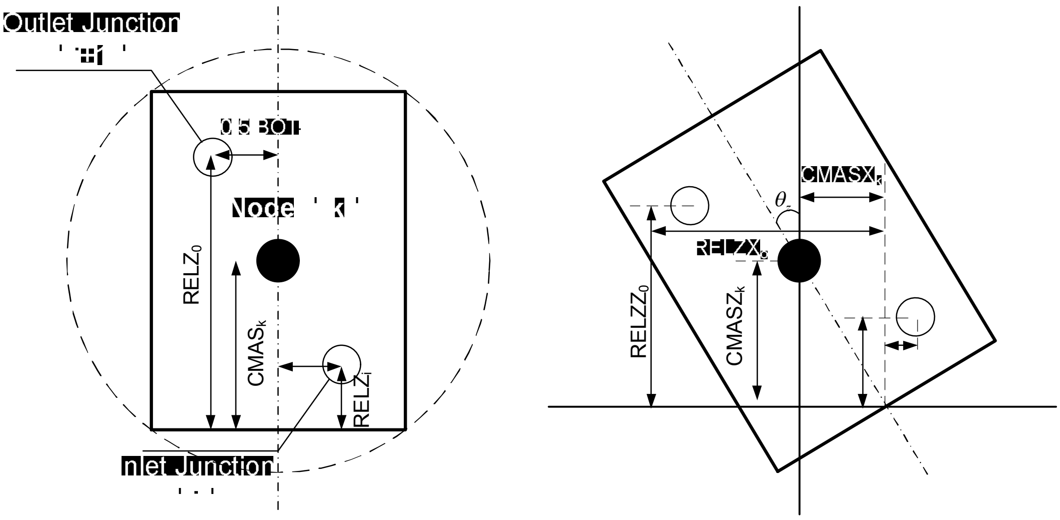

Figure 4.4 Modeling of control volume under rolling motion

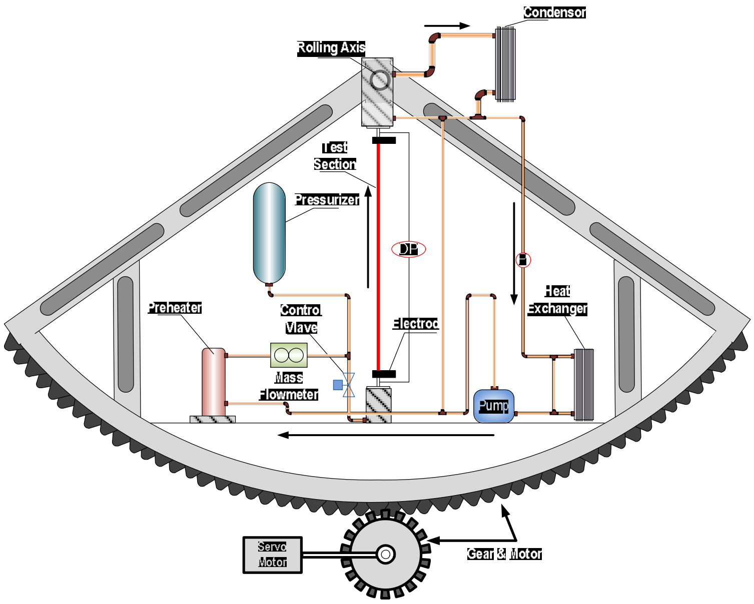

Figure 4.5 Two-dimensional schematic diagram of MARMS

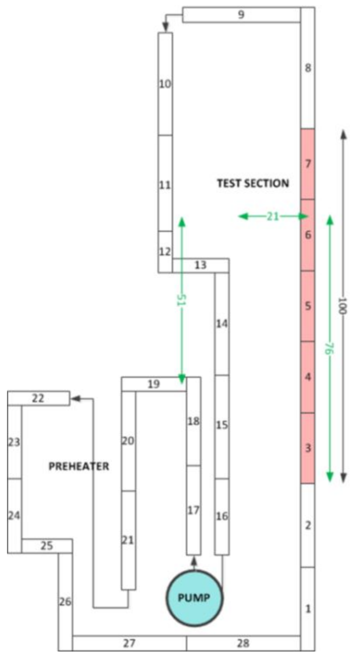

Figure 4.6 Nodalization of MARMS for TAPINS-M analysis

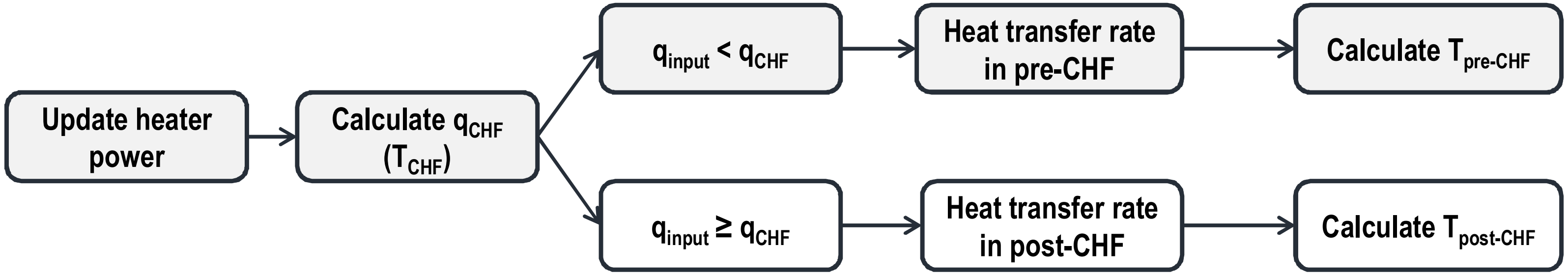

Figure 4.7 Calculation procedure of TAPINS-M for CHF

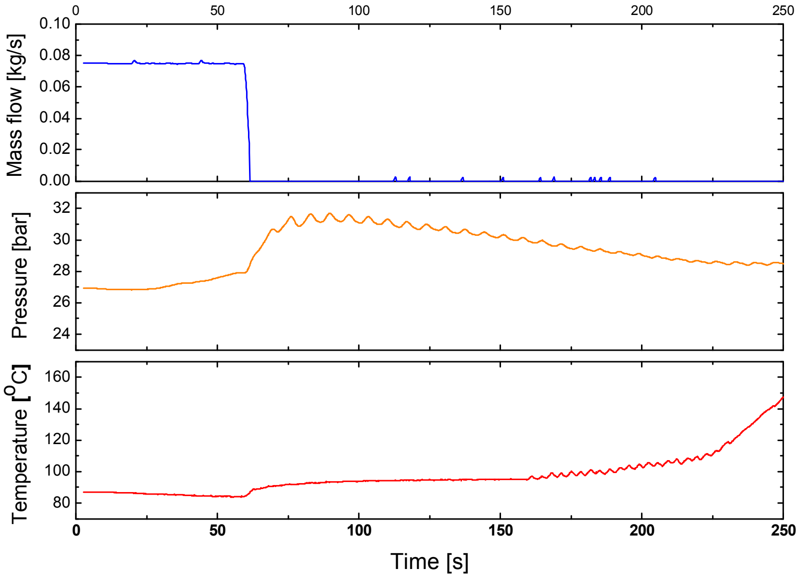

Figure 4.8 Responses of mass flow rate, pressure and temperature near and at CHF condition

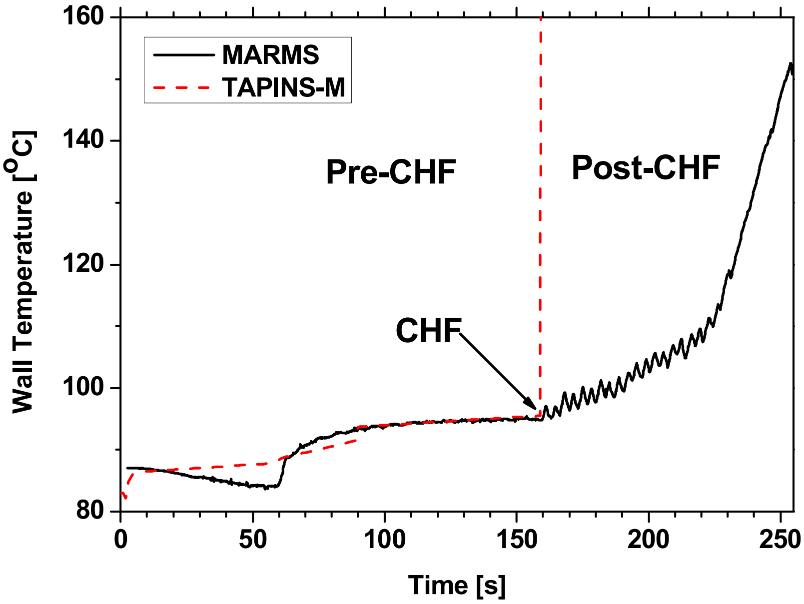

Figure 4.9 Comparison of TAPINS-M with MARMS CHF test

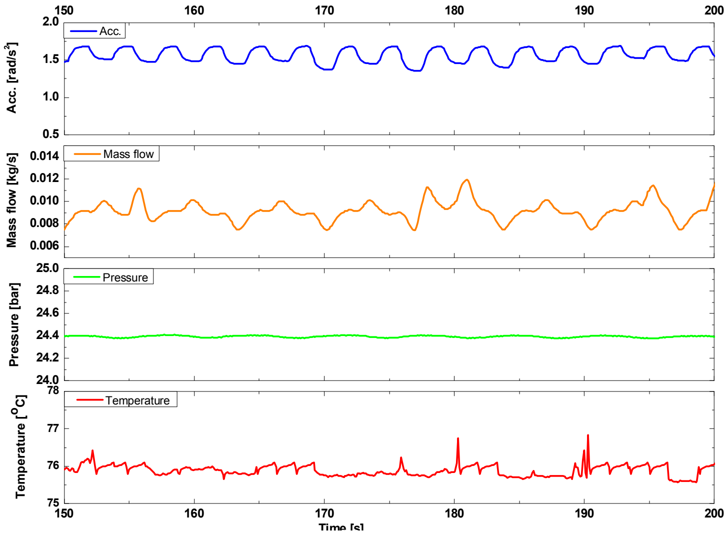

Figure 4.10 Responses of mass flow rate, pressure and temperature at single-phase natural circulation under rolling condition

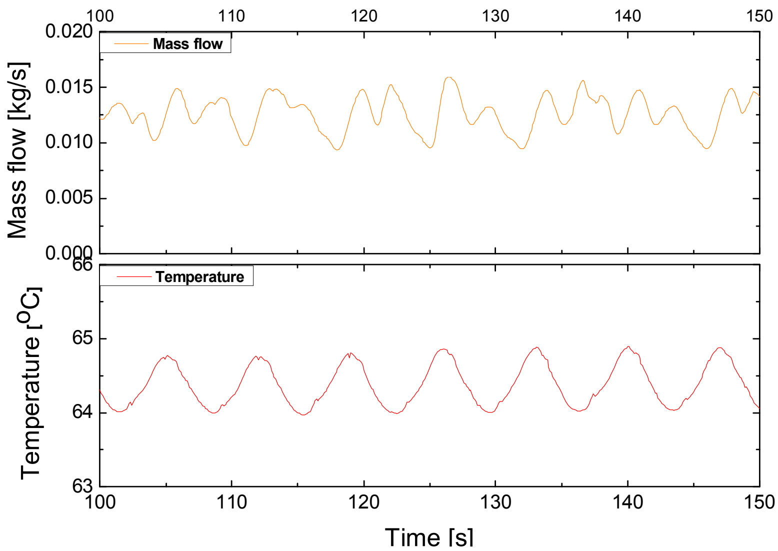

Figure 4.11 Responses of mass flow rate and temperature at two-phase natural circulation under rolling condition

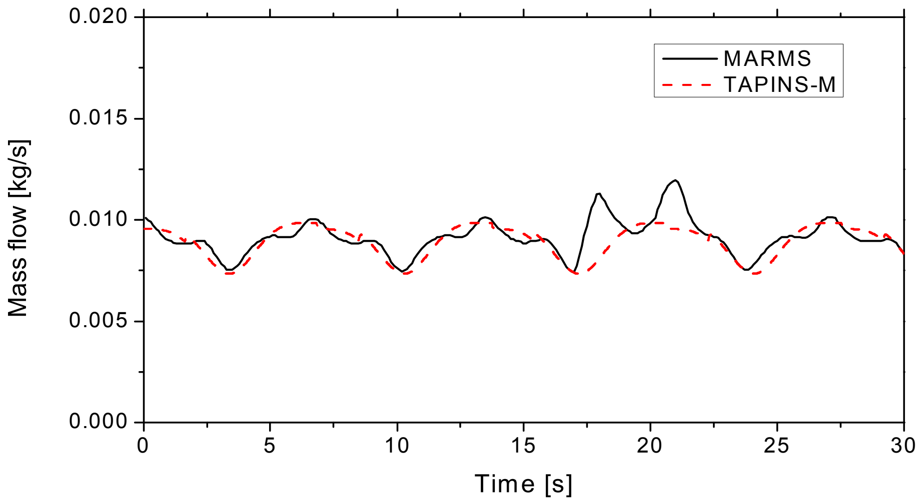

Figure 4.12 Comparison between the experimental results and TAPINS-M for fluctuation of mass flow (single-phase natural circulation)

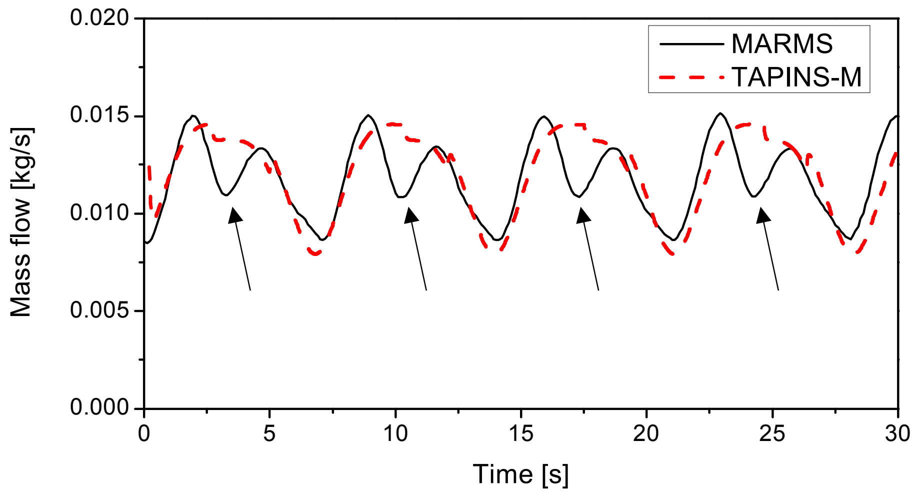

Figure 4.13 Comparison between the experimental results and TAPINS-M for fluctuation of mass flow (two-phase natural circulation)

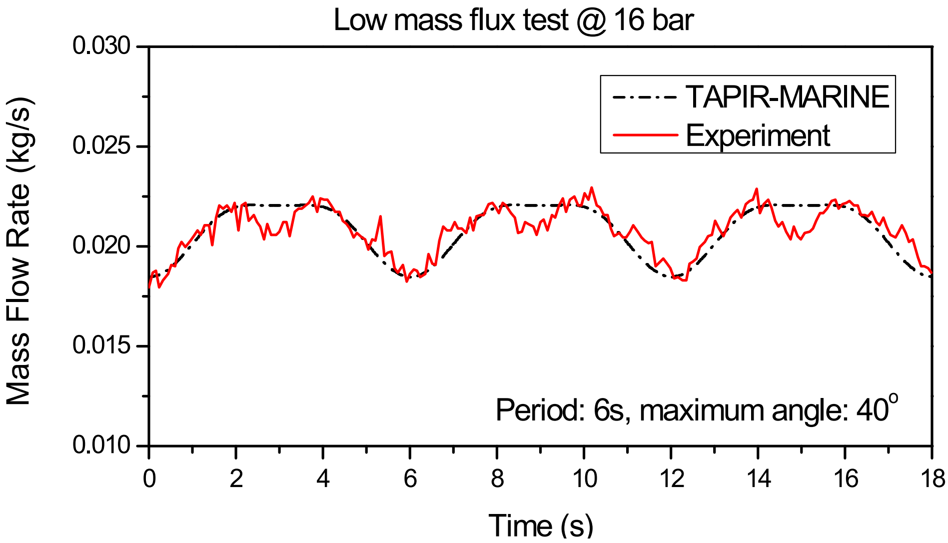

Figure 4.14 Comparison between the experimental results and the TAPINS-M for two-phase forced convection under rolling motion (low mass flux)

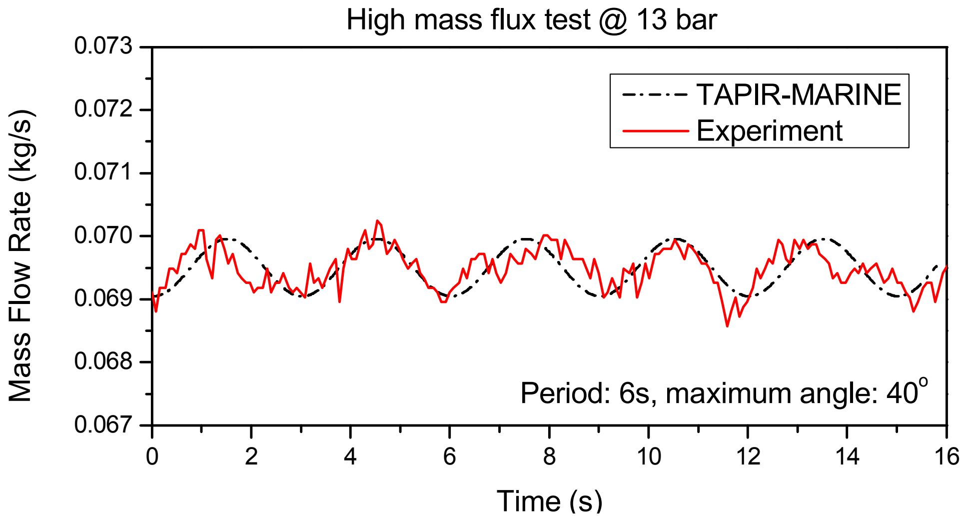

Figure 4.15 Comparison between the experimental results and the TAPINS-M for two-phase forced convection under rolling motion (high mass flux)

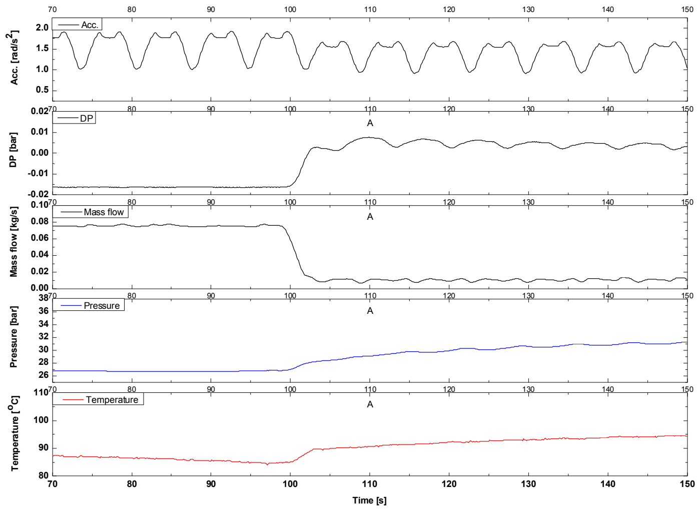

Figure 4.16 Responses of mass flow rate, pressure, DP and temperature after pump trip under rolling condition

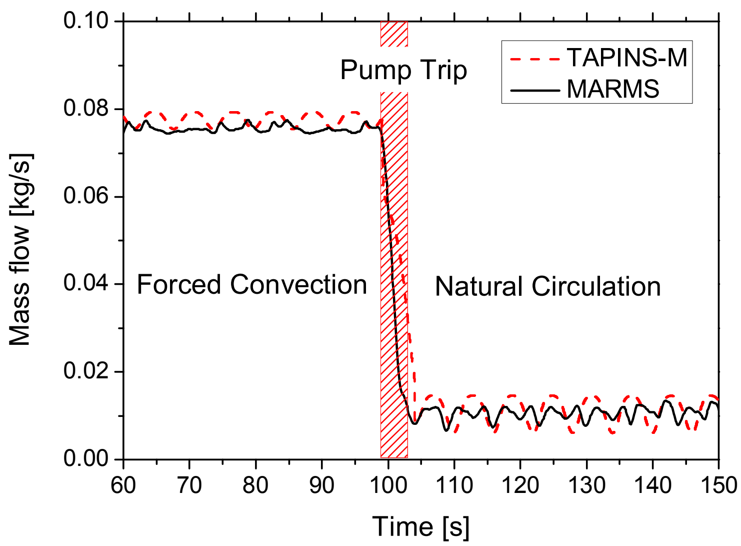

Figure 4.17 Comparison between the experimental results and the TAPINS-M for mass flow after pump trip under rolling motion

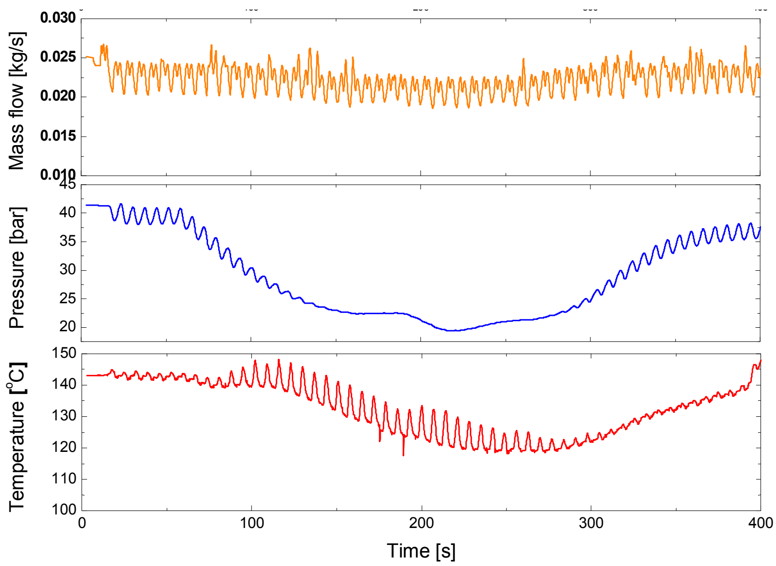

Figure 4.18 Responses of mass flow rate, pressure and temperature at depressurization and pressurization under rolling condition

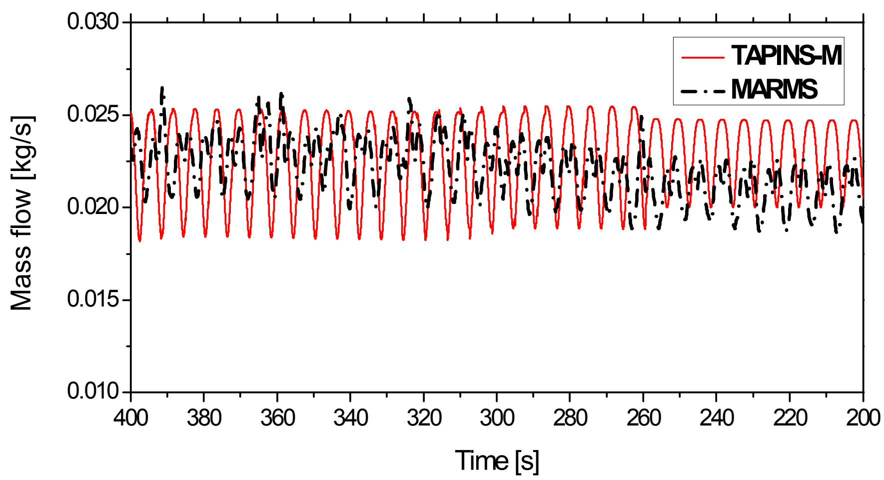

Figure 4.19 Comparison between the experimental results and the TAPINS-M for mass flow under rolling motion at depressurization and pressurization

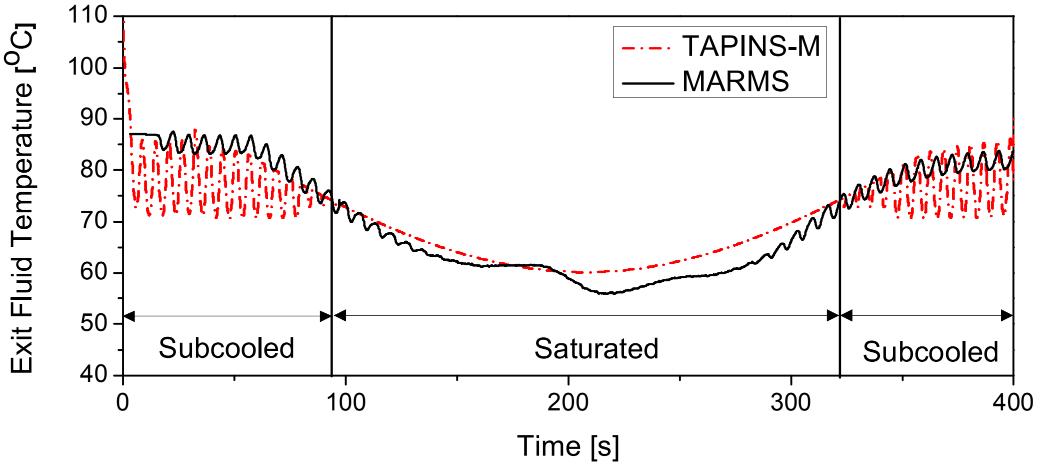

Figure 4.20 Comparison between the experimental results and the TAPINS-M for exit fluid temperature under rolling motion at depressurization and pressurization

Chapter 5

Conclusions

Marine reactors have different thermal-hydraulic characteristics compared to the current land-based reactors due to their different design features and operation conditions. In this study, a thermal-hydraulic code named TAPINS-M has been developed to investigate the normal and transient conditions of a marine reactor. TAPINS-M adopted the appropriate moving model for analysis of the marine reactor dynamics such as the heaving and rolling motions. It also adopted the developed CHF prediction model as it is a crucial safety factor to consider in safety design and operation of a marine nuclear reactor.

In order to develop the CHF correlation concerned with the rolling motion effect, the CHF behavior under rolling motion has been experimentally investigated. The CHF characteristics under rolling motion can be summarized as follow:

- The CHF enhancement is dependent on the mass flux, pressure and rolling amplitude.
- The CHF ratio decreases with decreasing mass flux (below certain mass flux) at intermediate pressures (13 and 16 bar).

- At the intermediate pressure, with increasing mass flux (over certain mass flux), the CHF is enhanced or similar to the value of the stationary CHF.
- At the high pressure (24 bar), the CHF is enhanced at all mass flux regions and inlet subcooling.

The CHF mechanisms under rolling motion can be summarized as follows;

- In the DNB region (over certain mass flux at intermediate pressure and high pressure), the combination of tangential force and high mass flux contribute to CHF enhancement due to the increase of the vapor layer agitation and bubble departure rate.
- In the dryout region (below certain mass flux at intermediate pressures), the rolling motion promotes the reduction of film thickness due to the minimum inlet mass flow or droplet entrainment rate in liquid film to vapor core.

Based upon dimensionless groups, equations and an interpolation factor, an empirical CHF correlation has been developed which is consistent with the experimental data for uniformly heated tubes that are internally cooled by R-134a under rolling motion. The flow regime was determined through the prediction method for annular flow. Non-dimensional numbers and functions were decided by the CHF mechanisms in each region. Since the mechanisms of CHF for transition region (TR) cannot be clearly described, the correlation for the TR was interpolated using the LFD and DNB correlations. For the interpolation, the power interpolation method was adopted. The functional form of power is logistic function form as the void fraction at OAF. The suggested correlation predicted the CHF Ratio plausibly with showing an average error of -0.59 and 2.51% for RMS.

TAPINS-M was validated with various steady-state and transient analyses on the 6 assessment items. The validation results demonstrated that the calculation results showed reasonable agreement with the experimental data. Thus, it can be concluded that TAPINS-M could provide a reasonable prediction on CHF under rolling motion, and can be used in normal and transient conditions of marine reactor such as natural and forced circulations. Especially, it should be noted that TAPINS-M could contribute to and improve the prediction on the transient simulation of the pump trip and pressure transition.

Nomenclature

a	Acceleration (m s^{-2})
A	Amplitude of oscillating inlet flow rate (kg s^{-1}), cross-sectional area (m^2)
C_0	Distribution parameter
C_p	Specific heat at constant pressure (J $kg^{-1}K^{-1}$)
D	Diameter (m)
D_h	Hydraulic diameter (m)
f	Darcy friction factor
F	Scaling factor
F_p	CHF correction factor
Fr	Froud number
g_o	Gravity acceleration (m s^{-2})
Δg	Amplitude of oscillating gravity acceleration (m s^{-2})
G	Mass flux (kg $m^{-2}s^{-1}$)
h	Specific enthalpy (J kg^{-1})
h_{fg}	Latent heat (J kg^{-1})
j_g	gas superficial velocity (m s^{-1})
k	Thermal conductivity (W $m^{-1}K^{-1}$), form loss coefficient
L	Length (m)
L_h	Heated length (m)
P	Pressure (bar)
P_h	Heated perimeter (m)
ΔP_{pump}	Pressure head provide by the pump (m)

T	Temperature (^{o}C)
T_s	period of gravity oscillation (s)
q''	Heat flux (kW m^{-2})
Q	Volumetric flow rate (m3 s^{-1})
r	Radius (m)
R	Radius from rolling axis (m)
Re	Reynolds number
Re_R	Reynolds number for rolling motion
S	Slip ratio
t	Time (s)
Tr	Transit time of the inlet flow through the test section (s)
u_θ	Velocity (m s^{-1})
V_{gj}	Drift velocity (m s^{-1})
We	Weber number
y_{min}	ratio of minimum inlet velocity (m s^{-1})
z	Spatial coordinates (m)

Greek Letters

α	Void fraction
α_{an}	Void fraction at OAF
β	$\left\|\partial\theta / \partial P\right\|_{saturation}$, volumetric expansion coefficient (K^{-1}), angular acceleration (rad s^{-2})
γ	$\left\|\partial\left(\rho_l / \rho_g\right) / \partial P\right\|_{saturation}$

μ	Dynamic viscosity (Pa s)
ρ	Density (kg m^{-3})
σ	Surface tension (N m^{-1})
Θ	Rolling amplitude (degree)
τ	Rolling period (s)
χ	Quality
χ_{an}	Quality at OAF
χ_c	Critical Quality
χ_{tr}	True quality
ω	Angular velocity (rad s^{-1})
υ	Specific volume (m^2 s^{-1})
Ψ	Modeling parameter

Subscripts

avg	Average
c	Critical heat flux, centrifugal
t	Tangential
ex	Exit
l	Liquid phase
g	Vapor phase
min	Minimum
o	Initial value
k	Node index

M	Model
W	Water
x	x-direction
z	z-direction

References

Ahmad, S. Y., “Axial distribution of bulk temperature and void fraction in a heated channel with inlet subcooling,” *Journal of Heat Transfer Trans. ASME,* Vol. 92, pp. 595-609, 1970.

Ahmad, S. Y., "Fluid to Fluid modeling of critical heat flux: A compensated distortion model," *International Journal of Heat and Mass Transfer*, Vol. 16, pp. 641, 1973.

Barnett, P. G., “The scaling of forced convection boiling heat transfer," United Kingdom Atomic Energy Authority, Report No. AEEW-134, 1963

Buckingham, E., “On Physically Similar Systems: Illustrations of the use of dimensional equations,” *Physical Review*, 4, vol. 4, pp. 345-376, 1914.

Chang, Y. P. and Snyder, N. W., "Heat transfer in saturated boiling,” *NUTHOS-5*, Beijing, China, April, 1997.

Cioncolini, A. and Thome, J. R., “Void fraction prediction in annular two-phase flow,” *International Journal of Multiphase Flow*, Vol. 43, pp. 72-84, 2012.

Coffield, R. D., "A subcooled DNB investigation of freon-113 and its similarity to subcooled water DNB data,” *Nuclear Engineering and Design*, Vol. 11, pp. 143, 1969.

Coleman, H. W. and Steele, Jr. W. G., Experimentation and Uncertainty Analysis for Engineers, John Wiley & Sons, 1989.

Collier, J. G. and Thome, J.R., Convective Boiling and Condensation, Oxford University Press, Oxford, pp. 325-374, 1994.

Dix, G. E., “Freon-water modeling of CHF in round tubes,” ASME-Paper No. 70-HT-26, Detroit, Michigan, 1970.

Dix, C.E., “Vapor void fractions for forced convection with subcooled boiling at low flow rates,” Ph.D. Thesis, 1971.

Fujino, M., “Some concepts of future nuclear ship” *N'ocean 2000: International workshop on utilization of nuclear power in oceans*, Tokyo, Japan, 2000.

Gao, P., Pang, F. and Wang, Z., “Theoretical research for effect of ocean conditions on natural circulation,” *Nuclear Power Engineering*, Vol. 15, pp. 330–335, 1995.

Gao, P., Pang, F. and Wang, Z., “Mathematical model of primary coolant in nuclear power plant influenced by ocean conditions,” *Journal of Harbin Engineering University*, Vol. 18, pp. 24–27, 1997.

Gao, P., Liu, S. and Wang, Z, “Effect of pitching and rolling upon natural circulation,” *Nuclear Power Engineering*, Vol. 20, pp. 228–231, 1999.

Groeneveld, D. C. et al., “1986 AECL-UO critical heat flux lookup table,” *Heat Transfer Engineering*, Vol. 7, pp. 46, 1986.

Groeneveld, D. C. et al., “Prediction of critical heat flux (CHF) for non-aqueous fluids in forced convective boiling,” *Proceeding of the 8th International Heat Transfer Conference,* San Francisco, USA, 1986.

Hong S. D., Chun, S. Y., Yang, S. Y., Chung, M. K. and Lashgari F., “A phenomenological prediction of dryout based on the churn-to-annular flow transition criterion in uniformly heated vertical tubes,” *Proceedings of 4th JSME-KSME Thermal Engineering Conference*, Kobe, Japan, 2000.

Hewitt, G. G., “Critical heat flux in flow boiling,” 6th Int. Heat Transfer Conf., Toronto, Canada, Vol. 6, pp.143-152, 1978.

Hwang, J.S., Kim, J.W., Nam, H.U. and Park, G.C., “Assessment of MARS code for predicting critical heat flux under heaving conditions,” *Nuclear Technology* Vol. 176, pp. 260-273, 2011.

Isshiki, N, "Effect of heaving and a listing upon thermo hydraulic performance and critical heat flux of water-cooled marine reactors,” *Nuclear Engineering and Design*, Vol. 6, p.138, 1965.

Ishida, T., Kunsunoki, T., Murata, H., Yokomura, T. and Kobayashi, M., “Thermal-hydraulic behavior of a marine reactor during oscillations,” *Nuclear*

Engineering and Design, vol. 120, pp. 213-225, 1990.

Ishida, T., Kunsunoki, T., et al., "Effect of ship motion on the reactor system: experimental voyage of nuclear powered ship MUTSU," *International Conference on New Trends in Nuclear System Thermal-Hydraulics*, Pisa, Italy, 1994.

Ishida, T. and Yoritsune, T., "Effects of ship motion on natural circulation of deep sea research reactor DRX," *Nuclear Engineering and Design*, Vol. 215, pp. 51–67, 2002.

Iyori, I., Aya, I., Murata, H., Kobayashi, M. and Nariai, H., "Natural circulation of integrated-type marine reactor at an inclined attitude," *Nuclear Engineering and Design*, Vol. 99, pp. 423–430, 1987.

Jensen, M. K., "A correlation for predicting the critical heat flux condition with twisted-tape swirl generators," *International Journal of Heat and Mass Transfer,* Vol. 27, pp. 2171-2173, 1984.

Kim, J. H., Kim, T. W., Lee, S. M. and Park, G. C., "Study on the natural circulation characteristics of the integral type reactor for vertical and inclined conditions," *Nuclear Engineering and Design*, Vol. 207, pp. 21–31, 2001.

Kusunoki, T., Odano, N., Yoritsune, T., Ishida, T., Hoshi, T. and Sako, K., "Design of advanced integral-type marine reactor, MRX," *Nuclear Engineering and Design*, vol. 201, pp. 155-175, 2000.

Katto, Y., "An analysis of the effect of inlet subcooling on critical heat flux of forced convection boiling in vertical uniformly heated tubes," *International Journal of Heat and Mass Transfer*, Vol. 22, pp. 1567, 1979.

Katto, Y., “Prediction of Critical Heat Flux for annular flow in tubes taking into account the critical liquid film thickness concept,” *International Journal of Heat and Mass Transfer*, Vol. 27, pp. 229-242, 1984.

Kim, C. H., Bang, I. C. and Chang, S. H., “Critical heat flux performance for flow boiling of R-134a in vertical uniformly heated smooth tube and rifled tubes,” *International Journal of Heat and Mass Transfer,* Vol. 48, pp. 2868-2877, 2005.

Kim, D. H., Lee, Y. H. and Chang, S. H., “Effects of mechanical vibration on critical heat flux in vertical annulus tube,” *Nuclear Engineering and Design,* Vol. 237, pp. 982-987, 2007.

Kim, Y. I., Baek, W. P. and Chang, S. H., “Critical heat flux under flow oscillation of water at low-pressure, low-flow conditions,” *Nuclear Engineering and Design,* Vol. 193, pp. 131-143, 1999.

Lee, Y. G., Kim, J. W., and Park, G. C., "Development of a thermal–hydraulic system code, TAPINS, for 10MW regional energy reactor," *Nuclear Engineering and Design*, vol. 249, pp. 364-378, 2012.

Lee, Y. H., Kim, D. H. and Chang, S.H., “An experimental investigation on the critical heat flux enhancement by mechanical vibration in vertical round tube," *Nuclear Engineering and Design,* Vol. 34, pp. 47-58, 2004.

Levy, S., "Forced convection subcooled boiling prediction of vapor volumetric fraction," *International Journal of Heat and Mass Transfer,* Vol. 10, pp. 951-965, 1967.

Levy, S., Healzer, J. M. and Abdollanhian D., "Prediction of Critical Heat Flux in Vertical Pipe Flow," *Nuclear Engineering and Design*, Vol. 65, pp. 131-140, 1981.

McQuillan, K. W. and Whalley, P. B., "Flow patterns in vertical two-phase flow," *International Journal of Multiphase Flow*, Vol. 11, pp. 161-175, 1985.

Mishima K. and Ishii, M., "Flow regime transition criteria for upward two-phase flow in vertical tubes," *International Journal of Heat and Mass Transfer*, Vol. 27, pp. 723-737, 1984.

Moon, S. K., Baek, W. P. and Chang, S.H., "Parametric trend analysis of the critical heat flux based on neural networks," *Nuclear Engineering and Design*, vol. 163, pp. 29-49, 1996.

Murata, H., Iyori, I. and Kobayashi, M., "Natural circulation characteristics of a marine reactor in rolling motion," *Nuclear Engineering and Design,* Vol. 118, pp. 141-154, 1990.

Murata, H., Sawada, K. and Kobayashi, M., “Experimental investigation of natural convection in a core of a marine reactor in rolling motion,” *Journal of Nuclear Science Technology,* Vol. 37, pp. 509-517, 2000.

Murata, H., Sawada, K. and Kobayashi, M., “Natural circulation characteristics of a marine reactor in rolling motion and heat transfer in the core,” *Nuclear Engineering and Design,* Vol. 215, pp. 69-85, 2002.

Okawa, T., Goto, T., Minamitani, J. and Yamagoe, Y., “Liquid film dryout in a boiling channel under flow oscillation conditions,” *International Journal of Heat and Mass Transfer,* Vol. 52, pp. 3665-3675, 2009.

Otsuji, T. et al., "Critical heat flux of forced convection boiling in an oscillating acceleration field,” *Nuclear Engineering and Design*, Vol. 71, pp. 15, 1982.

Ozawa, M., Umekawa, H., Mishima, K., Hibiki, T. and Saito, Y., “CHF in oscillatory flow boiling channels,” *Trans IChemE 79 Part A,* pp. 389-401, 2001.

PROPATH GROUP, "PROPATH: a program package for thermophysical properties of fluids, Ver. 12.1," 2001.

Stevens, G. F. and Kirby, G. J., “A quantitative comparison between burnout data for water at 1000 psia and Freon-12 at 155 psia. Uniformly heated round tubes, vertical upflow,” United Kingdom Atomic Energy Authority, Report No. AEEW-R327, 1964.

Semeria, R. and Hewitt, G. F., "Aspects of heat transfer in two-phase one-component flows, Seminar on Recent Developments in Heat Exchangers," Int. Center for Heat and Mass Trasnfer, Trogir, Yugoslavia.

Stevens, G. F. and Kirby, G. J., "A quantitative comparison between burn-out data for water at 1000 lb/in^2 and Freon-12 at 155 lb/in^2 uniformly heated round tubes, vertical upflow," AEEW-R327, 1964.

Su, G., Zhang, J. and Guo, Y., "Effects of ocean conditions upon the passive residual heat removal system (PRHRS) of ship rector," *Atomic Energy Science and Technology*, Vol. 30, pp. 487–491, 1996.

Taitel, Y., Dukler, A. E. and Bornea D., "Modeling flow pattern transitions for steady upward gas-liquid flow in vertical tubes," *AIChE. J.* Vol. 26, pp. 345-354, 1980.

Tan, S. and Gao, P., "Experimental and theoretical study on natural circulation capacity under rolling motion condition," *Proceedings of the 15th International Conference on Nuclear Engineering* (ICONE15-10120), Nagoya, Japan, 2007.

Tan, S., Zhang, H., Pang, F. and Gao, P., "Characteristic of single-phase natural circulation under rolling," *Nuclear Power and Engineering*, Vol. 26, pp. 554–558, 2005a.

Tan, S., Zhang, H., Pang, F. and Gao, P., "Experimental study on the effect of rolling motion upon single-phase natural circulation," *Proceedings of the 13th International Conference on Nuclear Engineering* (ICONE13-50094), Beijing, China, 2005b.

Tan, S., Zhang, H., Pang, F. and Gao, P., "Experimental research of effect of rolling upon heat transfer characteristic of natural circulation," *Nuclear Power and Engineering*, Vol. 27, pp. 33–36, 2006.

Tan, S., Gao, P. and Su, G., "Experimental and theoretical study on natural circulation flow under rolling motion condition," *Journal of Harbin Engineering University*, Vol. 28, pp. 1213–1217, 2007.

Tan, S.C., Su, G.H. and Gao, P.Z., "Experimental and theoretical study on single-phase natural circulation flow and heat transfer under rolling motion condition," *Applied Thermal Engineering,* Vol. 29, pp. 3160-3168, 2009.

Tan, S.C., Su, G.H., and Gao, P.Z., "Experimental study on two-phase flow instability of natural circulation under rolling condition," *Annals of Nuclear Energy* Vol. 36, pp. 103-113, 2009.

Todreas, N. E. and Kazimi, M. S., *Nuclear systems*, Hemisphere Pub. Corp., New York, 1990.

Tong, L. S. and Tang, Y. S., Boiling heat transfer and two-phase flow, Taylor & Francis, Washington D.C, 1997.

Umekawa, H., Ozawa, M., Miyazaki, A., Mishima, K. and Hibiki, T., "Dryout in a boiling channel under oscillatory flow condition," JSME Series B Vol. 39, pp. 412-418, 1996.

Wallis, G. B., One-dimensional two-phase flow, Wiley, New York, 1969.

Watanabe, N., Aritomi, M. and Kikura, H., "Thermal hydraulic flow oscillation characteristics in multiform channels under natural circulation and low pressure conditions," *Journal of Nuclear Science and Technology*, Vol. 45, pp. 160–170, 2008.

Weisman, J., Tang, J. Y. and Usman, S., "A phenomenological model for boiling heat transfer and the critical heat flux in tubes containing twisted tapes," *International Journal of Heat and Mass Transfer*, Vol. 37, pp. 69-80, 1994.

Whalley, P. B., Hutchinson, P. and Hewitt, G. F., "The calculation of Critical Heat Flux in Forced Convection Boiling," *5th International Heat Transfer Conference*, B6.11, Tokyo, Japan, 1974.

Woodward, J. B., "Natural circulation experiments in an oscillating force field", Ph.D. thesis, University of Michigan, Ann Arbor, 1965.

Yang, J., Jia, B. and Yu, J., "Simulation model of natural circulation in PWR coolant system under ocean condition," *Chinese Journal of Nuclear Science and Engineering*, Vol. 22, pp. 125–129, 2002.

Zhao, D. W., Su, G. H., Liang, Z. H., Zhang, Y. J., Tian, W. X. and Qiu, S. Z., “Experimental research on transient critical heat flux in vertical tube under oscillatory flow condition,” International Journal of Multiphase Flow 37 (9) (2011) 1235-1244.

Zigrang, D. and Sylvester, N., "A review of explicit friction factor equations," *Journal of Energy Resources Technology*, vol. 107, pp. 280-283, 1985.

Zuber, N. and Findlay, J., “Average volumetric concentration in two-phase flow systems,” *Journal of Heat Transfer*, Vol. 87, pp. 453-468, 1965.

Zvirin, Y., "A review of natural circulation loops in pressurized water reactors and other systems," *Nuclear Engineering and Design*, vol. 67, pp. 203-225, 1982.

Appendix A

Uncertainty Analysis

The uncertainty (Coleman, 1989) in each measured parameter is presented below at a 95 percent confidence level. These uncertainties are combined statistically to evaluate the possible errors in calculated parameters.

- Mass flux of R-134a
- Inlet and Outlet Pressure
- Inlet and Outlet Temperature
- Rolling Angle and Period
- Heat Flux

I. Mass Flux of R-134a

R-134a mass flux can be obtained from the mass flow rate of R-134a measured by Coriolis mass flow meter and flow area.

$$G_{R134a} = \frac{\dot{m}_{R134a}}{A_{cr}} = \frac{\rho_{R134a} Q_{R134a}}{A_{cr}}$$

Then, the uncertainty of the R-134a mass flux can be written using Root Sum Square method as follows,

$$\frac{U_{G_{R134a}}}{G_{R134a}} = \pm\sqrt{\left(\frac{B_{G_{R134a}}}{G_{R134a}}\right)^2 + \left(\frac{P_{G_{R134a}}}{G_{R134a}}\right)^2}$$

where, U : Total uncertainty

B : Bias error

P : Precision error (random error)

The bias error of the R-134a mass flux consists of the error from density measurement and volumetric flow rate. Effect of the uncertainty in flow area can be negligible relative to the influence of the mass flow rate of R-134a.

$$B^2{}_{G_{R134a}} = \left(\frac{\partial G_{R134a}}{\partial \rho_{R134a}} B_{\rho_{R134a}}\right)^2 + \left(\frac{\partial G_{R134a}}{\partial Q_{R134a}} B_{Q_{R134a}}\right)^2 = \left(\rho_{R134a} B_{\rho_{R134a}}\right)^2 + \left(Q_{R134a} B_{Q_{R134a}}\right)^2$$

$$\frac{B_{G_{R134a}}}{G} = \pm\sqrt{\left(\frac{B_{\rho_{R134a}}}{\rho_{R134a}}\right)^2 + \left(\frac{B_{Q_{R134a}}}{Q_{R134a}}\right)^2}$$

where, $\frac{B_{\rho_{R134a}}}{\rho_{R134a}}$ =0.001 (0.1%): Bias error of R-134a table

$B_{Q_{R134a}}$ =0.001 (0.1%): Bias error of the Coriolis mass flow meter

The precision error of mass flux is as follows,

$P_{G_{R134a}} = K\frac{S_{G_{R134a}}}{\sqrt{N}} = 1.96\frac{S_{G_{R134a}}}{\sqrt{N}}$: Precision error of the test data

where,

S_P : Standard deviation of the pressure measurement data

II. Inlet and Outlet Pressure

Since the pressure is measure directly by the pressure transmitter. The uncertainty of the pressure can be written as follows,

$$\frac{U_P}{P} = \pm\sqrt{\left(\frac{B_P}{P}\right)^2 + \left(\frac{P_P}{P}\right)^2}$$

The bias error and precision error (random error) are as follows, respectively.

$B_P = 0.0018\ (0.18\%)$: Bias error of the pressure transmitter

$P_T = K\frac{S_P}{\sqrt{N}} = 1.96\frac{S_P}{\sqrt{N}}$: Precision error of the test data

where,

S_P : Standard deviation of the pressure measurement data

III. Inlet and Outlet Temperature

Since the temperature is measure directly by the thermocouple. The uncertainty of the temperature can be written as follows,

$$\frac{U_T}{T} = \pm\sqrt{\left(\frac{B_T}{T}\right)^2 + \left(\frac{P_T}{T}\right)^2}$$

The bias error and precision error (random error) are as follows, respectively.

$B_T = 0.0037\ (0.37\%)$: Bias error of the thermocouple sensor

$P_T = K\frac{S_T}{\sqrt{N}} = 1.96\frac{S_T}{\sqrt{N}}$: Precision error of the test data

where,

S_T : Standard deviation of the temperature measurement data

IV. Rolling Angle and Period

Rolling angle and period are checked by accelerometer. The uncertainty of the temperature can be written like

$$\frac{U_{\theta_R}}{\theta_R} = \pm\sqrt{\left(\frac{B_{\theta_R}}{\theta_R}\right)^2 + \left(\frac{P_{\theta_R}}{\theta_R}\right)^2}$$

The bias error and precision error (random error) are as follows, respectively.

$B_{\theta_R} = 0.00233(0.233\%)$: Bias error of the pressure transmitter

$P_{\theta_R} = K\frac{S_{\theta_R}}{\sqrt{N}} = 1.96\frac{S_{\theta_R}}{\sqrt{N}}$: Precision error of the test data

where,

S_P: Standard deviation of the pressure measurement data

V. Heat Flux

The heat flux is calculated by voltage, current and heat transfer area. The voltage and current are measured by voltmeter and shunt.

$$q^{"} = \frac{Q}{A} = \frac{VI}{\pi D L_h}$$

Effect of the uncertainty in heat transfer area can be negligible relative to the influence of the voltage and current. The measurement uncertainty of the heat flux can be calculated as follows,

$$\frac{U_{q^{"}}}{G_{q^{"}}} = \pm\sqrt{\left(\frac{B_{q^{"}}}{q^{"}}\right)^2 + \left(\frac{P_{q^{"}}}{G_{q^{"}}}\right)^2}$$

$$B^2_{q''} = \left(\frac{\partial G_V}{\partial V} B_V\right)^2 + \left(\frac{\partial G_I}{\partial Q_I} B_I\right)^2 = \left(VB_V\right)^2 + \left(IB_I\right)^2$$

$$\frac{B_{q''}}{G} = \pm\sqrt{\left(\frac{B_V}{V}\right)^2 + \left(\frac{B_I}{I}\right)^2}$$

where, B_V =0.04 (4%): Bias error of voltage

B_I =0.04 (4%): Bias error of the current

국문 초록

선박용 원자로는 해상에서 운전되어 부하 변동 및 선체 요동에 의해 지상 원전과 다른 열수력 특성을 갖는다. 선체 요동이 원자로의 냉각재 계통에 미치는 영향에 대한 정량적 평가는 필수적이며, 선박용 원자로의 안전 설계에 반드시 반영되어야 한다. 특히, 선박용 원자로의 안전 여유도 및 운전을 고려하기 위하여 롤링 조건에서의 임계열속 예측은 중요하다.

본 연구에서는 선박용 원자로 냉각재 계통의 열수력 특성을 분석하기 위한 열수력 시스템 코드인 TAPINS-M을 개발하였다. 선박의 움직임을 모사하기 위해 선박 요동 모델과 실험을 통해 개발된 임계열속 예측 모델을 TAPINS-M 코드에 삽입하였다.

임계열속의 경우, 실험 및 이론적으로 많은 연구가 진행되어 왔지만, 대부분의 경우 선박용 원자로에 직접적으로 적용하기 어렵다. 특히, 지금까지 롤링 조건에서의 임계열속에 관한 연구가 없었으며, 실험자료도 충분치 않아 이 영역에 대한 현상 규명이 어려웠다.

롤링 조건에서 임계열속 현상을 이해하기 위한 실험을 수행하였다. 롤링 조건에서 임계열속은 특정 유속 영역을 기준으로 롤링 운동에 의해 정지 시 임계열속과 비교하여 증가하거나 감소하는 현상이 나타났다. 롤링 시 실험 결과를 바탕으로 임계열속 예측모델을 개발하였다. 롤링 시 임계열속 기구를 규명하기 위해서는 정지 시의 유동양식을 파악하여야 하는데, 이를 위해 공극률 계산을 통하여

액막건조 (LFD; Liquid Film Dryout), 그 외의 영역은 핵비등이탈 (DNB; Departure from Nucleate Boiling) 기구라고 구분하였다. 또한, 임계열속이 천이되는 영역을 천이영역 (TR; Transition Region)이라 정의하였다. 상관식 개발 시 무차원수는 액막건조와 핵비등이탈 영역의 임계열속 기구 특성을 반영하여 결정하였고, 함수형태는 임계열속 경향 및 기존의 상관식을 활용하여 결정하였으며, 상수는 다차원 회귀방법론을 통하여 도출하였다. 또한, 천이 영역은 지수 보간법을 이용하여 예측하였으며, 지수 값은 환형류가 발생되는 시점의 공극률 함수를 사용하였다.

최종적으로 TAPINS-M 코드 검증을 위해 다양한 정상상태 및 과도상태 해석을 수행하였다. 롤링 조건에서의 단상 및 이상류, 자연대류 및 강제 대류 실험과의 비교를 통해 TAPINS-M의 유량 변동 해석능력을 검증하였다. 코드 검증을 위한 과도실험 데이터를 생산하기 위해 펌프 정지 및 과도 압력에 대한 추가적인 실험을 수행하였고, 이를 TAPINS-M의 해석결과와 비교하였다. TAPINS-M의 검증 결과로부터, 선박용 원자로의 열수력 현상에 대해 신뢰성 있는 해석결과를 제공할 수 있음을 입증하였다.

주요어

선박용 원자로, MARMS 장치, 임계열속, 이종유체관 척도, R-134a, TAPINS-M 코드, 임계열속 상관식, 선체 요동, 선박요동 모델, 코드 검증

학번: 2009-30264

감사의 글

마7장7~8절 말씀

구하라 그리하면 너희에게 주실 것이요, 찾으라 그러면 찾을 것이요, 문을 두드리라 그러면 너희에게 열릴 것이니 구하는 이마다 얻을 것이요, 찾는 이가 찾을 것이요 두드리는 이에게 열릴 것이니라(마7:7−8). 대학원의 문을 연 순간부터 지금까지 이 날을 바라며 한참을 걸어온 것 같습니다. 매 순간 저에게 용기와 지혜로 인도해주신 주님께 이 영광 바칩니다.

긴 터널 끝의 빛을 따라 끝없이 걸어가는 듯 했던 대학원 생활이 아직 미흡하지만 한 권의 논문으로 결실을 맺게 되어 가슴이 뜨거워집니다. 제가 여기까지 올 수 있도록 부족한 저에게 사제의 연을 허락해 주시고 가르침을 받을 기회를 주신 박군철 교수님께 진심으로 감사드립니다. 그리고 대학원에 처음 입문하여 연구자로써 기초를 다지고 정진할 수 있도록 해주신 서균렬 교수님, 바쁘신 와중에 흔쾌히 심사위원을 허락해주시고 부족한 점을 지적하여 주신 심형진 교수님, 저의 연구에 관심을 가져주시고 논지를 정확히 짚어 주셔서 저로 하여금 더 깊이 집중할 수 있도록 해 주신 이광원 상무님 감사합니다. 또한 연구자의 正道를 알려주시고 저를 다신 한번 되돌아볼 수 있도록 해주시고 저의 졸업을 위해 하나부터 열까지 철저히 준비할 수 있도록 도와주신 조형규 교수님, 제가 발전 할 수 있도록 무수한 기회를 주시고 저의 미래에 대해 폭넓게 생각할 수 있도록 조언을 아끼지 않으신 김응수 교수님 감사합니다. 처음 실험장치를 설계할 때 이론과 실제의 차이에서 막막했던 저에게 해결책과 방도를 간구해주시어 순탄하게 진행될 수 있도록 도와주신

천세영 박사님, 문상기 박사님께 감사드립니다.

졸업하기까지 물신양면 도와주신 많은 연구실 선배님에게도 감사의 마음을 전하고 싶습니다. 연구를 시작하고 끝날 때까지 조언을 아끼지 않으시고 어려운 부탁도 항상 흔쾌히 들어주신 홍성덕 선배님, 논문의 막바지에 감동의 큰 도움을 주신 권현 선배님 감사합니다. 중간 중간 연구가 샛길로 가지 않도록 흐름을 다잡아주신 성진이형과 동운이형, 처음 연구실에 와서 빨리 적응할 수 있도록 도와주고 후배들에게 아낌없는 사랑을 베푸신 종원이형, 함께 운동하고 술 한잔 기울이며 고민을 나눌 수 있었던 종수형, 저에게 부케를 던져주어 길이길이 잊지 못할 추억을 주신 윤제형, 청첩장을 잊고 보내지 않은 불경죄(?)를 저질렀지만 돌잔치때는 꼭 불러 하시며 오히려 감동을 주신 거형이형, 먼 미국에서도 학문의 깊은 곳에서 연구와 시름하며 살고 있을 수종이형, 모두 감사드립니다.

같은 시기 대학원에 입학하여 설마 했던 기적을 함께 경험하고 대학원 기간 동안 함께했던, 나에게 귀감이 되어준 연건, 가장으로써의 책임감을 보여주고 아이들을 순풍순풍 낳아 주위를 놀라게 하는 절대 남자 성수, 어느덧 아빠가 되어 어깨가 무거워진 태진이, 터프한 외모와 달리 늘 적극적으로 도와주고 희생하는 진화, 인생을 즐길 줄 아는 지훈이, 자신이 힘들어도 남을 먼저 챙기고 최근에는 함께 헬스를 죽어라 같이하는 정훈, 연구실에서 더 잘 챙겨주지 못해 미안한 마음이 드는, 실험장치를 제작하며 온갖 시련을 극복하여 고맙고 조금만 더 잘 다듬어 나간다면 앞이 기대가 되는 일웅이, 연구실 과도기의 중심에 서서 홀로 풍파를 해치고 가지만 의젓하게 잘 이겨내는 동호, 순진한 것 같은 외모를 가졌지만 예상치 못한

반전으로 주위에 행복바이러스를 전하는 민섭, 부족한 선배를 이해해주고 도와준 (구)NuTHEL 홍일점 민영이, KISTEP 인연으로 좋은 후배를 알게되어 기쁜 혜윤, 설레임으로 막 대학원을 시작한 재순과 세린, 박사논문 준비에 혼이 나간 선배의 빈 곳을 채워준 연구실 후배들 모두 진심으로 고맙고 훌륭한 동료 및 후배들과 함께 해서 영광이었다는 말을 전하고 싶습니다.

또한, NUIDEA 연구실에서 함께했던 모든 식구들에게도 감사를 전하고 싶습니다. 처음 낯선 연구실에 와서 적응할 수 있도록 도와주신, 동거동락하며 실험하고 성공이라는 기쁨을 같이 누린 상우형, 많은 조언을 아끼지 않으신 찬수형, 동갑내기이지만 배울 점이 많은 형민, 미국에서 열심히 박사학위를 준비 중인 경민, 후배로써 잘 따라주고 힘들지만 항상 밝게 웃는 모습이 보기 좋은 재욱, 모두 감사합니다.

저를 멀리서 응원해주시는 최고의 지지자이며 후원자이신 부모님께 이 논문을 바칩니다. 항상 친아들처럼 믿어주신 지금은 하늘에 계신 장인어른, 저를 위해 항상 기도하여 주시는 장모님에게도 감사드립니다. 앞으로 더 열심히 사는 아들, 사위 모습 보여드리려 노력하고 효도하며 행복하게 살겠습니다. 10년 이상 함께 지내며 인생을 같이 하는 내 친구 재홍, 승환아 너희들 덕에 힘들 때 위로가 되었다.

마지막으로, 아름답고 사랑하는 저희 아내 유미에게 남편이 다른 걱정 없이 학업에 전념할 수 있도록 도와주고, 바쁘다는 핑계로 함께 하지 못하여도 오래도록 묵묵히 기다려준 것에 대한 미안함과 고마움을 동시에

전합니다. 처음 만났을 때부터 결혼한 지금까지 나를 믿어주고 사랑해줘서 고맙고 앞으로는 내가 더 잘하겠다는 마음을 전하며 이 글을 마칩니다.